Functionalisation of Surfaces and Interfaces:

Molecules, Particles and Crystals

By

Massimo Peruffo

A Thesis submitted for the degree of
Doctor of Philosophy

Department of Chemistry
University of Warwick

February 2010

For my parents

Contents

List of Figures

List of Tables

Acknowledgements

First and foremost I would like to thank Prof. Patrick Unwin for all his help and patience thorough my PhD. His encouragement and sometimes the animated discussions enable me to obtain this degree. I am grateful to Paolo Bertoncello that helped and advised me from the beginning of my PhD. An important mention to Pablo Contrera and Evans Kefalas for their help, collaboration and exchange of ideas. I am also grateful to my industrial collaborator at Reckitt-Benkiser, Liliana. Thanks to Tahani and Michelle for helping me on the crystal growth experiments, Martin Edwards and Hayley Morley for the COMSOL simulations. Thanks to Steve York helping me with the FE-SEM images. I also would like to acknowledge Marcus Grant and Lee Butcher in mechanical workshop for all their help. Their work has been absolutely crucial in the developing the flow cells.

I would like to thanks the electrochemistry and interfaces group, especially the people in C113. A particular thanks to Carrie-Anne, Michael, Laura and Hollie for the coffee breaks and many other things… Mathias for sharing for so long the house and for the interesting scientific discussions. Agnieszka for the electrochemistry evening chats.

Raffaello and Paola that have made available their support in a number of ways, for being always available and kind for anything I needed.

Finally, I would like to thank my family for their support and understanding.

Declaration

The work contained within this thesis is entirely original and my own work, except where acknowledged in the text. I confirm that this thesis has not been submitted for a degree at another university.

Part of this thesis has been published as detailed below:

Bertoncello, P.; Peruffo, M.; Unwin, P. R. *Chemical Communications* **2007**, 1597-1599

Bertoncello, P.; Peruffo, M.; Li, F.; Unwin, P. R. *Colloids and Surfaces A: Physicochemical and Engineering Aspects* **2008**, 222-6

Peruffo, M.; Contreras-Carballada, P.; Bertoncello, P.; Williams, R. M.; Cola, L. D.; Unwin, P. R. *Electrochemistry Communications* **2009**, 1885-7

Abstract

This thesis is concerned with understanding and directing the functionalisation of solid surfaces with materials: molecules, nanoparticles and crystals. Both conducting (electrode) and insulating surfaces are of interest. For molecular functionalisation, a sweep potential procedure has been developed to assist the formation of self assembled monolayers (SAMs) of a ruthenium thiolated complex. Electrochemical investigations were employed to characterised the SAM formed on a platinum electrode.

Nanoparticles formation explored two distinct routes. First Pd nanoparticles were successfully formed within ultra-thin Nafion films via impregnation and a chemical reduction method. Morphological investigations utilised atomic force microscopy. The electrocatalytic properties of the nanocomposite material were elucidated for the hydrogen oxidation reaction. The methodology used for the preparation of this nanocomposite material shows promise for applications in sensors and fuel cells. Second, the potential-assisted deposition of pre–formed perthiolated-ß-cyclodextrin-capped Pt nanoparticles method is described. Pt nanoparticles (5 nm diameter) were deposited in a controlled fashion on indium tin oxide and highly oriented pyrolytic graphite electrodes. The Pt nanoparticles formed in this way were electrocatalytically active towards hydrogen generation and oxidation. This new approach for the deposition of metal nanoparticles with controlled surface density provides a new tool for the investigation of electrocatalytic processes.

A major focus of the second part of the thesis has been the development of methods to study crystal deposition at extreme supersaturation. For this purpose a delivery system for calcium carbonate at high-supersaturation ion has been coupled with a quartz crystal microbalance and in–situ optical microscopy. The dynamics and quantitative evaluation of calcium carbonate deposition onto foreign solid substrates, and the effect of various additives, are described. Ex–situ studies, scanning electron microscopy and microRaman spectroscopy, allowed the morphological characterisation of the phases deposited. The transformation of ACC to calcite has been explored in details. In the study of additives, a significant finding was that citrate concentration shows a non-monotonic behaviour on the amount of scale deposited. Fast screening of different additives (polymeric and molecular) and a quantitative ranking of their inhibitory properties on calcium carbonate deposition on a gold surface is described. Molecular and polymeric additives showed different inhibitory mechanisms on the scaling process and the technique employed gave a better insight into their mode of action.

Abbreviations

ACC	amorphous calcium carbonate
AFM	atomic force microscopy
B–V	Butler Volmer theory
CA	chronoamperometry
CD	cyclodextrin
CIT	citrate
CNT	classical nucleation theory
CV	cyclic voltammetry
ET	electron transfer
FE-SEM	field emission scanning electron microscopy
HER	hydrogen evolution reation
HOPG	highly orientated pyrolytic graphite
ITO	indium tin oxide
KSV	Kossel, Stranski and Volmer theory
LS	Langmuir-Schaefer
LSV	linear sweep voltammetry
NP	nanoparticle
QCM	quartz crystal microbalance
SAM	self-assembled monolayer
SECM	scanning electrochemical microscopy
TEM	transmission electron microscopy
UME	ultramicroelectrode

Glossary of Symbols

ΔG	Gibbs energy
$\Delta \mu$	chemical potential
A	area
a	radius
C	capacitance
D	diffusion coefficient
d^1	Helmholtz inner layer
d^2	Helmholtz outer layer
d^3	diffuse layer
E	electrical potential
F	Faraday constant
f	frequency
h	height
i	current
I	ionic strength
j	current density
k^0	standard rate constant
k_{ads}	adsorption rate constant
k_B	Boltzmann constant
k_{sp}	solubility product
m	mass
q	charge
r	radius
S	saturation ratio
t	time
T	temperature
V	volume
Γ	surface coverage
γ	activity coefficient
ε_r	dielectric constant
v	scan rate
ρ	density

Chapter 1 INTRODUCTION

Surface science is a discipline that investigates phenomena that occur at interfaces, where an interface is defined as the boundary between two dissimilar phases. Common interfaces investigated by this branch of science are solid/gas, solid/liquid and solid/solid and the phenomena that occur can be distinguished as chemical and physical processes or physicochemical. This thesis is concerned with the functionalisation of solid/liquid interfaces either deliberately or advantageously from the molecular, to the crystal, scale. Consequently, this chapter gives an overview of adsorption, nucleation and growth processes at liquid/solid interface. Particularly relevant to the thesis is the formation of functionalised self-assembled monolayers, metal nanoparticles decoration of electrodes and the deposition of amorphous and crystalline $CaCO_3$. These topics are covered in this chapter.

1.1 A Broad Overview of Surface Science

Benjamin Franklin can be considered as a major pioneer of interfacial science with his studies on the spontaneous spreading of oil on water (17th

century). From this first step, knowledge on surface interactions, reactions and characterisation have progressed enormously with time (Figure 1-1) and the area has attracted the attention of many scientists from many different fields.

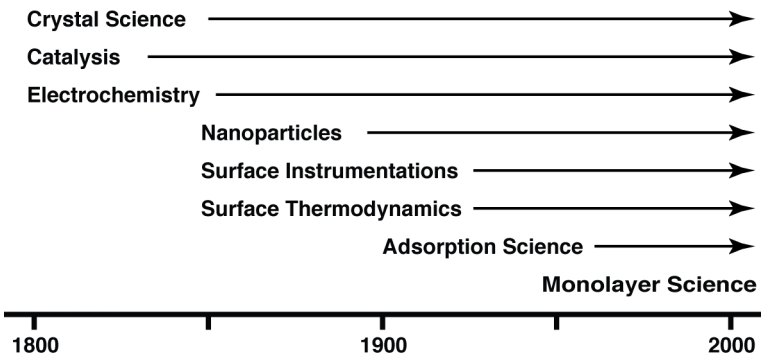

Figure 1-1. Interfacial science time line [1].

Interfacial science has been profoundly involved in the understanding of prenucleation, nucleation and growth mechanisms of crystals. In the early 18th century scientists have extensively investigated these processes. Ostwald [2] gave a major contribution theorising the preferential growth of large crystals compared to smaller ones. Larger crystals are energetically more stable, as a consequence of the superficial atoms having a higher energy with respect to the inner (bulk) atoms, so that a large crystal has lower surface to volume ratio with respect to a small crystal. Similar behaviour is encountered during the synthesis of metal nanoparticles in solution; their enhanced catalytic properties for some reactions [3-5‘is related to the high surface to volume ratio [6], but small particles (higher free energy) also tend to aggregate in solution to minimise the free energy. The most widespread strategy to avoid this issue and obtain small stable nanoparticles has been to exploit the affinity of alkanethiols for metals. This category of organic molecules is adsorbed on the surface of the nanoparticles forming a monolayer that prevents aggregation [7] and eventually small and stable nanoparticles are obtained.

The process of adsorption of molecules on a surface is itself an interesting process to investigate. The formation of self-assembled monolayers on a surface involves the interactions between the molecules constituting the monolayer and the substrate, and inter–molecule interactions within the monolayer [8]. Langmuir with his thermodynamic studies of chemisorption and physisorption of monolayers provided a fundamental starting point for the development of this field of science.

Surface science development has been strictly correlated with the progress of new instrumentation that has allowed characterisation of surface structure at molecular and atomic levels, as illustrated in Table 1-1 which provides a summary of some of the key techniques.

Table 1-1. Instrumental techniques for surface investigations.

Technique	*Surface information*
Atomic force microscopy	Surface structure
Scanning tunnelling microscopy	Surface structure
Angle-resolved photoemission spectroscopy	Electronic Structure, surface structure
Scanning electron microscopy	Surface topology, element analysis
Ellipsometry	Layer thickness
Secondary ion mass spectroscopy	Surface composition
X-ray photoemission spectroscopy	Composition, oxidation state
Transmission electron microscopy	Surface structure

1.2 Self-Assembled Monolayers

Self-assembled monolayers (SAMs) are a convenient and practical system to form well-defined ultra-thin film (typically 1–3 nm) of organic

material on metal and other surfaces with tuneable chemical physics properties. Using targeted organic synthesis, it is possible to obtain atomic control of the structure of the molecules employed to form SAMs; positioning organic and organometallic functional groups along a molecular chain, this functionality can be transferred to the vertical structure of a SAM [9-11]. Furthermore, scanning probe techniques, and electron or atomic beam μ-printing can be used to obtain horizontal patterning with 1–100 nm domain size [12-18] obtaining multi constituent SAMs over a surface [19, 20].

SAMs have attracted attention for potential technological applications in areas such as catalysis, chemical sensing, adhesion and biocompatible materials [22-23]. With recent development in molecular electronic devices, SAMs have also started attracting attention in this field as well broadening their applications [24-26]. They have been extensively used as tuneable insulating media to investigate electron transfer from the supporting metal electrode to a terminal redox group [9]or to explore the influence of conjugated bonds on the conductance of organic molecules [27, 28].

1.2.1 SAM Formation and Characteristics

The process of the formation of SAMs consists of the chemisorption of organic molecules from a gas or liquid phase to a solid surface (metal semiconducture or insulator) [29]. Specifically synthesised organic molecules (Figure 1-2) constituted by: i) a *head group* for high affinity with the metal surface; ii) a *spacer* that has the double function to provide stability (interactions between contiguous molecules) and to form a barrier between the environment

and the metal surface; iii) a *functional group*, are usually employed in order to obtain a SAM on a metal surface.

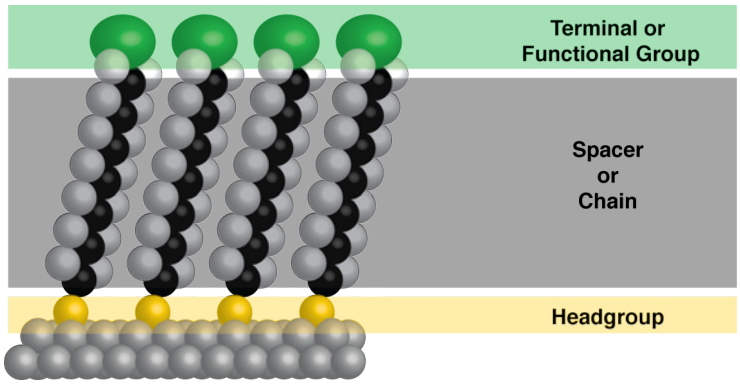

Figure 1-2. SAM molecule description

One of the most common procedures to prepare SAMs is to immerse a clean and flat surface (*vide infra*) in a dilute solution (1–10 mM) containing the constituent of the monolayer for 12–20 h (room temperature) allowing the adsorption of the molecules at the metal surface [30]. The process leading to the SAMs formation is subdivided into two main steps with different time scales and thermodynamical properties, namely adsorption on the surface and rearrangement of the molecules at the surface [31].

1.2.1.1 Adsorption Process

Adsorption is defined as the accumulation of species on a surface from a neighbouring phase, with the type of interaction between the surface and the adsorbate subdivided into two categories: physisorption and chemisorption. Weak interactions are characteristic of physisorption governed by induced dipole interaction (van der Waals interactions), while chemisorption is characterised by strong interactions, ionic or covalent bonds, which are typical of those in the formation of SAMs.

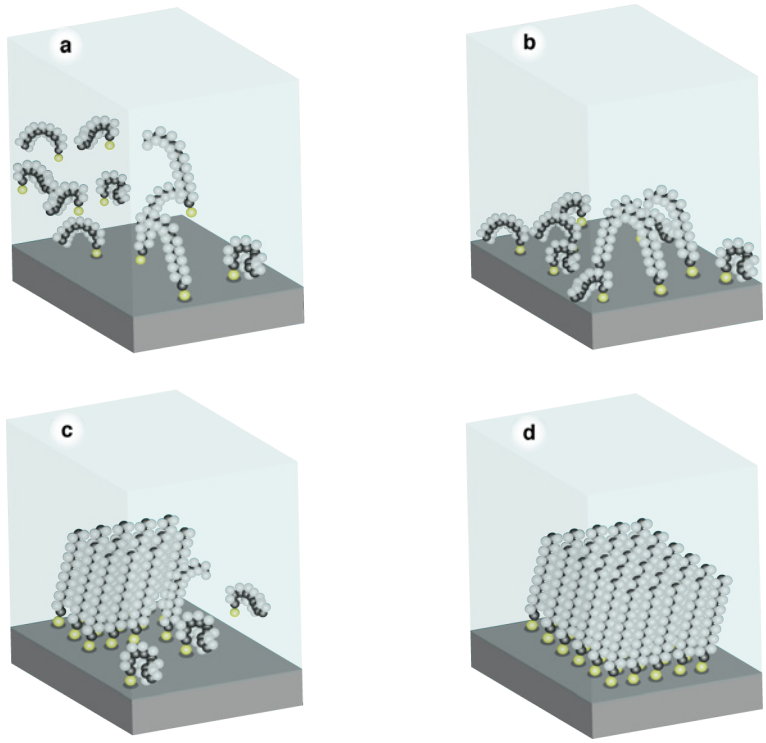

Figure 1-3. SAM adsorption process steps

The first step in adsorption is the transfer of adsorbates from bulk to the surface by mass transport, followed by the actual adsorption on the surface that involves chemisorption (Figure 1-3a). The overall process could be controlled by mass transport, adsorption rate or be in a mixed regime. The formation of a densely packed monolayer on a surface from dilute solution is a quick process (Figure 1-3b), after a few minutes of deposition a rather high surface coverage could be reached [32]. An increase in the concentration in solution shortens the deposition time, but the SAM formed during this fast process is poorly ordered. Despite the first phase being fast there is a second phase in which the molecules on the surface rearrange to form a well-ordered monolayer (Figure 1-3c), that requires a period from a few hours to days and is mainly regulated by the interactions between the molecules (*vide infra*). Finally, a compact and well-ordered monolayer is formed (Figure 1-3d) [33].

Exploiting the affinity of sulphur with different metals (Ag, Hg, Pd, Pt) and particularly with gold; organosulphur (thiols, disulfides, sulphides) are widely used to prepare SAMs on metal surfaces [34-38]. The energy of metal-thiol bonds is of the order of 100 kJ mol^{-1} [39]. The reaction on gold has been extensively investigated and no S–H stretching vibration is seen via Raman or infrared spectroscopy after the formation of the SAM [40, 41]. Furthermore, laser desorption mass spectrometry shows molecular thiols as negative ions desorbing from the surface [42]. While the actual reaction involved in the binding of thiols to metal (M) surfaces is not yet completely established, the accepted mechanism is an oxidative addition of the S–H to the metal with release of H_2 in the gas phase (1) or formation of water in presence of O_2 in solution (2) [29].

$$RS-H+M \rightarrow RS-M+\tfrac{1}{2}H_2 \qquad (1)$$

$$\begin{aligned} &RS-H+M \rightarrow RS-M+H_{ads} \\ &4H_{ads}+O_2 \rightarrow 2H_2O \end{aligned} \qquad (2)$$

1.2.1.2 Monolayer Organisation

After the initial adsorption phase, the molecular environment induces a non–covalent interaction between neighbours and a molecular rearrangement takes place [43]. This second stage needs much longer time, and the kinetics is in the range of 2 orders of magnitude slower compared to the adsorption process [32, 44]. This rearrangement provides a more compact monolayer and further molecules are thus adsorbed on the surface increasing the overall surface coverage. This phase is mainly regulated by the mobility of molecules on the

surface and the interactions between them, although the chain (spacer) structure and composition play a key role. Van der Waals interactions between adsorbates are the driving force for the reorganisation giving an important contribution to the stabilisation of the monolayer. The characteristic and reproducible vertical orientation of the molecules on the surface suggest a strong inter–chain interaction to minimise the energy of the system [45].

The orientation of molecules on the surface is controlled by two competitive factors: the stability of the metal-sulphur bond; and the maximisation of van der Waals interactions, with both dependants on the direction of the molecules. The orientation is defined by the angle between the main directrix of the molecules and the surface (Cant angle, α) and the rotation of the C–C chain (β) (Figure 1-4). Alkanethiols have been studied extensively and these parameters have been measured for different substrates, i.e. on gold, silver, platinum the values are 28° (α) / 53° (β), 11° – 14° (α) / 45° (β), <15° (α), respectively [46, 47].

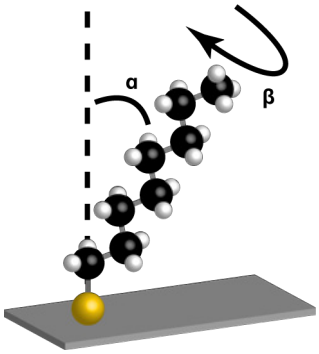

Figure 1-4. Molecule orientation on a SAM.

With the introduction of a specific functional group along the spacer chain, it is possible to obtain relative control on the structure of SAMs. In particular, insertion of a functional group along the chain results in a change of the molecular tilt (α) in order to maximise the interactions of the functional

groups between neighbouring molecules [48-50]. Nevertheless, the presence of bulky groups could also slow down the chemisorption kinetics and the adsorption process may couple with the rearrangement mechanism and decrease the chain interaction, so that a less stable and ordered SAM is obtained [49].

1.2.1.3 Defects

Figure 1-5 depicts the most common defects that could encountered on SAMs and can be caused by several factors; the cleanliness of the substrate and the presence of impurities in solution. The presence of foreign particles on the surface, which are not displaced (energetically unfavourable process), interrupt the continuity of the ordered monolayer. Furthermore, particles dissolved in solution can be trapped within the monolayer, as adsorbate impurities can be physisorbed on the surface driving to discontinuity on SAM organization. Another important factor is the topography of the substrate: polycrystalline or not atomically flat surfaces present discontinuities [51, 52]. The non–uniformity and purity of the metal surface is reflected in the non–uniformity of the SAM and these types of defects are strongly evident in electrochemistry experiments, i.e. the pinhole effect [53] is defined as tiny exposure of the underling metal to the solution, by incomplete SAM coverage. This is a serious problem when SAMs are employed as a blocking barrier.

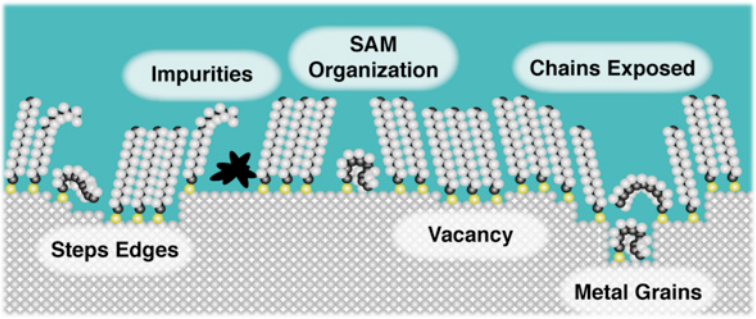

Figure 1-5. SAM defects description.

Adsorption is a dynamic process that is regulated by the equilibrium of the adsorbate in solution and at the surface. It is important to note that a weak S–M bond could lead to a high surface coverage of the monolayer when the solute is present in solution, but a quick desorption process in a fresh solution which does not contain the adsorbate.

1.2.1.4 Solvent

The solvent is of extreme importance, since deposition is affected by solvent/adsorbate and solvent/substrate interactions, but the effect of these interactions is not yet well understood. Several different solvents have been employed to search for the optimal experimental conditions to form a close packed monolayer and only general information has been acquired. Non–polar solvents increase the ratio of adsorption, but solvents with long carbon chains can interfere with the organisation of monolayers [54-57]. Nowadays, the most common solvents used are ethanol, tetrahydrofuran, acetonitrile and toluene, and there are no substantial differences upon the deposition of thiols [32].

1.2.2 Electrochemistry of a Confined Redox Species on a Surface

SAMs formed from thiols, disulfides and sulfides on gold have a relatively strong resistance against reductive desorption (3) [58, 59], but on other metals the stability is reduced [60]

$$M - SR + e^- \rightarrow M + {}^-SR \qquad (3)$$

Typical cyclic voltammograms (CVs) show a sharp cathodic peak for the stripping of the sulphur and a broad anodic peak for the adsorption, the

desorption proceeds via a nucleation centre is homogeneous across the metal surface [61], and the desorbed thiols tends to stay close to the surface and are readily readsorbed during the oxidative wave [62].

An electrode immersed in a solution generates a charge on the surface, resulting in the formation of a non–zero potential at the electrode/solution interface; the ions in solution migrate toward the surface to form a layer that counterbalances the surface charge (Figure 1-6a), resulting in the formation of a Helmholtz double layer (d^1 inner layer, d^2 outer layer). The high concentration of ions near to the surface creates a gradient of electrolyte concentration with the bulk solution, and a diffuse layer (d^3) is formed from the surface to the bulk.

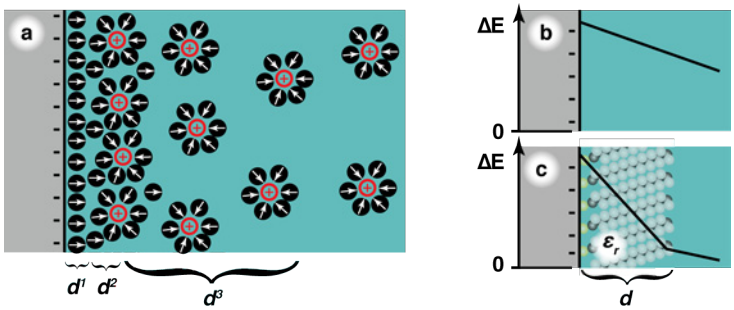

Figure 1-6. Helmholtz double layers (a), Potential gradient without (a) and with (c) the presence of an organic film.

In a relatively high electrolyte concentration, the Helmholtz double layer determines an interfacial capacitance (10–100 μF cm^{-2}) that depends on the potential applied to the electrode. Organic molecules (Figure 1-6c) have a low dielectric constant compared to an electrolyte solution hence an organic monolayer at the surface of the electrode dramatically decreases the Helmholtz capacitance, and it is virtually independent of potential [63, 64]. The capacitance is easily calculated by linear sweep or cyclic voltammetric experiments

$$C = \frac{dq}{dE} = \frac{i}{v} \tag{4}$$

where q (C) is the charge, E (V) is the potential applied at the electrode, v (V sec^{-1}) is the scan rate ($dq/dt = i$ and $dE/dt = v$), i (A) is the current and C (Farad) is the capacitance which is proportional to the dielectric constant of the media (SAM) and inversely proportional to its thickness

$$C = \varepsilon_r \frac{A}{d} \tag{5}$$

where ε_r (C V^{-1} cm^{-1}) is the dielectric constant of the organic SAM, A (cm^2) is the area of the electrode and d (cm) is the thickness. It is also possible to monitor the change of the capacitance during the deposition, to obtain in–situ information about the self-assembly process and the quality of the SAM that is produced.

The deposition of an organic non–conductive SAM on the surface of an electrode forms an insulating barrier that suppresses faradic processes [65]; electroactive solutes are denied access to the electrode surface. However, attaching a redox centre at the termination of the adsorbate SAM, provides a tool to investigate either: the electron transfer across a spacer of fixed length (thickness of the SAM) between the metal surface and the redox centre itself; or the effect of different types of spacer [66-69], for example, conjugated bonding along the chain, or aromatic moieties that increase the conductivity of the spacer that could act as a conductive medium between the electrode and the redox centre. The distance is easily tuneable using spacers with different lengths [70, 71]. The surface coverage of the redox centre is easily measured by integration of the peak current during the redox process after background subtraction ((6), (7), Figure 1-7).

$$q = \int_{E^i}^{E^f} \frac{idE}{\nu} \tag{6}$$

$$\Gamma = \frac{q}{n\mathrm{F}A} \tag{7}$$

where Γ (mol cm^{-2}) is the surface coverage of the redox centre, n is the number of electrons involved in the reaction, F (96.485 C mol^{-1}) is the Faraday constant and A (cm^{-2}) is the area of the functionalised electrode.

These types of investigations are less affected by the presence of pinholes, but surface coverage, lateral interaction and conformational distortions can influence the CV shape from ideality. In a reversible oxidation reaction of a SAM in which all the redox centres are initially in their reduced state

$$Red^{Z_{Red}} \underset{k_b}{\overset{k_f}{\rightleftharpoons}} Ox^{Z_{Ox}} + ne^- \tag{8}$$

j (A cm^{-2}), which is the current density associated by the reaction (8), and is expressed by

$$j = n\mathrm{F}\left(k_f\Gamma_{Red} - k_b\Gamma_{Ox}\right) \tag{9}$$

where k_f and k_b are the forward and backward half reaction rates constant and Γ_{Red} and Γ_{Ox} denote the surface concentrations (surface coverage) of the reduced and oxidised species. In a system of strongly adsorbed molecules, without adsorption and desorption, Γ_T is the sum of Γ_{Red} and Γ_{Ox} and is constant. The rate constants expressed using Butler–Volmer (B–V) formalism are

$$\begin{aligned} k_f &= k^0 \exp\left[\frac{n\mathrm{F}(1-\alpha)}{\mathrm{R}T}\left(E - E^0\right)\right] \\ k_b &= k^0 \exp\left[\frac{n\mathrm{F}\alpha}{\mathrm{R}T}\left(E - E^0\right)\right] \end{aligned} \tag{10}$$

where α defines the transfer coefficient, that corresponds to the symmetry of the energy barrier [72] and k^0 is the standard rate constant.

The current density can also be defined as

$$j = n\mathrm{F}\frac{d\Gamma_{Ox}}{dt} = n\mathrm{F}\frac{d\Gamma_{Ox}}{dE}\frac{dE}{dt} = n\mathrm{F}\nu\frac{d\Gamma_{Ox}}{dE} \qquad (11)$$

and from ((9), (11)) is possible to obtain a differential equation which, upon solving, gives the CV shape of the redox reaction

$$\frac{d\Gamma_{Red}}{dE} = \frac{1}{\nu}\left\{\Gamma_{Red}k^0\exp\left[\frac{n\mathrm{F}(1-\alpha)}{\mathrm{R}T}\left(E-E^0\right)\right] - \Gamma_{Ox}k^0\exp\left[\frac{n\mathrm{F}\alpha}{\mathrm{R}T}\left(E-E^0\right)\right]\right\} \qquad (12)$$

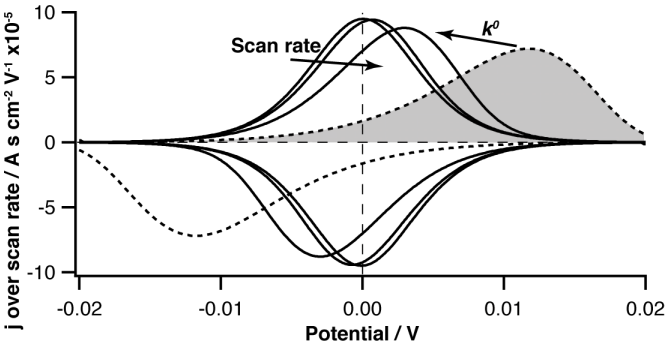

Figure 1-7. Simulation of CVs using Butler–Volmer formalism, (solid line) different scan rate with constant rate constant, (dashed line) same scan rate but smaller rate constant k_0.

In Figure 1-7 are shown the theoretical CVs at constant k^0 (10^5 s^{-1}) and increasing ν (100, 1000 and 5000 V s^{-1}) (solid line), and waves at the same ν (5000 V s^{-1}) and smaller k^0 (10^4 s^{-1}) (dashed line), considering a surface coverage of 10^{-10} mol cm^{-2}. It can be seen that on the forward and reverse CVs the peak to peak separation is related to the rate constant and increases for sluggish reaction rates and at faster scan rates. The possibility of modelling an experimental CV is useful in the calculation of the rate constant of the electron transfer.

A more rigorous treatment is obtained by including Marcus relations for the rate constant, in which the electronic coupling, the reorganisation energy and the Gibbs free energy between the initial and final states of the electron transfer

are considered [73, 74]. Several causes induce a deviation from the ideal theoretical shape of a CV and that seen in practice. Thus to obtain a more accurate evaluation of the constant rate, different models have been developed; in the following paragraphs brief overviews of some of these are reported.

Lateral interactions. Two neighbouring molecules exert a different interaction on each other depending on the oxidation state; Ox/Red, Ox/Ox and Red/Red and can exert attraction or repulsion to different degrees, and during a redox process the molecules change their oxidation states resulting in a continuous variation of the overall interaction energy. Laviron formulated a model based on B–V theory and when a Frumkin isotherm is followed [75]. It showed deviation from the ideal CV shape for strong interactions with consequent broadening of the peaks.

Effect of the interfacial potential. The redox centre is separated from the metal surface by an organic medium with low dielectric constant that decreases the potential sensed by the redox centre causing deviation from ideal behaviour. This has been considered in the model developed by Smith and White [64].

Effect of ion pairing. Variation of the monolayer charge during a redox process induces a flux of ions in and out the SAM region to compensate for different oxidation states of the active centre. The stabilisation energy depends on the number of ions constituting the solvation shell and this has been considered by Rowe and Creager [76] to develop an expression that relates the peak potential shift to the concentration of the ions in bulk (ionic strength effect).

1.3 Metal Nanoparticles

In early 1990 Giersing and Mulvaney published a work [77] in which the high affinity of alkanethiols for gold was exploited to stabilise gold nanoparticles (NPs) in solution. The study of objects with at least one dimension in the rage of 1 – 100 nm showed the importance of size and shape on physical and chemical properties of matter [78]; in the bulk metal electrons energy levels are a continuum, but decreasing the size of the body in which the electrons are confined, results in a quantisation of the energy levels [79-82], which drastically changes the chemical and physical behaviour of matter at the nanoscale [83]. Another feature that makes NPs interesting is the high fraction of atoms at the surface. Atoms at the surface have different properties compared to those in bulk; in particular the atoms have a lower coordination number that changes their reactivity [84, 85].

The assembly of metal nanoparticles on surfaces is currently of considerable interest due to their extraordinary properties; the formation of nanostructured interfaces on conductive substrates (electrodes) has led to the exploitation of their properties in a variety of applications including sensing [86-89] and nanoelectronics [90]. In electroanalysis NP decorated electrodes have a number of advantages in comparison to macroelectrodes, including intrinsically higher catalytic characteristic and an increase of the sensitivity. The small size produces an increase in mass transport (for surface coverage < 1 %) and the high surface area decreases the ratio of signal to noise [91].

Furthermore, NPs have an impact on the mass production of devices. The possibility to use small amounts of material, that are often expensive, such as

platinum, gold and palladium, instead of bulk quantities is of relevance for economical industrial application of metal catalysts.

1.3.1 Synthesis

Several strategies have been explored to synthesise NPs in solution [92], almost of which involve the reduction of metal ions in solution by chemical or electrochemical reduction [93]. A crucial issue to address is avoiding the aggregation of the nanoparticles. The atoms lying on the surface of the NPs have a higher free energy compared to those inside and increasing the size of the nanoparticle, decreases the surface to volume ratio, stabilising the nanoparticles. The resulting decrease of free energy is the driving force for aggregation during and after the synthesis. To overcome this issue different strategies have been explored and herein is a brief overview of some of them.

1.3.1.1 Colloidal Synthesis

There are primarily two mainstream strategies to protect NPs from aggregation in solution: *electrostatic stabilisation* in which ions in solution are adsorbed at the hydrophilic metal surface [94], and the resulting double layer charge prevents aggregation by Coulombic repulsion; *steric stabilization* [95] involves the self assembly of organic molecules on the metal surface of the NPs. Thiols are widely used for this purpose, and the resulting organic layer operates as a physical barrier against aggregation (Figure 1-8).

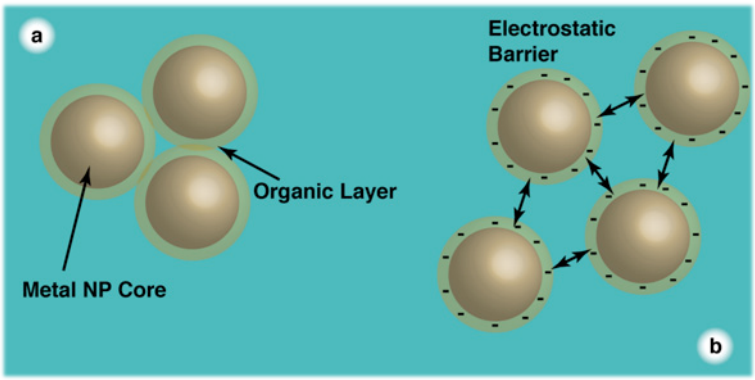

Figure 1-8. Steric (a) and electrostatic (b) stabilisation against aggregation.

The ligands used as a protection layer determine the solubility of the NPs in polar or non–polar solvents. NPs protected (capped) with non–charged organic molecules are soluble in non–polar solvent unless the organic molecules employed are functionalised with hydrophilic groups. A typical synthetic procedure for capped-metal nanoparticles consists of the reduction of a target metal salt in solution using a reducing agent in the presence of the protecting ligands [96, 97]. The size of the NPs can be controlled by employing different experimental conditions, including variation of the salt to ligand ratio [98], reducer strength and type of ligands [99]. A strong reducer, like $NaBH_4$, gives smaller particles compared to a weaker reducer (H_2). Since the reduction process takes place in the presence of the ligands that are adsorbed at the surface of the NPs, changing the affinity between the ligands and the growing NPs results in a variation of the final size of the NPs a strong affinity blocks the growth in the early stages resulting in small NPs. By adjusting these different experimental parameters it is possible to obtain a fine control over the size and shape of NPs [100, 101].

1.3.1.2 Surface Synthesis

A different approach to the synthesis of NPs is the electrodeposition on conductive substrates. A negative potential is applied at the conductive substrate (electrode) immersed in a solution of the metal salt to reduce the metal ion to metal. This method has been widely employed to decorate electrodes with a variety of different metal NPs [102, 103]. In this way it is possible to obtain highly pure NPs without a protecting layer that often decreases the catalytic properties of NPs [104]. Penner and co-workers [105, 106] have extensively explored electrodeposition of Pt and other metals on highly orientated pyrolytic graphite [103, 107-109]. To achieve uniform deposition of monodispersed NPs precise experimental conditions have to be devised. The potential applied to the surface as a single pulse or a sequence of pulses, as well as the concentration of the salt, has a critical effect on the deposition.

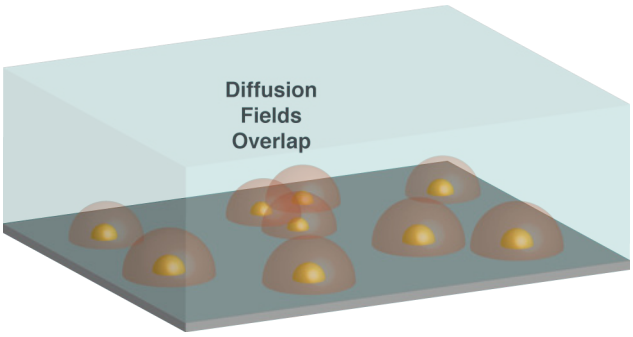

Figure 1-9. Electro deposition of nanoparticles and diffusion field.

To obtain monodispersed nanoparticles, an instantaneous nucleation is needed. Normally this is obtained by high driving forces (high reductive potential) to quickly saturate all the active sites on the surface. However, a high surface coverage can induce coupling between neighbouring NPs that brings an overlap of the ions diffusion field towards the surface (Figure 1-9) resulting in an

inhomogeneity of the mass transport and hence the final size distribution [107-109].

1.3.1.3 Impregnation and Reduction Method

This method consists of a two-step procedure. In the first step a template is impregnated with the ions of the target metal, the template can be provided by a film or membrane that allows metal ion exchange [110, 111] or a solid structure able to incorporate metal ions [112, 113]. The second step involves the reduction of the ions to the metal form. The template consists of small separated domains, each containing a discrete amount of ions, and during the reduction phase the small chambers essentially constitute a nano-reactor in which NPs form. The reduction can be achieved by addition of a reducing agent or, if the template is attached to an electrode, by electroreduction. The distribution of the NPs inside the template is related to the spatial structure of the substrate and a uniform structured polymer membrane or film is of extreme importance to obtain a final uniform nanostructured material [114, 115]. Several interesting works have been carried out by Crooks and co-workers [116] exploiting the capability of dendrimers to load metal ions and providing a template for the formation of monodisperse NPs with high catalytic activity [117].

1.4 Crystals

Understanding the mechanisms involved in the crystallisation process has interested scientists over a long period. The ability to control the crystallisation process, the size, and polymorphism of crystals are some of the main goals that

science is trying to achieve. Formation of crystals from electrolyte solutions is a fundamental process in nature [118] as well as in industries such as building materials [119], in pharmaceutical industries for which crystallisation is the main purification procedure, or for scaling effects on pipelines [120, 121]. Nature is able to mould the crystallisation process using additives to obtain incredibly resilient material such as bones and shells [122, 123], and the way they are able to control the formation, and structure of the material they need is amazing [124, 125]. Understanding these processes would allow us to create new materials with amazing properties of strength as nature already does. Many of the aspects of crystal growth are related to nanoparticle systems, discussed above, but crystal growth is complicated by a multitude of chemical species in solution that can influence the process.

1.4.1 Crystal Nucleation and Growth

The precipitation of a solid phase in an electrolytic solution (13) is driven by the difference in chemical potential of the solutes in the liquid phase ($\Delta\mu_l$) and in the solid phase ($\Delta\mu_c$) (14), where $\Delta\mu$ is defined by (15)

$$a\mathrm{A}^{z_a} + b\mathrm{B}^{z_b} \xleftrightarrow{K_{sp}} \mathrm{A}_a\mathrm{B}_b \downarrow \tag{13}$$

where k_{sp} is the solubility product.

$$\Delta\mu = \Delta\mu_c - \Delta\mu_l \tag{14}$$

$$\Delta\mu = -\mathrm{k_B}T\log\left(\frac{C}{C_e}\right) \tag{15}$$

where $\mathrm{k_B}$ is the Boltzmann constant (1.381 x10^{-23} m^2 kg s^{-2} K^{-1}), T (K) the temperature C the activity of the solute and C_e the activity at equilibrium. In case

of multiple components as in (13), C is substituted by the activity product and C_e by the solubility product. For values of C higher then C_e the formation of a solid phase is encouraged and deviation from the equilibrium, the driving force of crystallisation, is defined by the saturation ratio (S), which for (13) is defined by (16) [126].

$$S = \sqrt[a+b]{\frac{\{A\}^a \{B\}^b}{K_{sp}}} \tag{16}$$

Therefore essential conditions for nucleation and/or growth is a saturation ratio $S > 1$, namely the activities of the solutes exceed their solubility product.

The process of crystal formation can be divided into two main steps: i) nucleation, which is the formation of a new mineral phase, i.e. the formation of a stable 3D structure in solution; ii) the growth of a crystal, i.e. the process of addition of ions (or molecules) to the crystal surface from the solution.

Nucleation is a distinct process in homogeneous and heterogeneous growth; homogeneous nucleation is the formation of clusters and nuclei via aggregation of ions of the same compound, however when impurities are present in solution the nucleation occurs preferentially via aggregation at the surface of the foreign particles. These impurities act as nucleation sites for heterogeneous nucleation.

After the formation of the first stable crystal, the growth proceeds via incorporation of material from the solution to the surface of the crystal. The growth can then proceed via different mechanisms depending on the surface roughness and saturation ratio. Two-dimensional nucleation and spiral growth are primary mechanism [127].

1.4.1.1 Nucleation Phase

Nucleation consists of the formation of stable nuclei in solution, as described in the previous section. A saturated solution is an essential condition and the overall energy (ΔG) involved on the nucleation process is the sum of the energy of the aggregation of ions (ΔG_c), which is proportional to the volume of the cluster (r^3), and the energy gained by the formation of a solid/liquid interface (ΔG_s) that is proportional to the surface (r^2). In Figure 1-10 the total free energy is plotted, along with the components related to the surface (ΔG_s) and volume (ΔG_c), against the radius of the particle. For ΔG values corresponding to a radius lower then the critical radius (r^*) a cluster is energetically driven to dissolution and nucleation tends to be an extremely rare event thus a critical energy is needed to attain a stable nucleus. The saturation ratio plays a fundamental role on the nucleation probability, since ΔG_c increases with the saturation ratio (15), (16) and consequently r^* decreases. Thus, high-supersaturation values corresponds to a higher probability of nucleation.

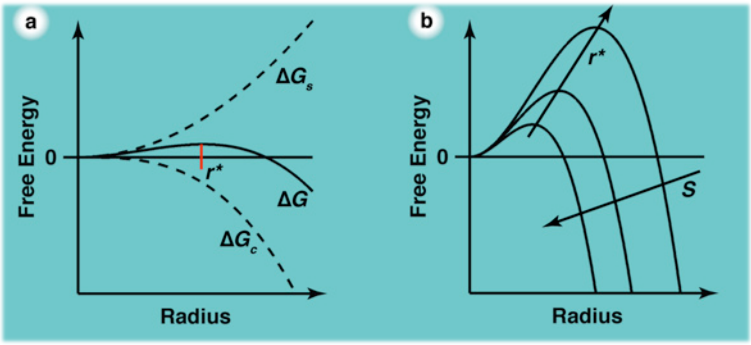

Figure 1-10. (a) Gibbs free energy variation with radius; total (ΔG), along with surface (ΔG_S) and bulk (ΔG_C) contribution. (b) Variation of free energy at different supersaturation values.

The classical nucleation theory (CNT) assumes the rate of nucleation, number of nuclei formed per unit time, as a quasiequilibrium process that follows Arrhenius approach

$$j = A\exp\left(-\frac{\Delta G^*}{k_B T}\right) \tag{17}$$

in which ΔG^* is the free energy at r^* and A is a frequency factor related to the frequency with which the system attempts to overcome the energy barrier over the density of sites available; an increase in the concentration brings an increase of nucleation rate and stable nuclei with a lower r. Due to the existence of an effective critical energy, a supersaturated solution with a low S gives rise to a metastable solution. In such a situation, only pre–existing crystals or crystal seeds would undergo growth and homogeneous nucleation is virtually absent. Nucleation is more likely to occur via a heterogeneous path by interaction with foreign particles or the vessel.

CNT states that the formation of nuclei takes place in a supersaturated solution [128] and that growth occurs by continuous addition of elementary units (ions) in an ordered fashion to reach the critical size. An interesting experiment by Gebauer [129], instead proved the presence of precursors, small clusters formed in undersaturated solutions. This led to the formulation of a general alternative route for nucleation (Figure 1-11).

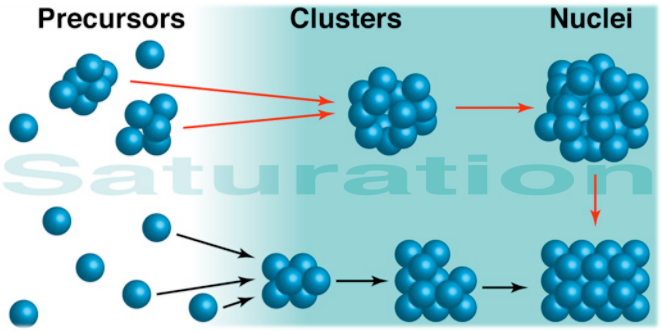

Figure 1-11. Description of CNT nucleation process (black arrows) and two-step process (red arrows).

Clusters are effectively precursors to the proper nucleation phase that arise from the agglomeration of the latter mentioned clusters [128]. The formation of a solid phase implies an inner structure, a defined distribution of atoms or molecules; while the precursors presumably have an amorphous structure [130], the final crystal has a well-defined and reproducible distribution of the elementary units. The passage from the initial clusters to the crystal nucleus involves thermodynamic and kinetic arguments: a metastable phase with a structure closer to its precursor is facilitated to nucleate, the energy barrier for a reconstruction is lower and the kinetics is faster. While at a macro scale (final crystal) the physical properties are independent from the size, because nanoscale properties can vary with the size, the surface energy can be influenced by the curvature of the surface [131], and have a different effect with the size of the particle, which has a strong impact on the cluster free energy. A particular polymorph can be favourable in a particular size range and then a reconstruction can occur to achieve a more stable polymorph (Figure 1-12).

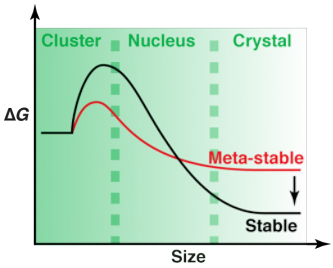

Figure 1-12. Free energy path for two polymorphs.

A complete reconstruction to attain a stable polymorph is a process that can be overtaken by kinetics. Notably, at high driving forces (high-supersaturation) the first available process is the formation of an amorphous nucleus and a high nucleation rate promotes secondary nucleation on pre–existing particles, giving birth to a dendritic growth [132]. A number of works on calcium carbonate nucleation evidence of the formation of amorphous $CaCO_3$ particles [133], and only later, does a phase change occur to a stable polymorph.

1.4.1.2 Growth Phase

The growth process of crystals occurs via a series of steps: mass transport of elementary units (ions, molecules) from the solution to the surface of the crystal, adsorption and mobility at the surface on the crystal surface, followed by incorporation into the crystal (Figure 1-13a)

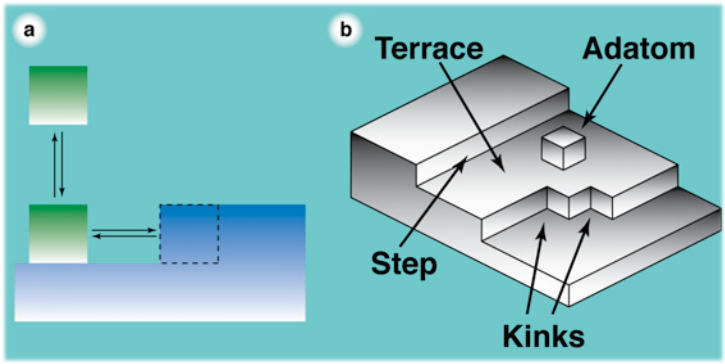

Figure 1-13. Growth process.

According to Kossel, Stranski and Volmer theory (KSV) [134-136] incorporation is energetically preferential at defect sites; a kink represents the most energetically favoured incorporation site since the units have three interaction points (Figure 1-13b), followed by a terrace step and the surface of the terrace itself. The growth of the crystal occurs layer by layer resulting in a movement of the steps across the surface.

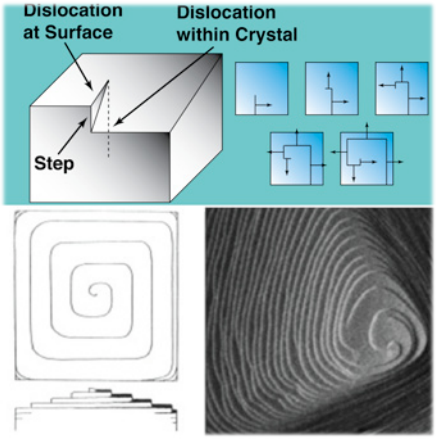

Figure 1-14. Spiral growth description, (reproduced from reference[137]).

For this mechanism to occur, pre–existing terraces have to be present on the surface of the crystals. Structural defects are a common feature on real crystals and, as noted by Frank [138], screw dislocations are present in almost all the crystals. A screw dislocation results from a bulk defect of the crystal structure and evolves in a three-dimensional spiral that acts as an infinite source of steps (Figure 1-14) which allows a continuous growth. The related growth mechanism was explained by Burton–Cabrera–Frank (BCF) [139-143], who developed a theory describing the growth of a crystal face as movement of steps that has been validated by a number of works that investigate the phenomenon at the microscale, for example employing atomic force microscopy (AFM) to image the spiral growth [144-146]. Crystal growth via spiral enlargement is mainly encountered at low supersaturations, while at high driving forces a different type

of growth starts to be relevant, namely the nucleation of two-dimensional clusters on the surface of the crystal. The nucleation of a cluster has a high energy barrier and only at high driving force can be considered effective. The formation of a new two dimensional nucleus on the surface provides new steps that can undergo growth [147]. Multi-nucleation can also take place and a synergetic growth due to the intersection of several growing clusters on the same surface has also to be considered [126] (Figure 1-15).

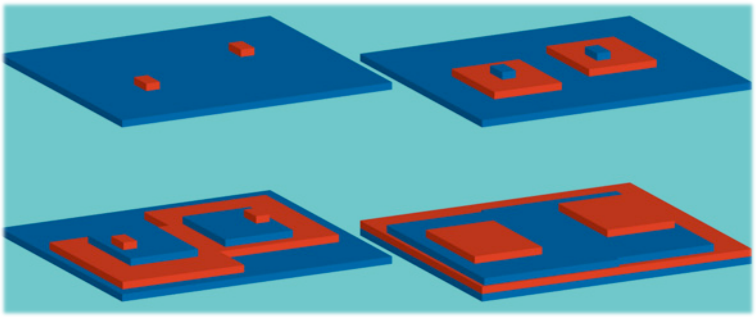

Figure 1-15. Two dimensional nucleation.

1.4.2 Polymorphism

Polymorphism is the characteristic of a material to exist in different crystal structures, starting from the same elemental units (atoms or molecule). A typical example is calcium carbonate that is found in nature in three different polymorphs: vaterite, aragonite and calcite [148]. Each polymorph has a different thermodynamic stability and only the most stable polymorph lasts over time; the others are defined as metastable. The Ostwald step rule [149] describes this evolution as a sequence of metastable phases that the system visits before achieving the final and more thermodynamically stable polymorph [150] (Figure 1-16). The nucleation of the less stable polymorph is connected to kinetic

arguments, normally a less stable polymorph is associated to a lower energy barrier, hence quicker kinetics [151].

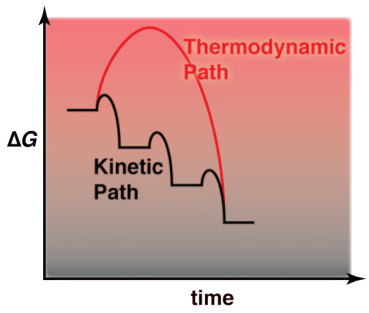

Figure 1-16. Thermodynamic vs kinetic path during crystallisation.

At high-supersaturation, where kinetics dominate, it is easier to obtain an unstable polymorph, but as shown by Boistelle [152], shortly after the supersaturation of the solution decreases, growth slows and a phase change to a more stable phase occurs. In fact, at low supersaturation the most stable polymorph is normally the first to form. In this situation the thermodynamic stability is more influential than kinetic effects [153].

1.4.3 Additives

Addition of small or large molecules to growth media can have an enormous impact upon the nucleation and crystallization as showed, for example, by Cai [154]. The presence of a polymer stabilised the formation of amorphous calcium carbonate (ACC) and after a dissolution/recrystallisation process formation of hollow sphere vaterite occurred. The interaction of additives with crystals can affect the structure or aggregation of the crystals [155], changing the properties of the final crystal. In nature many organisms employ organic molecules to stabilise particular polymorphs [156, 157] or to induce specific

shapes at the macroscale [158] which results in different properties of the final crystal [159-161]. An inhibition effect [162-164] can be obtained as well and this is of paramount importance for industrial and domestic purposes. These issues are further discussed in chapter 7 and 8.

1.5 Aims of this Thesis

The work presented in this thesis is focused on investigations of the deposition of materials on solid substrates: encompassing molecules, nanoparticles and crystals. Studies span the nanoscale, to micrometer scale, and the influence on the deposition of experimental conditions and procedures is a key focus.

Functionalisation of electrodes is an important field, because the ability to improve the catalytic activity of a conductive surface is of paramount importance for sensors and fuel cell development. Chapter 3 is focused on the functionalisation of an electrode at the molecular level. These studies were carried out to obtain a redox functionalised metal surface with metal complexes with recognition site to open up a pathway for non-covalent molecular wires.

In chapter 4 and 5 the main aims were to develop novel techniques to obtain metal nanoparticle functionalised electrodes. Two different procedure were investigated: in chapter 4, Nafion ultrathin films deposited on indium tin oxide glass slides were employed as templates for the chemical production of palladium nanoparticles; while the protocol developed in chapter 5 focused on the surface assembly of platinum nanoparticles from solution. In both of these

chapters, the final aim was to achieve a catalytic substrate for oxygen and hydrogen electrochemical reactions.

On a different length scale, chapter 6, 7 and 8 develops methodology to evaluate the scaling properties of calcium carbonate from high-supersaturated solutions. To achieve new insights on the deposition mechanism in this extreme condition, a solution delivery system was developed and coupled with quartz crystal microbalance and optical microscopy.

Deposition of calcium carbonate at high-supersaturated condition presents different mechanism compared to low supersaturation solution, and in chapter 6 a series of experiments are reported to gain insight into these mechanisms using the experimental delivery system developed. In chapter 7, the same system was employed to obtain quantitative analysis of the influence of citrate concentration on calcium carbonate deposition. Investigations of the effect of additives on calcium carbonate scaling process are of primary importance for every day life and in the industrial field. The development of a reliable, efficient and quick methodology to evaluate anti–scaling properties of different additives was considered extremely useful for this purpose, and chapter 8 reports studies of a series of different commercial inhibitors exploiting the system developed.

1.6 Bibliography

[1] Somorjai, G. A.; *Introduction to Surface Chemistry and Catalysis*; Wiley-interscience publication: United States of America, 1994.

[2] Ostwald, W.; *Lehrbuch der Allgemeinen Chemie* **1896**, *2*.

[3] Conrad, H.; Ertl, G.; Latta, E. E.; *Surf. Sci.* **1974**, *41*, 435-446.

[4] Yeager, E.; *Electrochim. Acta* **1984**, *29*, 1527-1537.

[5] Che, M.; Bennett, C. O.; *Adv Cat* **1989**, *36*, 55-172.

[6] Valden, M.; Lai, X.; Goodman, D. W.; *Science* **1998**, *281*, 1647-1650.

[7] Gates, B. C.; *Chem. Rev.* **1995**, *95*, 511-522.

[8] Schwartz, D. K.; *Annu. Rev. Phys. Chem.* **2001**, *52*, 107-137.

[9] Cygan, M. T.; Dunbar, T. D.; Arnold, J. J.; Bumm, L. A.; Shedlock, N. F.; Burgin, T. P.; Jones, L.; Allara, D. L.; Tour, J. M.; Weiss, P. S.; *JACS* **1998**, *120*, 2721-2732.

[10] de Boer, B.; Meng, H.; Perepichka, D. F.; Zheng, J.; Frank, M. M.; Chabal, Y. J.; Bao, Z.; *Langmuir* **2003**, *19*, 4272-4284.

[11] Gao, Z.; Siow, K. S.; Chan, H. S. O.; *Synt. Met.* **1995**, *75*, 5-10.

[12] Chabinyc, M. L.; Love, J. C.; Thywissen, J. H.; Cervelli, F.; Prentiss, M. G.; Whitesides, G. M.; *Langmuir* **2003**, *19*, 2201-2205.

[13] Berggren, K. K.; Bard, A.; Wilbur, J. L.; Gillaspy, J. D.; Helg, A. G.; McClelland, J. J.; Rolston, S. L.; Phillips, W. D.; Prentiss, M.; Whitesides, G. M.; *Science* **1995**, *269*, 1255-1257.

[14] Golzhauser, A.; Eck, W.; Geyer, W.; Stadler, V.; Weimann, T.;

Hinze, P.; Grunze, M.; *Adv. Mater.* **2001**, *13*, 806-809.

[15] Ginger, D. S.; Zhang, H.; Mirkin, C. A.; *Angew. Chem. Int. Ed.* **2004**, *43*, 30-45.

[16] Kramer, S.; Fuierer, R. R.; Gorman, C. B.; *Chem. Rev.* **2003**, *103*, 4367-4418.

[17] Liu, G. Y.; Xu, S.; Qian, Y. L.; *Acc. Chem. Res.* **2000**, *33*, 457-466.

[18] Xia, Y. N.; Whitesides, G. M.; *Angew. Chem. Int. Ed.* **1998**, *37*, 551-575.

[19] Stranick, S. J.; Parikh, A. N.; Tao, Y. T.; Allara, D. L.; Weiss, P. S.; *J. Phys. Chem.* **1994**, *98*, 7636-7646.

[20] Stranick, S. J.; Atre, S. V.; Parikh, A. N.; Wood, M. C.; Allara, D. L.; Winograd, N.; Weiss, P. S.; *Nanotechnology* **1996**, *7*, 438-442.

[21] Hara, K.; Akiyama, R.; Takakusagi, S.; Uosaki, K.; Yoshino, T.; Kagi, H.; Sawamura, M.; *Angew. Chem. Int. Ed. Engl.* **2008**, *47*, 5627-5630.

[22] Thomas, R. C.; Houston, J. E.; Crooks, R. M.; Kim, T.; Michalske, T. A.; *JACS* **1995**, *117*, 3830-3834.

[23] Frisk, M. L.; Tepp, W. H.; Johnson, E. A.; Beebe, D. J.; *Anal. Chem.* **2009**, *81*, 2760-2767.

[24] Collet, J.; Tharaud, O.; Chapoton, A.; Vuillaume, D.; *Appl. Phys. Lett.* **2000**, *76*, 1941.

[25] Chen, Y.; Ohlberg, D. A. A.; Li, X.; Stewart, D. R.; Williams, R. S.; Jeppesen, J. O.; Nielsen, K. A.; Stoddart, J. F.; Olynick, D. L.; Anderson, E.; *Appl. Phys. Lett.* **2003**, *82*, 1610-1612.

[26] Mantooth, B. A.; Weiss, P. S.; *P IEEE* **2003**, *91*, 1785-1802.

[27] Krings, N.; Strehblow, H. H.; Kohnert, J.; Martin, H. D.; *Electrochim. Acta* **2003**, *49*, 167-174.

[28] Clegg, R. S.; Hutchison, J. E.; *Langmuir* **1996**, *12*, 5239-5243.

[29] Ulman, A.; *Chem. Rev.* **1996**, *96*, 1533.

[30] Dubois, L. H.; Nuzzo, R. G.; *Annu. Rev. Phys. Chem.* **1992**, *43*, 437-463.

[31] Henderson, A. P.; Seetohul, L. N.; Dean, A. K.; Russell, P.; Pruneanu, S.; Ali, Z.; *Langmuir* **2009**, *25*, 931-938.

[32] Bain, C. D.; Troughton, E. B.; Tao, Y. T.; Evall, J.; Whitesides, G. M.; Nuzzo, R. G.; *JACS* **1989**, *111*, 321-335.

[33] Zhao, X. M.; Wilbur, J. L.; Whitesides, G. M.; *Langmuir* **1996**, *12*, 3257-3264.

[34] Love, J. C.; Wolfe, D. B.; Haasch, R.; Chabinyc, M. L.; Paul, K. E.; Whitesides, G. M.; Nuzzo, R. G.; *JACS* **2003**, *125*, 2597-2609.

[35] Nuzzo, R. G.; Allara, D. L.; *JACS* **1983**, *105*, 4481-4483.

[36] Nuzzo, R. G.; Fusco, F. A.; Allara, D. L.; *JACS* **1987**, *109*, 2358-2368.

[37] Fenter, P.; Eisenberger, P.; Li, J.; Camillone, N.; Bernasek, S.; Scoles, G.; Ramanarayanan, T. A.; Liang, K. S.; *Langmuir* **1991**, *7*, 2013-2016.

[38] Edinger, K.; Goelzhaeuser, A.; Demota, K.; Woll, C.; Grunze, M.; *Langmuir* **1993**, *9*, 4-8.

[39] Vos, J. G.; Forster, R. J.; Keyes, T. E.; *Interfacial Supramolecuar Assemblies*; Jhon Wiley & Sons, Ltd: 2003.

[40] Bryant, M. A.; Pemberton, J. E.; *JACS* **1991**, *113*, 8284-8293.

[41] Nuzzo, R. G.; Dubois, L. H.; Allara, D. L.; *JACS* **1990**, *112*, 558-

569.

[42] Li, Y.; Huang, J.; McIver, R. T.; Hemminger, J. C.; *JACS* **1992**, *114*, 2428-2432.

[43] Shimazu, K.; Yagi, I.; Sato, Y.; Uosaki, K.; *Langmuir* **1992**, *8*, 1385-1387.

[44] Kim, Y. T.; McCarley, R. L.; Bard, A. J.; *Langmuir* **1993**, *9*, 1941-1944.

[45] Li, D.; Ratner, M. A.; Marks, T. J.; Zhang, C.; Yang, J.; Wong, G. K.; *JACS* **1990**, *112*, 7389-7390.

[46] Laibinis, P. E.; Whitesides, G. M.; Allara, D. L.; Tao, Y. T.; Parikh, A. N.; Nuzzo, R. G.; *JACS* **1991**, *113*, 7152-7167.

[47] Li, Z.; Chang, S. C.; Williams, R. S.; *Langmuir* **2003**, *19*, 6744-6749.

[48] Shnidman, Y.; Ulman, A.; Eilers, J. E.; *Langmuir* **1993**, *9*, 1071-1081.

[49] Evans, S. D.; Urankar, E.; Ulman, A.; Ferris, N.; *JACS* **1991**, *113*, 4121-4131.

[50] Tam-Chang, S. W.; Biebuyck, H. A.; Whitesides, G. M.; Jeon, N.; Nuzzo, R. G.; *Langmuir* **1995**, *11*, 4371-4382.

[51] Poirier, G. E.; *Chem. Rev.* **1997**, *97*, 1117-1128.

[52] Yang, G.; Liu, G. -Y.; *J. Phys. Chem. B* **2003**, *107*, 8746-8759.

[53] Bishop, A. R.; Nuzzo, R. G.; *Curr. Opin. Colloid Interface Sci.* **1996**, *1*, 127-136.

[54] Dannenberger, O.; Wolff, J. J.; Buck, M.; *Langmuir* **1998**, *14*, 4679-4682.

[55] Peterlinz, K. A.; Georgiadis, R.; *Langmuir* **1996**, *12*, 4731-4740.

[56] Yamada, R.; Sakai, H.; Uosaki, K.; *Chemistry Letters* **1999**, 667-668.

[57] Schneider, T. W.; Buttry, D. A.; *JACS* **1993**, *115*, 12391-12397.

[58] Walczak, M. M.; Popenoe, D. D.; Deinhammer, R. S.; Lamp, B. D.; Chung, C.; Porter, M. D.; *Langmuir* **1991**, *7*, 2687-2693.

[59] Widrig, C. A.; Chung, C.; Porter, M. D.; *J. Electroanal. Chem.* **1991**, *310*, 335-359.

[60] Williams, J. A.; Gorman, C. B.; *J. Phys. Chem.* **2007**, *111*, 12804-12810.

[61] Finklea, H. O.; Robinson, L. R.; Blackburn, A.; Richter, B.; Allara, D.; Bright, T.; *Langmuir* **1986**, *2*, 239-244.

[62] Weisshaar, D. E.; Lamp, B. D.; Porter, M. D.; *JACS* **1992**, *114*, 5860-5862.

[63] Smith, C. P.; White, H. S.; *Langmuir* **1993**, *9*, 1-3.

[64] Smith, C. P.; White, H. S.; *Anal. Chem.* **1992**, *64*, 2398-2405.

[65] Vuillaume, D.; Boulas, C.; Collet, J.; Davidovits, J. V.; Rondelez, F.; *Appl. Phys. Lett.* **1996**, *69*, 1646.

[66] Tran, E.; Grave, C.; Whitesides, G. M.; Rampi, M. A.; *Electrochim. Acta* **2005**, *50*, 4850-4856.

[67] Forster, R. J.; Faulkner, L. R.; *JACS* **1994**, *116*, 5444-5452.

[68] Zapotoczny, S.; Auletta, T.; de Jong, M. R.; Schonherr, H.; Huskens, J.; van Veggel, F. C. J. M.; Reinhoudt, D. N.; Vancso, G. J.; *Langmuir* **2002**, *18*, 6988-6994.

[69] Creager, S. E.; Wooster, T. T.; others; *Anal. Chem.* **1998**, *70*,

4257-4263.

[70] Smalley, J. F.; Finklea, H. O.; Chidsey, C. E.; Linford, M. R.; Creager, S. E.; Ferraris, J. P.; Chalfant, K.; Zawodzinsk, T.; Feldberg, S. W.; Newton, M. D.; *JACS* **2003**, *125*, 2004-2013.

[71] Weber, K.; Hockett, L.; Creager, S.; *J. Phys. Chem. B* **1997**, *101*, 8286-8291.

[72] Bard, A. J.; Faulkner, L. R.; *Electrochemical methods: fundamentals and applications* , 2nd ed.; John Wiley & Sons, Inc.: United States of America, 2001.

[73] Marcus, R. A.; *J. Chem. Phys.* **1965**, *43*, 679.

[74] Newton, M. D.; Sutin, N.; *Annu. Rev. Phys. Chem.* **1984**, *35*, 437-480.

[75] Laviron, E.; Roullier, L.; *J. Electroanal. Chem.* **1980**, *115*, .

[76] Rowe, G. K.; Creager, S. E.; *Langmuir* **1991**, *7*, 2307-2312.

[77] Giersig, M.; Mulvaney, P.; *Langmuir* **1993**, *9*, 3408-3413.

[78] Burda, C.; Chen, X. B.; Narayanan, R.; El-Sayed, M. A.; *Chem. Rev.* **2005**, *105*, 1025-1102.

[79] McEuen, P. L.; *Science* **1997**, *278*, 1729-1730.

[80] Julien, F. H.; Alexandrou, A.; *Science* **1998**, *282*, 1429-1430.

[81] Weller, H.; *Angew. Chem. Int. Ed. Engl.* **1993**, *32*, 41-53.

[82] Empedocles, S. A.; Neuhauser, R.; Shimizu, K.; Bawendi, M. G.; *Adv. Mater.* **1999**, *11*, 1243-1256.

[83] Falsig, H.; Hvolbaek, B.; Kristensen, I. S.; Jiang, T.; Bligaard, T.; Christensen, C. H.; Nørskov, J. K.; *Angew. Chem. Int. Ed. Engl.* **2008**, *47*, 4835-4839.

[84] Solla-Gullón, J.; Rodriguez, P.; Herrero, E.; Aldaz, A.; Feliu, J. M.; *Phys. Chem. Chem. Phys.* **2008**, *10*, 1359-1373.

[85] Vajda, S.; Pellin, M. J.; Greeley, J. P.; Marshall, C. L.; Curtiss, L. A.; Ballentine, G. A.; Elam, J. W.; Catillon-Mucherie, S.; Redfern, P. C.; Mehmood, F.; Zapol, P.; *Nat. Mater.* **2009**, *8*, 213-216.

[86] Karam, P.; Halaoui, L. I.; *Anal. Chem.* **2008**, *80*, 5441-5448.

[87] Shipway, A. N.; Katz, K.; Willner, I.; *ChemPhysChem* **2000**, *1*, 18-52.

[88] Wang, F.; Hu, S.; *Microchim. Acta* **2009**, *165*, 1-22.

[89] Luo, X.; Morrin, A.; Killard, A. J.; Smyth, M. R.; *Electroanalysis* **2006**, *18*, .

[90] Yu, B.; Meyyappan, M.; *Solid-State Electron.* **2006**, *50*, 536-544.

[91] Katz, E.; Willner, I.; Wang, J.; *Electroanal.* **2004**, *16*, 19-44.

[92] Aiken, J. D.; Finke, R. G.; *J. Mol. Catal. A: Chem.* **1999**, *145*, 1-44.

[93] Murray, C. B.; Kagan, C. R.; Bawendi, M. G.; *Annu. Rev. Mater. Sci.* **2000**, *30*, 545.

[94] Henglein, A.; Giersig, M.; *J. Phys. Chem. B* **1999**, *103*, 9533-9539.

[95] Bönnemann, H.; Braun, G.; Brijoux, W.; Brinkmann, R.; Tilling, A. S.; Seevogel, K.; Siepen, K.; *J. Organomet. Chem.* **1996**, *520*, 143-162.

[96] Templeton, A. C.; Wuelfing, W. P.; Murray, R. W.; *Acc. Chem. Res.* **2000**, *33*, 27-36.

[97] Brust, M.; Walker, M.; Bethell, D.; Schiffrin, D. J.; Whyman, R.; *J. Chem. Soc., Chem. Commun.* **1994**, *1994*, 801-802.

[98] Chen, S.; Kimura, K.; *Langmuir* **1999**, *15*, 1075-1082.

[99] Hatzor, A.; Weiss, P.; *Science* **2001**, *291*, 1019-1020.

[100] Peng, X.; Manna, L.; Yang, W.; Wickham, J.; Scher, E.; Kadavanich, A.; Alivisatos, A. P.; *Nature* **2000**, *404*, 59-61.

[101] Brown, K. R.; Natan, M. J.; *Langmuir* **1998**, *14*, 726-728.

[102] Salimi, A.; Sharifi, E.; Noorbakhsh, A.; Soltanian, S.; *Biosens. Bioelectron.* **2007**, *22*, 3146-3153.

[103] Penner, R. M.; *J. Phys. Chem. B* **2002**, *106*, 3339-3353.

[104] Bönnemann, H.; Brijoux, W.; *Advanced Catalysts and Nanostructured Materials*; W.Moser, Academic Press: New York, 1996.

[105] Zoval, J. V.; Stiger, R. M.; Biernacki, P. R.; Penner, R. M.; *J. Phys. Chem.* **1996**, *100*, 837-844.

[106] Zoval, J. V.; Lee, J.; Gorer, S.; Penner, R. M.; *J. Phys. Chem. B* **1998**, *102*, 1166-1175.

[107] Penner, R. M.; *J. Phys. Chem. B* **2001**, *105*, 8672-8678.

[108] Liu, H.; Penner, R. M.; *J. Phys. Chem. B* **2000**, *104*, 9131-9139.

[109] Fransaer, J. L.; Penner, R. M.; *J. Phys. Chem. B* **1999**, *103*, 7643-7653.

[110] O'Mullane, A. P.; Dale, S. E.; Macpherson, J. V.; Unwin, P. R.; *Chem. Commun.* **2004**, 1606-1607.

[111] Sun, Y. P.; Atorngitjawat, P.; Lin, Y.; Liu, P.; Pathak, P.; Bandara, J.; Elgin, D.; Zhang, M.; *J. Membr. Sci* **2004**, *245*, 211-217.

[112] Mandal, S.; Roy, D.; Chaudhari, R. V.; Sastry, M.; *Chem. Mater.* **2004**, *16*, 3714-3724.

[113] Astruc, D.; Daniel, M. C.; Ruiz, J.; *Chem. Commun.* **2004**, 2637-

2649.

[114] Rollins, H. W.; Lin, F.; Johnson, J.; Ma, J. J.; Liu, J. T.; Tu, M. H.; DesMarteau, D. D.; Sun, Y. P.; *Langmuir* **2000**, *16*, 8031-8036.

[115] Devanath, M. A. V.; others, O.; *J. Solid State Electrochem.*, *5*, 274-279.

[116] Ye, H.; Crooks, R. M.; *JACS* **2005**, *127*, 4930-4934.

[117] Scott, R. W. J.; Wilson, O. M.; Crooks, R. M.; *J. Phys. Chem. B* **2005**, *109*, 692-704.

[118] Luquet, G.; Marin, F.; *Comptes rendus-Palevol* **2004**, *3*, 515-534.

[119] Charola, A. E.; Pühringer, J.; Steiger, M.; *Environmental Geology* **2007**, *52*, 207-220.

[120] Al-Anezi, K.; Hilal, N.; *Desalination* **2007**, *204*, 385-402.

[121] Amor, M. B.; Zgolli, D.; Tlili, M. M.; Manzola, A. S.; *Desalination* **2004**, *166*, 79-84.

[122] Smith, B. L.; Schäffer, T. E.; Viani, M.; Thompson, J. B.; Frederick, N. A.; Kindt, J.; Belcher, A.; Stucky, G. D.; Morse, D. E.; Hansma, P. K.; *Nature* **1999**, *399*, 761-763.

[123] Aizenberg, J.; Weaver, J. C.; Thanawala, M. S.; Sundar, V. C.; Morse, D. E.; Fratzl, P.; *Science* **2005**, *309*, 275-278.

[124] Weiner, S.; Addadi, L.; *J. Mater. Chem.* **1997**, *7*, 689-702.

[125] Addadi, L.; Raz, S.; Weiner, S.; *Adv. Mater.* **2003**, *15*, 959-970.

[126] Nielsen, A. E.; Toft, J. M.; *J. Cryst. Growth* **1984**, *67*, 278-288.

[127] Teng, H. H.; Dove, P. M.; De Yoreo, J. J.; *Geochim. Cosmchim. Acta* **2000**, *64*, 2255-2266.

[128] Garside, J.; Larson, M. A.; *Chem. Eng. Sci.* **1986**, *41*, 1285-1289.

[129] Gebauer, D.; Völkel, A.; Cölfen, H.; *Science* **2008**, *322*, 1819-1822.

[130] Zhang, T. H.; Liu, X. Y.; *Angew. Chem.* **2009**, *121*, .

[131] Schmelzer, J. W. P.; Gutzow, I.; Schmelzer, J.; *J. Colloid Interface Sci.* **1996**, *178*, 657-665.

[132] Oaki, Y.; Imai, H.; *Crystal Growth & Design* **2003**, *3*, 711-716.

[133] Rieger, J.; Thieme, J.; Schmidt, C.; *Langmuir* **2000**, *16*, 8300-8305.

[134] Kossel, W.; *Nachr. Ges. Wiss. Gottingen Math.-phys. Klasse* **1927**, 135-143.

[135] Stranski, I. N.; *Z. Phys. Chem* **1928**, *136*, 259.

[136] Brandes, H.; Volmer, M.; *Z. Phys. Chem* **1931**, *155*, 466.

[137] Kwon, Y. I.; Dai, B.; Derby, J. J.; *Prog. Cryst. Growth and Charact. Mater.* **2007**, *53*, 167-206.

[138] Frank, F. C.; *Faraday Discuss.* **1949**, *5*, 48-54.

[139] Burton, W. K.; Cabrera, N.; *Faraday Discuss.* **1949**, *5*, 33-39.

[140] Bennema, P.; *J. Cryst. Growth* **1967**, *1*, 287-292.

[141] Bennema, P.; *J. Cryst. Growth* **1967**, *1*, 278-286.

[142] Cabrera, N.; Burton, W. K.; *Faraday Discuss.* **1949**, *5*, 40-48.

[143] Koutsopoulos, S.; *Langmuir* **2001**, *17*, 8092-8097.

[144] Dobson, P. S.; Bindley, L. A.; Macpherson, J. V.; Unwin, P. R.; *Langmuir* **2005**, *21*, 1255-1260.

[145] Bosbach, D.; Junta-Rosso, J. L.; Becker, U.; Hochella, M. F.; *Geochim. Cosmchim. Acta* **1996**, *60*, 3295-3304.

[146] Teng, H. H.; Dove, P. M.; DeYoreo, J. J.; *Geochim. Cosmchim.*

Acta **1999**, *63*, 2507-2512.

[147] van Kemenade, M. J. J. M. V.; de Bruyn, P. L.; *J. Colloid Interface Sci.* **1987**, *118*, 564-585.

[148] Clarkson, J. R.; Price, T. J.; Adams, C. J.; *J. Chem. Soc. Faraday Trans.* **1992**, *88*, 243-249.

[149] Ostwald, W.; *Z. Phys. Chem* **1897**, *22*, 289.

[150] Kitamura, M.; *Pure Appl. Chem.* **2005**, *77*, 581-591.

[151] Söhnel, O.; Mullin, J. W.; *J. Cryst. Growth* **1982**, *60*, 239-250.

[152] Boistelle, R.; Astier, J. P.; *J. Cryst. Growth* **1988**, *90*, 14-30.

[153] Bernstein, J.; Davey, R. J.; Henck, J. O.; *Angew. Chem. Int. Ed.* **1999**, *38*, 3440-3461.

[154] Cai, A.; Xu, X.; Pan, H.; Tao, J.; Liu, R.; Tang, R.; Cho, K.; *J. Phys. Chem. C* **2008**, *112*, 11324-11330.

[155] Falini, G.; Fermani, S.; Goisis, M.; Manganelli, G.; *J. Cryst. Growth Des.* **2009**, *9*, 153-169.

[156] Elhadj, S.; De Yoreo, J. J.; Hoyer, J. R.; Dove, P. M.; *PNAS* **2006**, *103*, 19237-19242.

[157] Berman, A.; Addadi, L.; Weiner, S.; *Nature* **1988**, *331*, 546-548.

[158] Falini, G.; Albeck, S.; Weiner, S.; Addadi, L.; *Science* **1996**, *271*, 67.

[159] Meldrum, F. C.; *Int. Mater. Rev.* **2003**, *48*, 187-224.

[160] Wu, W.; Nancollas, G. H.; *Colloids Surf., B* **1997**, *10*, 87-94.

[161] Walsh, D.; Kingston, J. L.; Heywood, B. R.; Mann, S.; *J. Cryst. Growth* **1993**, *133*, 1-12.

[162] Mann, S.; Didymus, J. M.; Sanderson, N. P.; Heywood, B. R.;

Samper, E. J. A.; *J. Chem. Soc. Faraday Trans.* **1990**, *86*, 1873-1880.

[163] HOUSE, W. A.; *J. Colloid. Interface Sci.* **1987**, *119*, 505-511.

[164] Qingfeng, Y.; Yangqiao, L.; Anzhong, G.; Jie, D.; Ziqiu, S.; *J. Colloid. Interface Sci.* **2001**, *240*, 608-621.

Chapter 2 EXPERIMENTAL

2.1 Chemicals

All the aqueous solutions were prepared using Milli-Q reagent water (Millipore Corp.) with a resistivity ≥18 MΩ cm at 25 °C.

Table 2-1. List of chemical employed.

Chemical	*Purity/Grade*	*Supplier*
Acetonitrile (CH_3CN)	HPLC Grade	Fisher Scientific
Alumina		Buehler, USA
Calcium chloride dihydrate ($CaCl_2$ x$2H_2O$)	99%	Sigma ultra
Sodium hydrogen carbonate ($NaHCO_3$)	AnalR 99.5%	BDH
Dimethylformamide (DMF)	HPLC grade	Aldrich
Ethanol (C_2H_5OH)	Analytical reagent Grade	Aldrich
Hydrochloric acid (HCl)	Analytical reagent Grade, 37%	Fisher Scientific
K_2PtCl_4	99.9%	H. Drijfhout & Zoon's Edelmetaalbedrijven B.V.
Methanol (MeOH)	HPLC Grade	Fisher Scientific
Metyl-viologen dichlororide hydrate (MV)	98%	Aldrich
Mono potassium phosphate (KH_2PO_4)	Analytical reagent Grade	Fisher Scientific

Chemical	*Purity/Grade*	*Supplier*
Nafion® 117 Perfluorinated ion-exchange resin	5 wt% in aliphatic alcohol/H_2O	Aldrich
Nitric acid (HNO_3)	Analytical reagent Grade	Fisher Scientific
Palladium nitrate ($PdNO_3$)	99.99% ($10\%_{wt}$ Pd^{2+}, $10\%_{wt}$ HNO_3)	Aldrich
Potassium hydrogen phthalate ($KHC_8H_4O_4$)	Analytical reagent Grade	Fisher Scientific
Potassium nitrate (KNO_3)	Analytical reagent Grade	Fisher Scientific
Sodium borohydride ($NaBH_4$)	99%	Aldrich
Sodium Chloride (NaCl)	Analytical reagent Grade	Aldrich
Sodium dihydrogen citrate ($NaH_2C_6H_5O_7$)	Analytical reagent Grade	Aldrich
Sodium hydroxide (NaOH)	97%	Fisher Scientific
tetra-butyl ammonium hesaflouro-phosphate ($tBAPF_6$)	98%	Aldrich
tetra-butyl ammonium perchlorate ($tBAClO_4$)	99%	Fluka
Acetone (C_3H_6O)	Analytical reagent Grade	Aldrich
Isopropanol alcohol (C_3H_8O)	Analytical reagent Grade	Aldrich
1-Butyl-3-methylimidazolium hexafluorophosphate (BMI)		Fluka

Table 2-2. Buffers employed.

Buffer composition	*pH*
KHPhthalate/HCl	3.0 ±0.1
KHPhthalate/NaOH	4.0 ±0.1
KHPhthalate/NaOH	5.0 ±0.1
KH_2Phosphate/NaOH	7.0 ±0.1

2.2 General Materials

Microscopy slides: VWR International (UK).

Indium tin oxide (ITO) glass plate electrodes: from Delta Technologies Ltd., Stillwater (USA), these had square resistance, Rs ≤10 Ω. ITO glass plates were sonicated in isopropanol, acetone and chloroform for at least 5 minutes before use. The substrates were dried using nitrogen and, before use, the substrates were cleaned with chloroform.

Highly oriented pyrolytic graphite (HOPG): From PI Supplies, West Chester (PA, USA), SPI-1 grade, 10 mm x10 mm x2 mm. Freshly prepared surfaces were obtained by cleaving using adhesive tape. The HOPG was fixed to a silicon slide coated with Cr/Au for electrical contact.

Glass substrates for $CaCO_3$ deposition: The slides were from Logitech ltd (UK), they were 1.25 mm thick and used for in–situ optical microscopy investigations. They were cleaned using pirana solution (H_2SO_4 : H_2O_2 3 : 1)[#] at 80 °C for 60 minutes.

Quartz crystals: The QCM probes were from IJ Cambria Scientific, Wales (UK). They were gold coated quartz crystals.

2.3 General Instrumentation

Luminecence: luminescence studies were performed on a Quanta-Master QM-1 steady-state emission spectrometer from Photon Technology Instruments equipped with a 75 W xenon arc lamp and a model 810 photon-counting detection system with a red sensitive R928 photomultiplier tube. The

[#] Special disposal procedure.

luminescence spectra were not corrected for photomultiplier response due to the weak signal. The excitation spectra were corrected for lamp and instrument response. All spectra were recorded using PTI Felix fluorescence analysis software for Windows. Absorption spectra were recorded on a Shimadzu UV-3101PC Uv/Vis/NIR spectrometer.

Transmission electron microscopy (TEM): a JEOL 2000fx TEM was used.

Field emission scanning electron microscopy (FE-SEM): a Zeiss SUPRA 55 VP FE-SEM was used. The samples were coated with gold before imaging.

Atomic force microscopy (AFM): either tapping mode (TM-AFM) or contact mode were performed using a Digital Instruments Multimode AFM and Nanoscope IIIa controller, Veeco (USA), and Si tips (LOT-Oriel, UK) were employed.

Micro-Raman spectroscopy: a Renishaw inVia Raman Microscope with incorporated Leica microscope and CCD detector was used. The parameters used were: 514.5 nm (2.41 eV) excitation wavelength of an Ar laser, at 10 mW power, focused in a 10 μm spot.

Optical microscopy: the microscope was a Leica DM4000 M with a CCD camera DFC490. This was used for the optical flow cell-crystal growth experiments.

Quartz crystal microbalance (QCM): a CHI400 EQCM from IJ Cambria Scientific, Wales (UK), was used.

pH-Meter: from Denver instruments UB-10, (UK).

2.4 Electrochemical Instrumentation

All the electrochemical investigations, linear sweep voltammetry (LSV), cyclic voltammetry (CV), chronoamperometry (CA), were performed using a potentiostat (Electrochemical Analyzer CHI 730A, IJ Cambridge Scientific, Cambridge, UK) controlled by a PC, using either two or three electrode setups, further details are shown in the relevant chapters (chapters 3, 4 and 5).

Table 2-3. Reference and working electrodes employed.

Electrode	*Description*
Ag/AgCl	Silver chloride coated silver wire reference electrode
AgQRE	Silver wire quasi reference electrode
SCE	Saturated calomel reference electrode (CH Instruments, UK)
Pt-working electrode	Platinum macro working electrode, 2 mm diameter disc (CHI 102, CH Instruments, UK)
Pt/Au-UME	Ultramicroelectrode, platinum or gold with 25 or 50 µm diameter disc (built in house)

2.4.1 Cleaning Procedure for Platinum Micro and Macro Electrodes

The platinum disk UMEs, (25 µm and 50 µm) and platinum macroelectrode were polished on a microcloth pad (Microcloth 2-7/8 Buehler, USA) immersed in a solution of water and alumina. Electrochemical cleaning was then performed in H_2SO_4 (0.1 M) cycling between 1 V and -0.50 V vs

Ag/AgCl reference electrode, for an average of 30 cycles (Figure 2-1) until well-defined typical features of polycrystalline platinum were recognised, including hydrogen adsorption/desorption, and platinum oxidation/reduction [1]. Because oxidation/reduction process of platinum electrode surfaces increases roughness, excessive cycling was avoided. In order to reduce the platinum surface, desorb the hydrogen adsorbed during the electrocleaning, a fixed potential of -0.15 V was applied for 90 s.

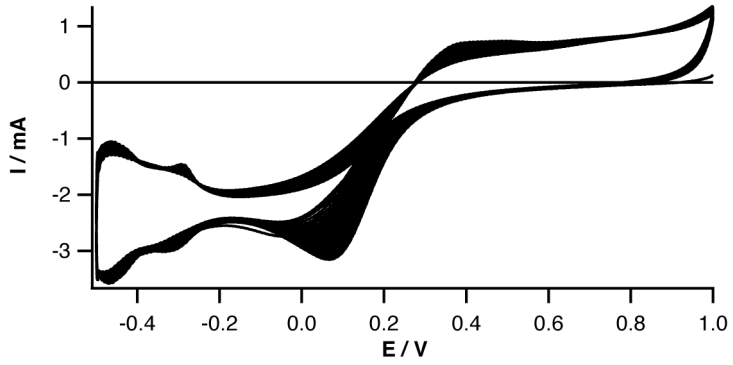

Figure 2-1. Electrocleaning CVs of Pt-UME, 25 µm diameter, in H_2SO_4 (0.1 M) solution.

2.5 Flow System for Investigation of Calcium Carbonate Deposition

A flow system (Figure 2-2) that allowed the mixing of two solutions (containing calcium and carbonate ions, respectively) with a constant flow rate and conditions was designed in house.

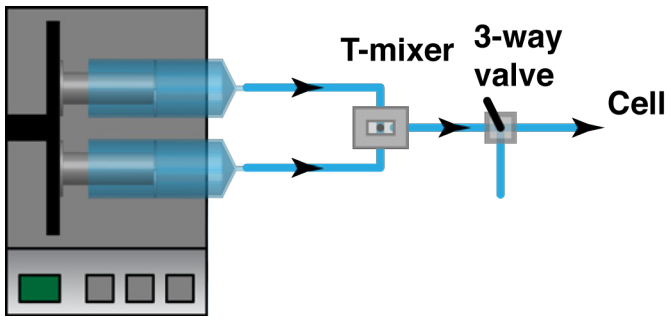

Figure 2-2. Schematic of the delivery system built in house.

2.5.1 Delivery and Mixing System

The system (Figure 2-2) was used to obtain a supersaturated solution of calcium carbonate to be delivered to two different flow cells (see below) for in–situ analysis. All the parts in contact with the solution were built with PTFE to avoid heterogeneous nucleation of calcium carbonate. Homogeneous nucleation was expected at short times due to the high-supersaturated conditions employed. Thus, to deliver a solution of calcium/carbonate with constant saturation ratio (*S*) an in–line mixing system was judged to be the most efficient method. A dual-driven syringe system (Kd Scientific mod. 200, B–D plastic syringes, 60 ml) was employed to deliver the solutions of calcium and carbonate to a custom-made T-mixer (Figure 2-3) to obtain a rapid mixing. The outlet of the mixer was connected to either the optical flow cell or the quartz microbalance (QCM) flow cell. For the flow rate of 2 ml min^{-1} (total flow rate) used, the time for the solution to reach the related cell was measured as 22 s. A 3-way valve was used to divert the incoming supersaturated solution toward the waste or to the cell and allowed the cell to be filled with water at the beginning of each experiment and to be emptied using air at the end.

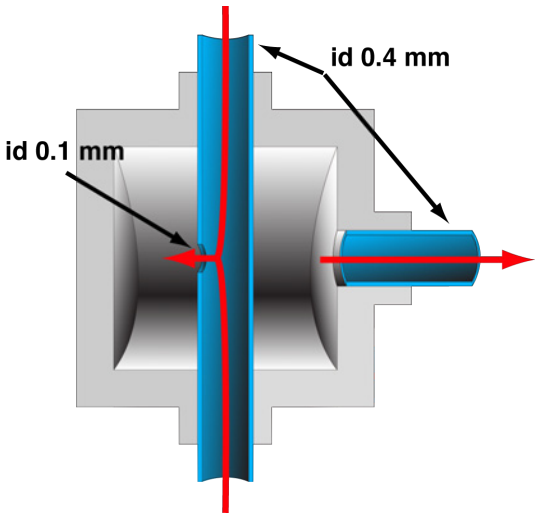

Figure 2-3. T-mixer schematic.

The system was tested to evaluate the reliability of the flow rate before and after the T-mixer. The flow rate was set at different values 0.5, 1 and 1.5 ml min^{-1} for both the channels (using different syringes containing water) and the solution before and after the T-mixer was collected and weighted at different times (30, 60 and 120 s). For each flow rate and time 10 runs were performed. Table 2-4 shows the average volume collected.

Table 2-4. Flow rate reliability test. Volume collected for channel A, B and after the T-mixer.

Set flow rate / ml min^{-1}	*Time / min*	*Exp. Vol A / ml*	*Exp. Vol B / ml*	*Exp. Vol after mix / ml*	*Exp. Flow rate / ml min^{-1}*
0.5	1	0.502 ±0.002	0.502 ±0.002	1.004 ±0.002	0.502 ±0.003
0.5	5	2.51 ±0.002	2.51 ±0.002	5.02 ±0.002	0.502 ±0.003
0.5	10	5.02 ±0.002	5.02 ±0.002	10.04 ±0.002	0.502 ±0.003
1	1	1.004 ±0.002	1.004 ±0.002	2.008 ±0.002	1.004 ±0.003
1	5	5.02 ±0.002	2.51 ±0.002	10.04 ±0.002	1.004 ±0.003
1	10	10.04 ±0.002	10.04 ±0.002	20.08 ±0.002	1.004 ±0.003
1.5	1	1.506 ±0.002	1.506 ±0.002	3.012 ±0.002	1.506 ±0.003
1.5	5	7.53 ±0.002	7.53 ±0.002	15.06 ±0.002	1.506 ±0.003
1.5	10	15.06 ±0.002	15.06 ±0.002	30.12 ±0.002	1.506 ±0.003

The test showed a really constant flow rate over time close to the set flow rate.

2.5.2 Flow Cells

Two different flow cells were developed to couple with the solution delivery system described above. The cells, a QCM-flow cell and a microscope flow cell, were employed for in–situ experiments on the deposition of calcium carbonate.

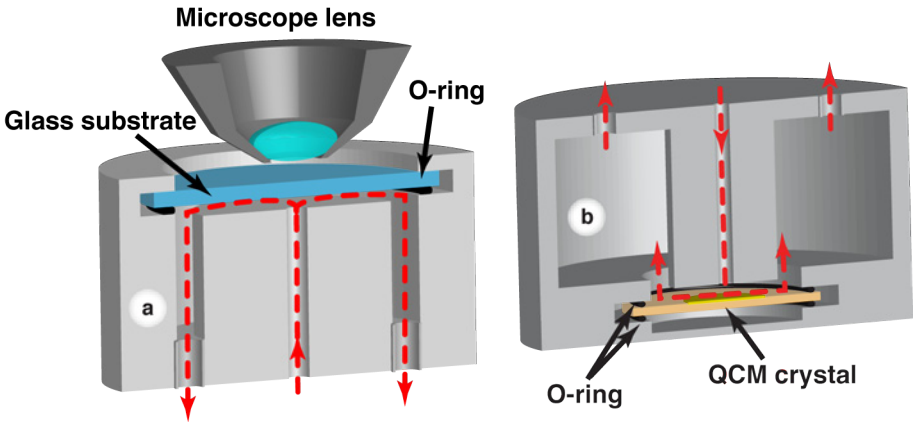

Figure 2-4. Schematics of (a) microscopy flow cell and (b) QCM-flow cell.

Figure 2-4a shows the flow cell used for in–situ microscopy investigations. The cell was positioned on the microscope stage and the microscope was typically focused on the centre of the glass bottom surface aligned with the nozzle outlet.

Figure 2-4b shows the QCM-flow cell. The cell was developed to accommodate a QCM quartz crystal in the centre underneath the nozzle outlet such as to form a thin layer flow cell.

The cells were designed to have the same thin cell geometry, 1.5 mm thickness, in such a way to obtain the same deposition conditions on both systems employed. Mass transport in the cells was simulated using finite element

software, which showed a well-defined radial laminar flow along the substrates (see chapter 6) This is of paramount importance for experimental reproducibility.

2.5.3 Deposition Procedure

The microscopy cells were firstly filled with water and then the supersaturated solution was flowed at 2 ml min^{-1} for a preset time and images were recorded every 5 s (total of 200 images for 1000 s) using dark field microscopy to enhance the crystal shape. At the end of an experiment the cell was filled with air and the glass substrate was quickly taken off and rinsed with acetone and nitrogen blow dry. The glass substrates were cut in two pieces through the centre and used respectively for micro-Raman spectroscopy and FE-SEM imagining (after gold coating).

Brand new quartz crystals were cleaned using water, chloroform and acetone in this sequence before use, and then blown dry with nitrogen. Deposition experiments were performed following the same procedure used for in–situ microscopy, but the variation of resonant frequency of the crystal was recorded during the deposition and then converted to mass deposited on the crystal surface using Sauerbrey equation:

$$\Delta f = \frac{-2 f_0^2}{A\sqrt{\rho\mu}} \Delta m \qquad (18)$$

where Δf is the variation of frequency, Δm is the change in the mass deposited, f_0 is the resonant frequency of the crystal (~7.995 MHz), A the area of the gold disk coated onto the crystal (0.205 cm^2), μ_q the shear modulus of the quartz (2.947 x10^{11} g cm^2) and ρ_q the density of the quartz (2.648 g cm^3). The

cell was then emptied by flowing in air and the QCM probe was removed and used for FE-SEM imaging (after gold coating).

The solution delivery system was carefully rinsed with 120 ml water, 120 ml pH 3 HCl acidic solution and 120 ml water. The flow cells were kept in acidic solution for 30 min and thoroughly rinsed with water, before and after each experiment to ensure removal of $CaCO_3$ possibly deposited.

2.5.4 Technical Drawings

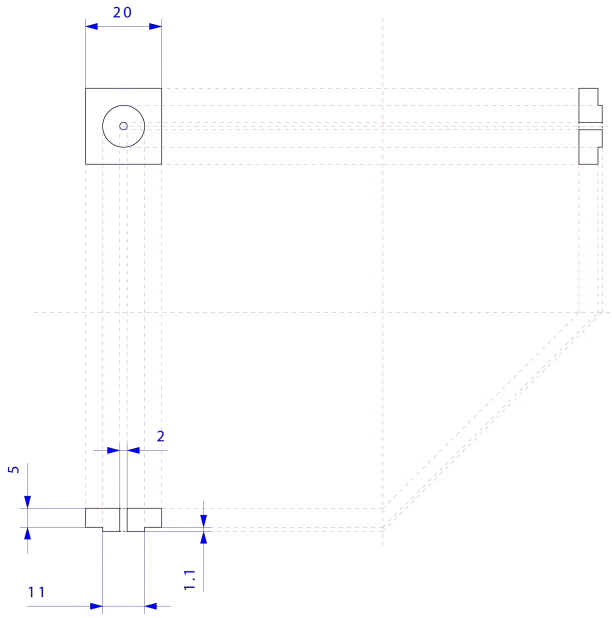

Figure 2-5. T-mixer lid, measures in mm.

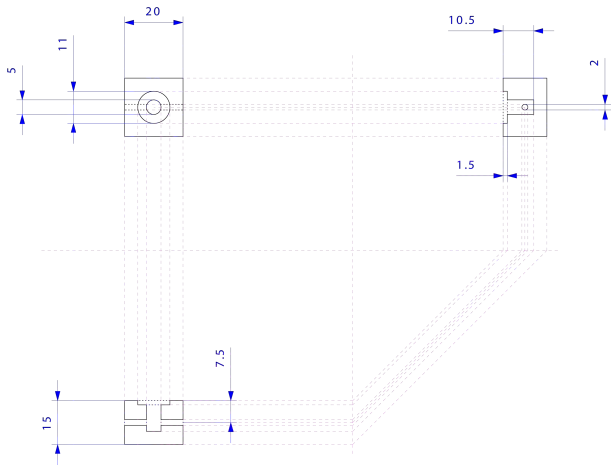

Figure 2-6. T-mixer body, measures in mm.

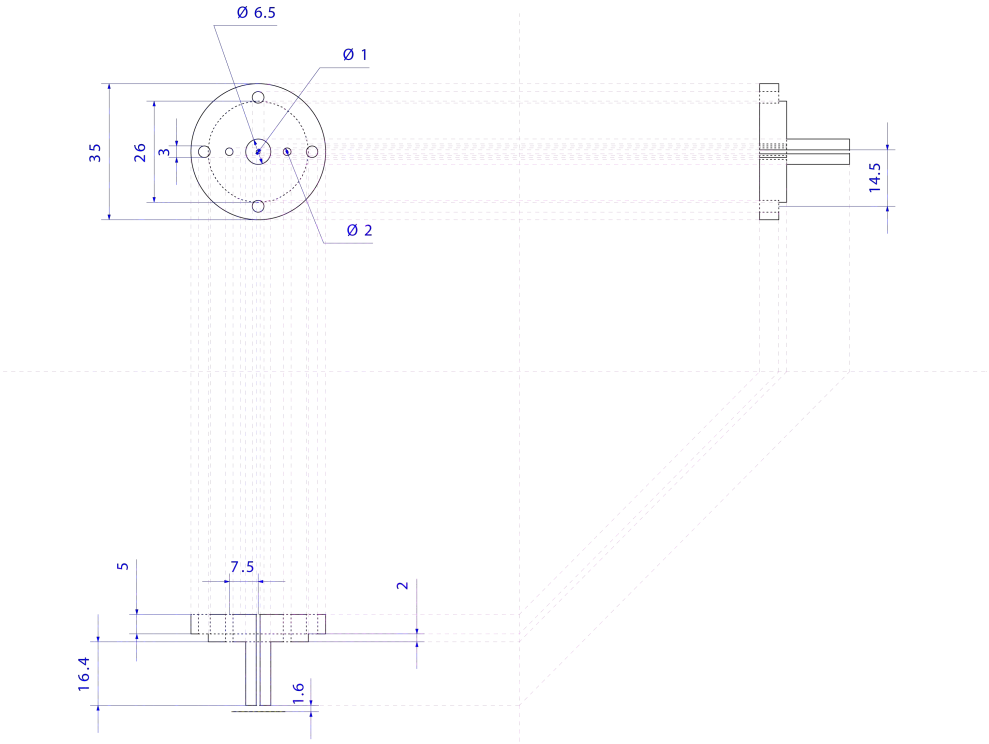

Figure 2-7. QCM-flow cell lid, measures in mm.

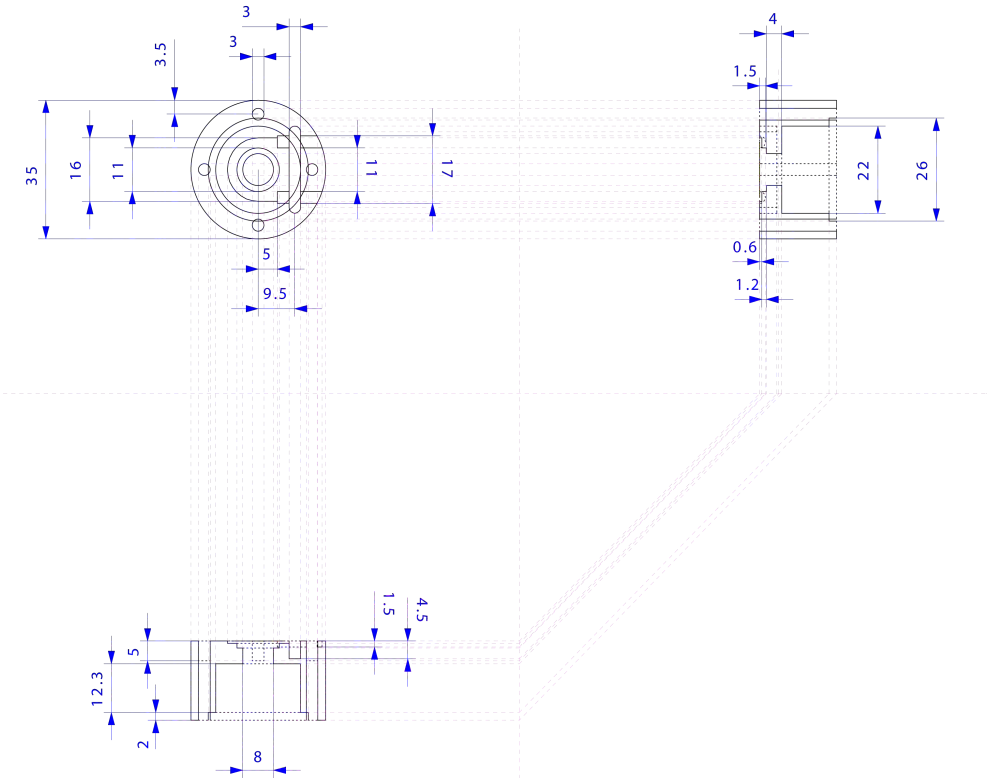

Figure 2-8. QCM-flow cell body, measures in mm.

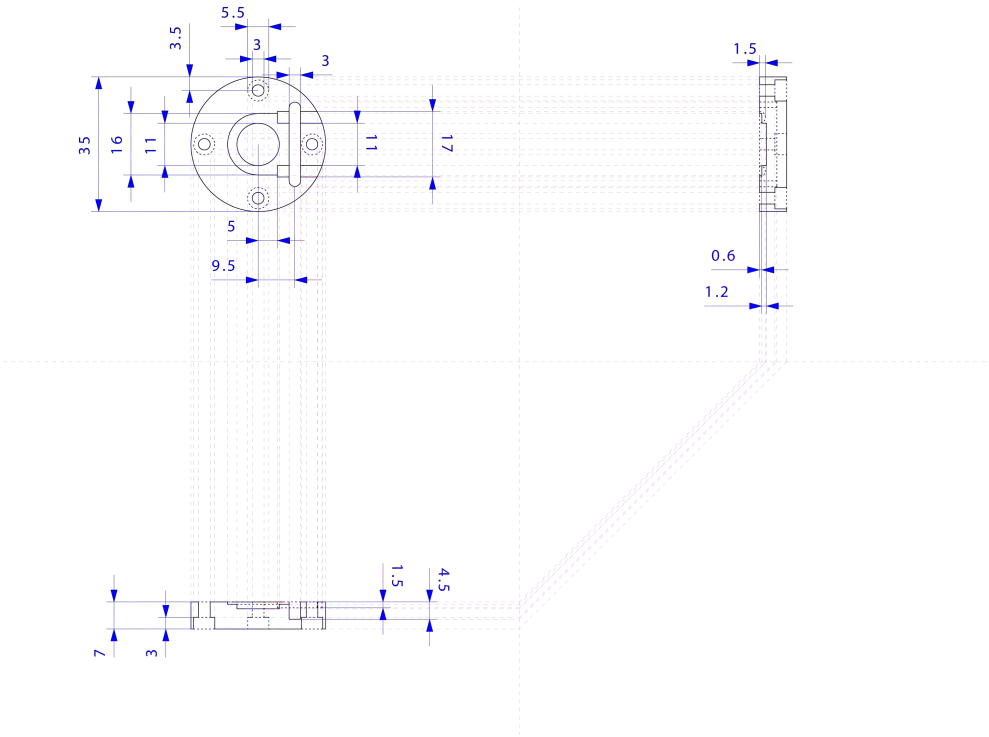

Figure 2-9. QCM-flow cell bottom, measures in mm.

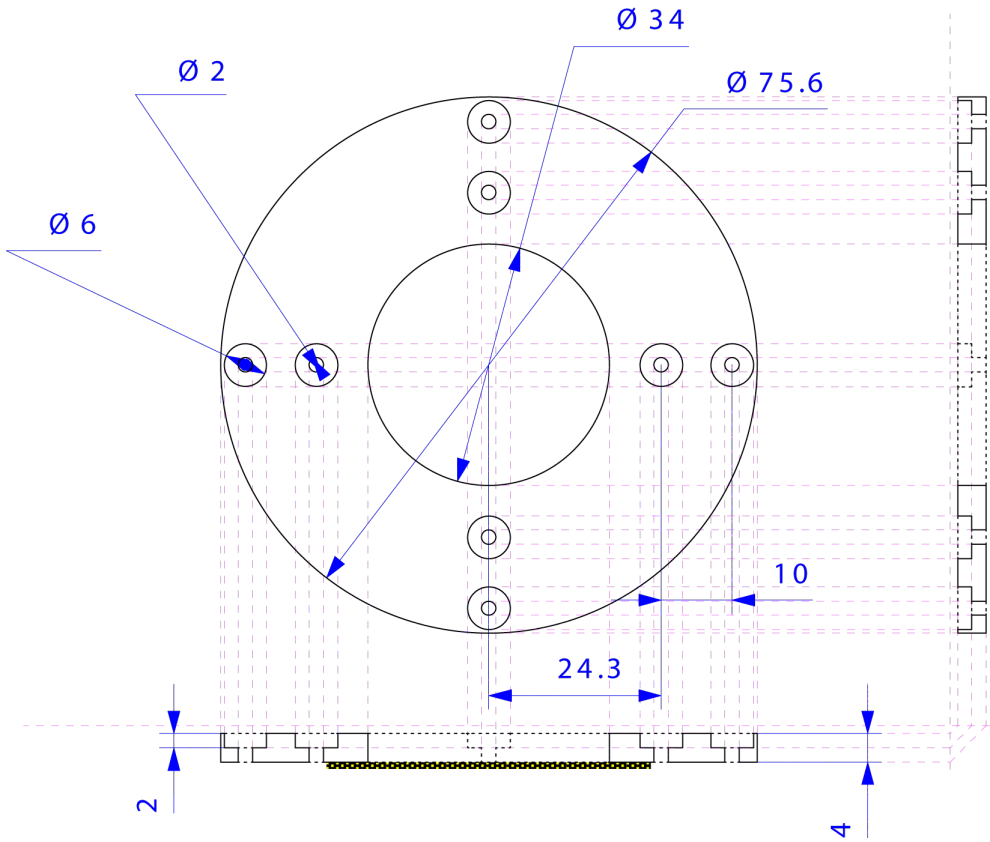

Figure 2-10. Microscope flow cell lid, measures in mm.

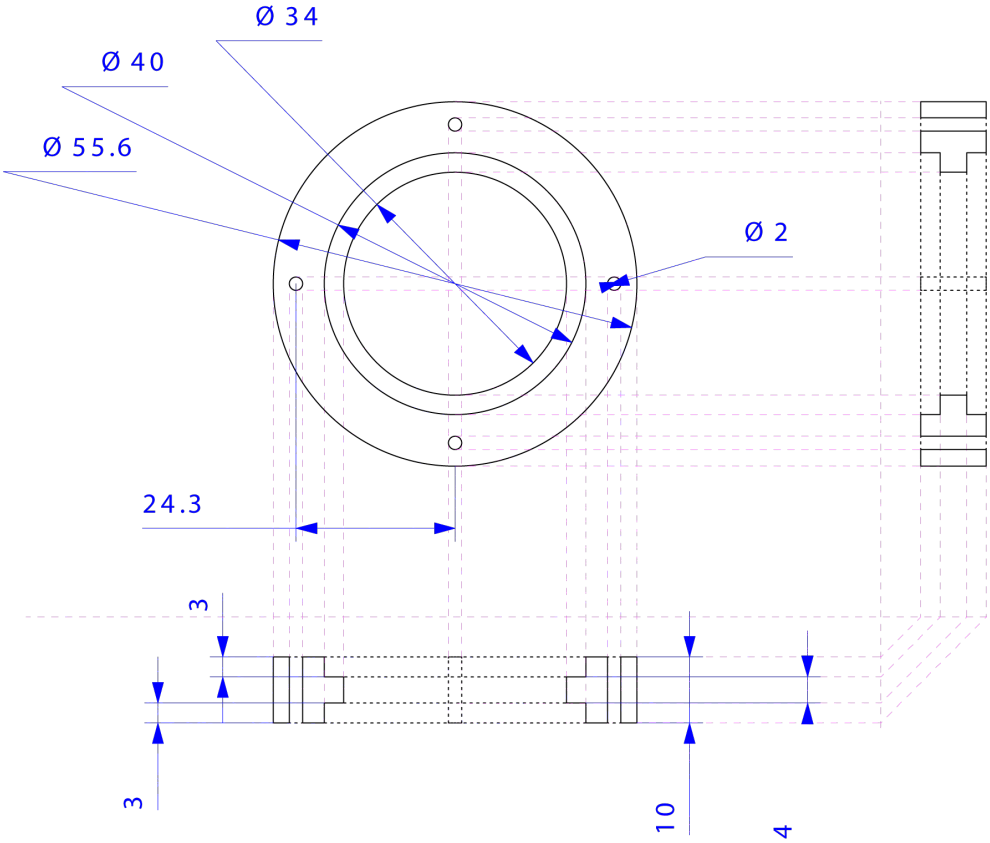

Figure 2-11. Microscope flow cell body, measures in mm.

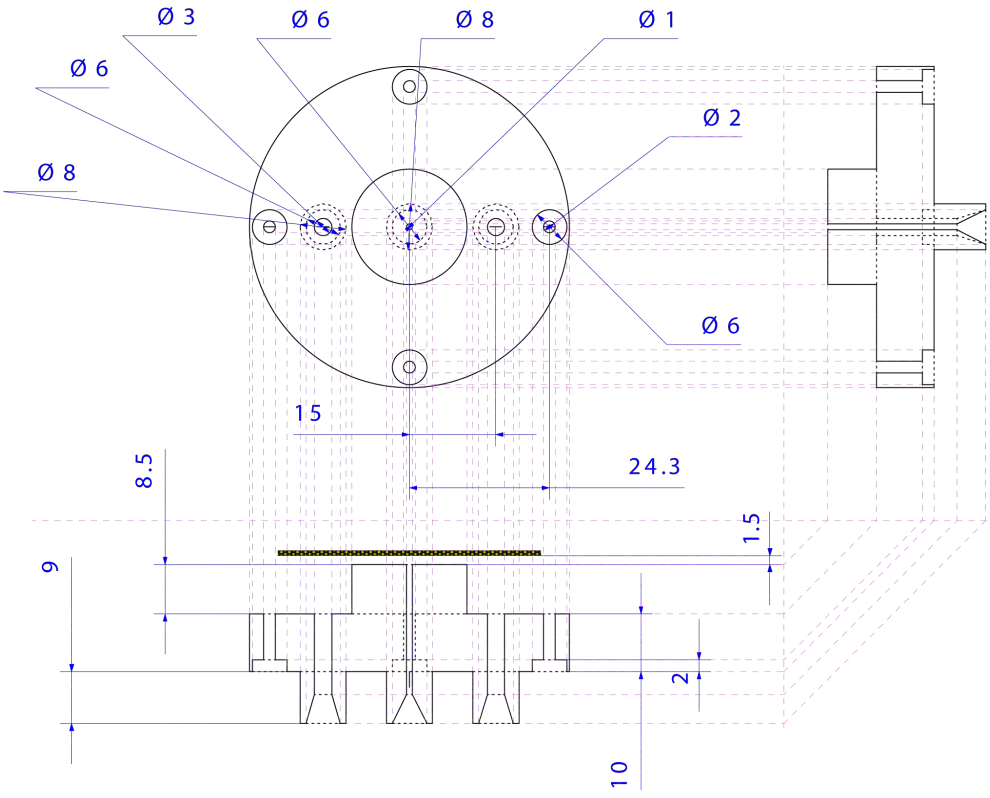

Figure 2-12. Microscope flow cell bottom, measures in mm.

2.5.5 Speciation Model

The system developed was built with the purpose of delivering a high-saturated solution of calcium carbonate. To use ion sensor devices to measure the ion concentrations after the mixer would have been problematic because such high-supersaturated solution can easily form incrustations at the sensor surface interfering with the reliability of the measurements. The determination of initial speciation after mixing was therefore calculated via speciation software (MINEQL+, version 4.6, environmental research software). The pH and concentrations of carbonate (chapter 6) and calcium and calcium/citrate (chapter 7) were chosen to obtain a constant saturation ratio (*S*) for all the solutions and to have CO_3^{2-} as the limiting species. Moreover, the concentration of calcium was chosen to be sufficiently high to avoid a complete depletion of Ca^{2+} activity in solution due to the chelant effect of citrate. A concentration of 10 mM for the carbonate ions solution, 20 mM for the calcium ions (with a concentration from 0 up to 7 mM of citrate ions) and pH 10.50 were the optimal to satisfy the previous stated conditions.

The simulations were performed fixing the temperature at 22 °C and the pH was calculated considering an electroneutral solution; the ionic strength was calculated by the software. The simulations considered a system closed to the atmosphere (no exchange of CO_2) and the influence of CO_2 dissolved in the water used to prepare the solutions was calculated considering a $pCO_2 = -3.5$ (normal atmospheric condition), the overall dissolved carbonate from CO_2 was calculated to be 0.11 μM, negligible for our purposes.

The pH of the solutions before pH correction, and the amount of NaOH to be added to each solution to obtain pH 10.50, was simulated. Good agreement

was found with the experimental data, confirming the validity of the speciation simulations (data reported in chapter 6 and 7).

Table 2-5. Solubility product constants [2].

Calcite K_{sp}	*ACC I* K_{sp}	*ACC II* K_{sp}
3.44×10^{-9} M^2	3.1×10^{-8} M^2	3.8×10^{-8} M^2

The speciation of the solution after mixing was based on the output data of the simulations carried out for the solutions before mixing. The initial saturation ratio (S) (19) after mixing was calculated, using the solubility product constants listed in Table 2-5 and the activity coefficient calculated via the Davies equation (20)

$$S = \sqrt{\frac{\left\{Ca^{2+}\right\}\left\{CO_3^{2-}\right\}}{\mathrm{K_{sp}}}} \tag{19}$$

$$\log \gamma_j = -Az_j^2\left(\frac{\sqrt{I}}{1+\sqrt{I}} - bI\right) \tag{20}$$

$$A = 1.82x10^6\left(\varepsilon T\right)^{-3/2} \tag{21}$$

$$\varepsilon = 87.74 - 0.400T_C + 9.398x10^{-4}T_C^2 - 1.141x10^{-6}T_C^3 \tag{22}$$

where γ_j is the activity coefficient for the component j, z_j the charge for the component j, b is a constant fixed with good approximation to 0.24, I the ionic strength (mol l^{-1}), T is temperature in Kelvin; ε is the dielectric constant, corrected for temperature using an empirical equation, (22), T_C is the temperature in Celsius. The activity of neutral ion pairs can be approximated to the concentration, since the activity coefficient at low ionic strength is ~1 (23).

$$\log \gamma_0 = bI \qquad (23)$$

where b is in the range of 0.1 – 0.2

In Table 2-6 are listed the activities after mixing of the relevant species for all the solutions prepared in chapter 6 and 7.

Table 2-6. Speciations of the solution after mixing.

Specie	*Concentration / M*	*Specie*	*Concentration / M*
$NaHCO_3$	5	$NaHCO_3$	5
$CaCl_2$	10	$CaCl_2$	10
$NaH_2Citrate$	0	$NaH_2Citrate$	0.5
Free ions	*Activity / M*	*Free ions*	*Activity / M*
H^+	1.02×10^{-11}	H^+	7.49×10^{-11}
Ca^{2+}	3.74×10^{-03}	Ca^{2+}	3.44×10^{-03}
Cl^-	1.69×10^{-02}	Cl^-	1.69×10^{-02}
CO_3^{2-}	4.73×10^{-04}	CO_3^{2-}	5.31×10^{-04}
Na^+	7.30×10^{-03}	Na^+	8.79×10^{-03}
$Citrate^{3-}$		$Citrate^{3-}$	1.58×10^{-06}
COMPLEXES		COMPLEXES	
OH^-	7.85×10^{-05}	OH^-	1.07×10^{-04}
$CaOH^+$	5.64×10^{-06}	$CaOH^+$	7.09×10^{-06}
$CaHCO_3^+$	6.99×10^{-05}	$CaHCO_3^+$	5.31×10^{-05}
H_2CO_3	2.6×10^{-07}	H_2CO_3	1.58×10^{-07}
HCO^{3-}	1.09×10^{-03}	HCO^{3-}	9.05×10^{-04}
$NaHCO_3$	4.74×10^{-06}	$NaHCO_3$	4.71×10^{-06}
NaH[Citrate]		NaH[Citrate]	2.97×10^{-12}
H_2[Citrate]		H_2[Citrate]	1.27×10^{-15}
H[Citrate]		H[Citrate]	2.91×10^{-10}
H_3[Citrate]		H_3[Citrate]	1.29×10^{-22}
$CaCO_3$	2.61×10^{-03}	$CaCO_3$	2.71×10^{-03}
Ca[Citrate]		Ca[Citrate]	4.17×10^{-04}
$NaCO^{3-}$	6.98×10^{-05}	$NaCO^{3-}$	9.47×10^{-05}
Na_2[Citrate]		Na_2[Citrate]	3.93×10^{-09}
Na[Citrate]		Na[Citrate]	1.51×10^{-07}
Ionic strenght	3.15×10^{-2}	Ionic strenght	3.17×10^{-2}
S^{ACCI}	7.6	S^{ACCI}	7.7
S^{ACCII}	6.8	S^{ACCII}	6.9
$S^{calcite}$	22.7	$S^{calcite}$	23.1
pH	9.99	pH	10.13

Specie	*Concentration / M*	*Specie*	*Concentration / M*
$NaHCO_3$	5	$NaHCO_3$	5
$CaCl_2$	10	$CaCl_2$	10
$NaH_2Citrate$	1	$NaH_2Citrate$	1.75
Free ions	*Activity / M*	*Free ions*	*Activity / M*
H^+	4.17×10^{-11}	H^+	2.35×10^{-11}
Ca^{2+}	3.11×10^{-03}	Ca^{2+}	2.71×10^{-03}
Cl^-	1.69×10^{-02}	Cl^-	1.69×10^{-02}
CO_3^{2-}	6.27×10^{-04}	CO_3^{2-}	7.20×10^{-04}
Na^+	1.04×10^{-02}	Na^+	1.27×10^{-02}
$Citrate^{3-}$	3.49×10^{-06}	$Citrate^{3-}$	6.99×10^{-06}
COMPLEXES		COMPLEXES	
OH^-	1.92×10^{-04}	OH^-	3.42×10^{-04}
$CaOH^+$	1.15×10^{-05}	$CaOH^+$	1.79×10^{-05}
$CaHCO_3^+$	3.14×10^{-05}	$CaHCO_3^+$	1.77×10^{-05}
H_2CO_3	5.76×10^{-08}	H_2CO_3	2.09×10^{-08}
HCO^{3-}	5.92×10^{-04}	HCO^{3-}	3.81×10^{-04}
$NaHCO_3$	3.67×10^{-06}	$NaHCO_3$	2.87×10^{-06}
NaH[Citrate]	4.35×10^{-12}	NaH[Citrate]	5.90×10^{-12}
H_2[Citrate]	8.70×10^{-16}	H_2[Citrate]	5.47×10^{-16}
H[Citrate]	3.59×10^{-10}	H[Citrate]	4.01×10^{-10}
H_3[Citrate]	4.96×10^{-23}	H_3[Citrate]	1.75×10^{-23}
$CaCO_3$	2.88×10^{-03}	$CaCO_3$	2.89×10^{-03}
Ca[Citrate]	8.31×10^{-04}	Ca[Citrate]	1.45×10^{-03}
$NaCO^{3-}$	1.32×10^{-04}	$NaCO^{3-}$	1.84×10^{-04}
Na_2[Citrate]	1.23×10^{-08}	Na_2[Citrate]	3.59×10^{-08}
Na[Citrate]	3.95×10^{-07}	Na[Citrate]	9.53×10^{-07}
Ionic strenght	3.19×10^{-2}	Ionic strenght	3.26×10^{-2}
S^{ACCI}	7.9	S^{ACCI}	7.9
S^{ACCII}	7.2	S^{ACCII}	7.2
$S^{calcite}$	23.8	$S^{calcite}$	23.8
pH	10.38	pH	10.63

Specie	*Concentration / M*	*Specie*	*Concentration / M*
$NaHCO_3$	5	$NaHCO_3$	5
$CaCl_2$	10	$CaCl_2$	10
$NaH_2Citrate$	2.5	$NaH_2Citrate$	3.5
Free ions	*Activity / M*	*Free ions*	*Activity / M*
H^+	8.33×10^{-12}	H^+	4.68×10^{-12}
Ca^{2+}	2.33×10^{-03}	Ca^{2+}	1.93×10^{-03}
Cl^-	1.68×10^{-02}	Cl^-	1.68×10^{-02}
CO_3^{2-}	8.27×10^{-04}	CO_3^{2-}	9.19×10^{-04}
Na^+	1.53×10^{-02}	Na^+	1.85×10^{-02}
$Citrate^{3-}$	1.15×10^{-05}	$Citrate^{3-}$	1.93×10^{-05}
COMPLEXES		COMPLEXES	
OH^-	9.59×10^{-04}	OH^-	1.71×10^{-03}
$CaOH^+$	4.31×10^{-05}	$CaOH^+$	6.37×10^{-05}
$CaHCO_3^+$	6.22×10^{-06}	$CaHCO_3^+$	3.20×10^{-06}
H_2CO_3	3.03×10^{-09}	H_2CO_3	1.06×10^{-09}
HCO^{3-}	1.56×10^{-04}	HCO^{3-}	9.72×10^{-05}
$NaHCO_3$	1.42×10^{-06}	$NaHCO_3$	1.07×10^{-06}
NaH[Citrate]	4.20×10^{-12}	NaH[Citrate]	4.77×10^{-12}
H_2[Citrate]	1.14×10^{-16}	H_2[Citrate]	6.02×10^{-17}
H[Citrate]	2.35×10^{-10}	H[Citrate]	2.21×10^{-10}
H_3[Citrate]	1.30×10^{-24}	H_3[Citrate]	3.84×10^{-25}
$CaCO_3$	2.85×10^{-03}	$CaCO_3$	2.62×10^{-03}
Ca[Citrate]	2.05×10^{-03}	Ca[Citrate]	2.85×10^{-03}
$NaCO^{3-}$	2.56×10^{-04}	$NaCO^{3-}$	3.43×10^{-04}
Na_2[Citrate]	8.66×10^{-08}	Na_2[Citrate]	2.13×10^{-07}
Na[Citrate]	1.91×10^{-06}	Na[Citrate]	3.87×10^{-06}
Ionic strenght	3.40×10^{-2}	Ionic strenght	3.60×10^{-2}
S^{ACCI}	7.9	S^{ACCI}	7.6
S^{ACCII}	7.1	S^{ACCII}	6.9
$S^{calcite}$	23.7	$S^{calcite}$	22.7
pH	11.08	pH	11.33

To evaluate the robustness of the preparation method a series of simulations were carried out in which an error of ±50 µl of NaOH added was considered, the error on the final *S* was less than 5%.

2.6 Bibliography

[1] Solla-Gullón, J.; Rodriguez, P.; Herrero, E.; Aldaz, A.; Feliu, J. M.; *Phys. Chem. Chem. Phys.* **2008**, *10*, 1359-1373.

[2] Gebauer, D.; Völkel, A.; Cölfen, H.; *Science* **2008**, *322*, 1819-1822.

Chapter 3 ELECTRODE FUNCTIONALISATION VIA REDOX-ACTIVE SELF-ASSEMBLED MONOLAYERS

Three different metal complex thiols were used to functionalise a platinum electrode and the work reported focused on finding the optimum experimental conditions and procedure to obtain compact self-assembled monolayer (SAM) with good redox-activity. A notable achievement is that potential-assisted deposition has been developed and used to form a SAM of a ruthenium complex showing an improvement on the conventional deposition process.

3.1 Introduction

The functionalisation of surfaces with transition metal complexes is attractive for the development of sensors and molecular electronic devices [1, 2] based on the rich redox and photophysical properties of the complexes. Despite

the increased interest in the attachment of metal complexes to surfaces [3, 4], the properties of their monolayer formation relating to structure, kinetics and thermodynamics of adsorption are less well understood than their organic counterparts. It has recently been shown that a Ru(II) tris-bipyridine complex with two thiol attachment sites for surfaces formed stable monolayers [4]. We have been interested in developing surface active metal complexes with recognition sites in order to build supramolecular wires on surfaces based on cyclodextrin-guest recognition properties, in a similar manner as their solution assembly [5].

Supramolecular approaches allow the construction of several components in a defined configuration [6]. Multi-electron metal centres, with appropriate redox and photochemical properties, in a single supramolecular structure, provide a basis for the development of molecular energy conversion system, and wires. However, previous approaches in this area have mainly concentrated on the covalent construction of metal-based donor and acceptor units linked with organic bridges [7]. This involves multi-step reactions to link the building blocks, often resulting in poor yields and synthetic complexity.

Non-covalently assembled systems, in contrast, have the potential to allow control of the charge transfer processes by a simple choice of the assembled photo- and redox-active components. In this context, self-assembled systems between Ruthenium bipyridine centres (Figure 3-1) and various electron or energy acceptors, for example, have recently attracted attention [8, 9].

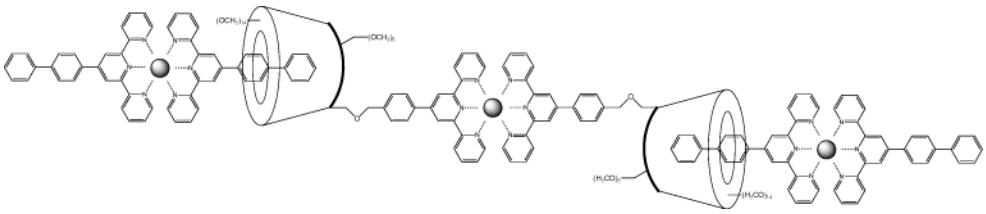

Figure 3-1. Non-covalent molecular wire.

The non-covalent assembly of molecular units in solution and at the interfaces is the key to providing functional molecular architectures. Cyclodextrin (CD) hosts are particularly promising for the aqueous assembly of guest molecules, due to their hydrophilic exterior and hydrophobic interior. A hydrophobic molecule in aqueous solution is driven into the cavity of the cyclodextrin for affinity with hydrophobic environment and to avoid the polar solvent (Figure 3-2). Aromatic groups are a good choice as guests for the assembly of conductive wires because they promote electron transfer (ET) along the wire.

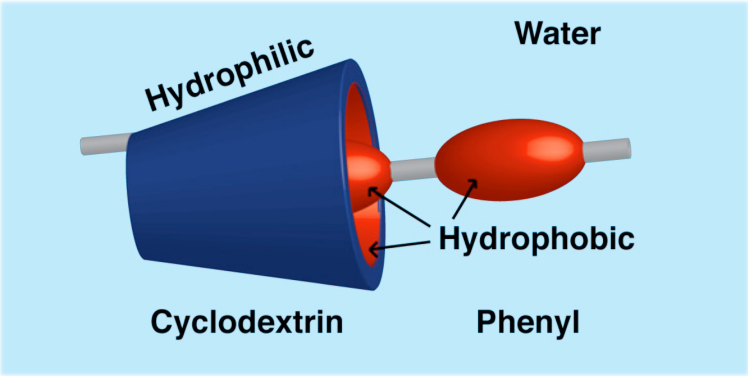

Figure 3-2. Cyclodextrin-Phenyl Host-Guest system.

Recently, both the aqueous assembly of photoactive metal units using a cyclodextrin host, and the communication of the metal centres by photo-induced process, has been demostrated [10].

The metal centres along the wire may be considered as Donor/Acceptor sites and the ET process is promoted by their reduction and oxidation (Figure

3-1). The processes involved in the passage of an electron through the metal centres may follow a hoping or tunnelling process, as already discussed in chapter 1. It depends on the structure of the molecules and types of bonds that connect the metal centres, the presence of conjugate chain or aromatic groups would promote a transfer through the hopping process. Covalently bonded wires and the presence of such kinds of bonds generally leads to a hopping process, but in the case of system with non-covalent bonds there is a break in the conjugate chain and a tunnelling process could be more favourable.

In this chapter, the monolayer formation of metal complexes with hydrophobic tails is investigated. The combination of a terpyridine moiety provides advantages in contrast to bipyridine metal complexes, due to the lack of geometrical isomers and the possibility for directional growth of the wire; and a thiol functionality seems especially appealing for the construction of metallo-supramolecular structures on metal surfaces.

3.1.1 Experimental

3.1.1.1 Materials

The metal complexes investigated in this chapter were synthesised at University of Birmingham by Dr. Evangelos Kefalas, part of the group headed by Dr. Zoe Pikramenou.

Table 3-1. Metal complexes investigated.

$[(biph\text{-}tpy)Os(tpy\text{-}SAc)](NO_3)_2$	
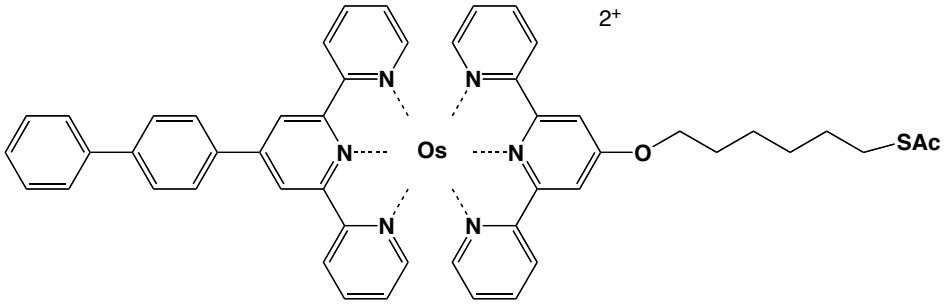	
Soluble in	FW
CH_3CN, CH_3CN/H_2O (50:50-90:10)	1106 g mol^{-1}
$[(CD\text{-}tpyOs(tpy\text{-}SAc)](PF_6)_2$	
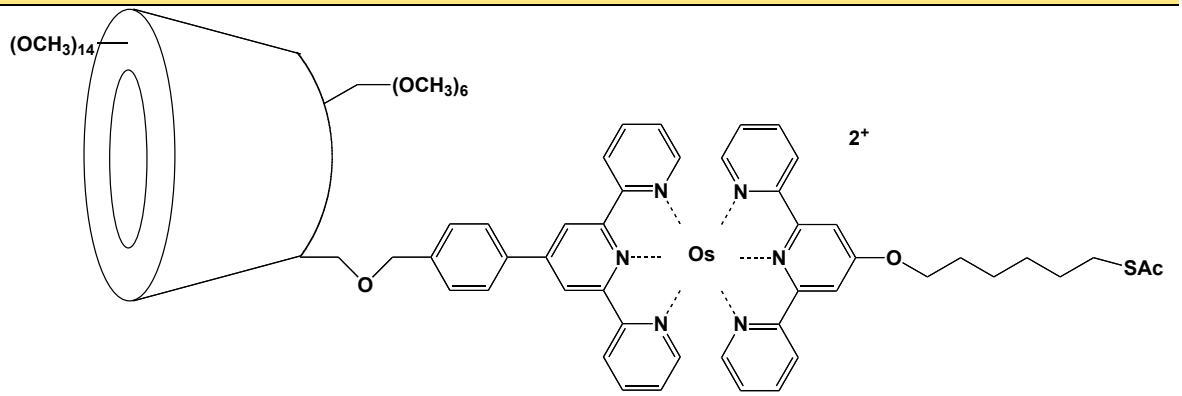	
Soluble in	FW
MeOH, CH_3CN/H_2O (90:10-60:40)	1569 g mol^{-1}
$[(biph\text{-}tpy)Ru(tpy\text{-}thioctic)](PF_6)_2$	
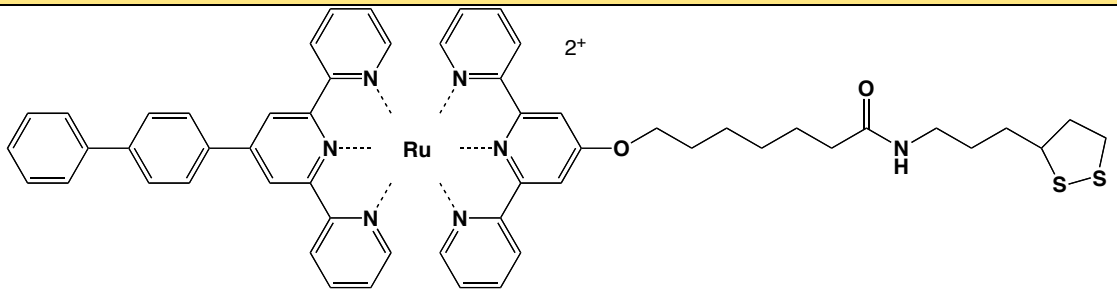	
Soluble in	FW
MeOH, CH_3CN	1298 g mol^{-1}

3.1.1.2 Droplet Setup

Electrochemical investigation of ruthenium complexes in water is difficult, since the oxidation potential of ruthenium (II/III) is more positive than for water oxidation on many electrode materials. Thus, an ionic liquid was employed for some studies because of the extended potential window offered. A droplet set up was employed (Figure 3-3) for electrochemical investigations of SAMs in the ionic liquid medium. A platinum macroelectrode (without or with a SAM previously deposited) was held in an inverted position and used as the substrate on which a droplet of ionic liquid was used as the electrolyte. A three electrode set up was employed as described in the previous paragraph using the inverted Pt macroelectrode as working electrode.

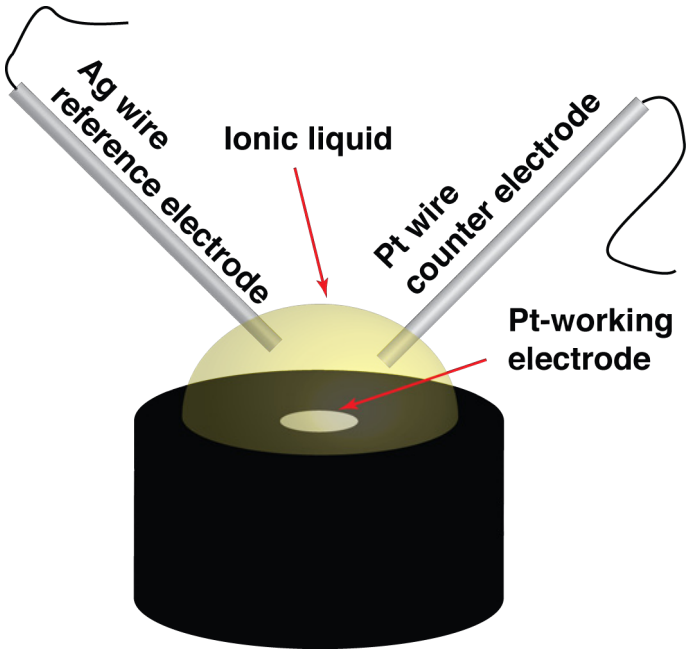

Figure 3-3. Droplet set up.

3.2 Results and Discussion

3.2.1 Self-Assembled Monolayer Assessment

The capability to form SAM; of each of the three different metal complexes was investigated initially in a systematic fashion. The formation of the SAMs was achieved by immersion of a clean platinum macroelectrode (1 mm radius) in a solution containing the metal complex of interest and tetra-butyl ammonium hesaflouro-phosphate ($tBAPF_6$) 0.1 M that was used as electrolyte for the electrochemical investigation. The depositions were carried out using different concentration of the target molecules ranging from 10 μM to 5 mM in three different solvents (MeOH, CH_3CN and CH_3CN:H_2O at different ratios) and different deposition times (few minutes to 3 days), to evaluate the surface coverage at thermodynamic equilibrium.

Attempts to increase the lateral interaction and improving the stability of the SAMs involved a series of further investigations adding to the deposition solution dodecane or undecane thiols in different percentages (1–10%). However, the presence of this type of thiol incorporation, which intrinsically form very stable pure monolayers, prevented the incorporation of the metal complexes on the electrode surface. In fact, all the electrochemical investigations carried out on functionalised electrodes using this technique did not show any surface redox process.

In Table 3-2 are listed the best experimental conditions for each complex, which gave the highest surface coverage. Figure 3-4 to 3-6 show typical CVs of

the final SAMs formed on the Pt macroelectrode, from which the surface area coverage could be calculated by integrating the current under the oxidation peak (after background subtraction) usually at scan rate of 10 V s^{-1} (see chapter 1).

Table 3-2. Molecules and deposition conditions for the formation of SAMs macro platinum electrode.

Compound	*Solvent*	*Conc./ mM*	*Deposition time / h*	Γ / *fmol* cm^{-2}
[(biph-tpy)Ru(tpy-thioctic)]$(PF_6)_2$	CH_3CN	0.5	20	42 ±2
[(biph-tpy)Os(tpy-SAc)]$(NO_3)_2$	CH_3CN	1	42	24 ±2
[(CD-tpy)Os(tpy-SAc)]$(PF_6)_2$	CH_3CN:H_2O / 90:10	2	42	<1

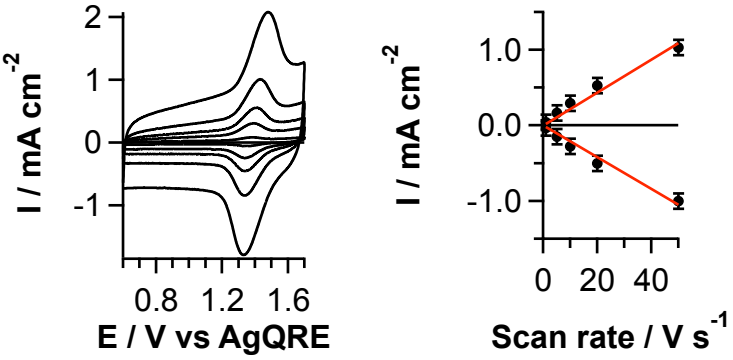

Figure 3-4. a) Cyclic-voltammograms at different scan rates (top to bottom 50, 20, 10, 5 and 1 V s^{-1}) of [(biph-tpy)Ru(tpy-thioctic)]$(PF_6)_2$, 0.5 mM, in CH_3CN and 0.1 M tBAPF6. b) shows the dependence of current peaks (after background subtraction) on scan rate.

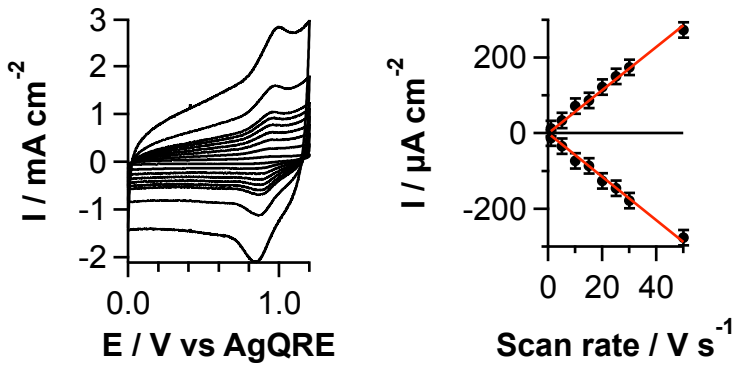

Figure 3-5. a) Cyclic-voltammograms at different scan rates (top to bottom 50, 30, 25, 20, 15, 10, 5 and 1 V s^{-1}) of [(biph-tpy)Os(tpy-SAc)]$(NO_3)_2$, 1 mM, in CH_3CN and 0.1 M tBAPF6. b) shows the dependence of current peaks (after background subtraction) on scan rate.

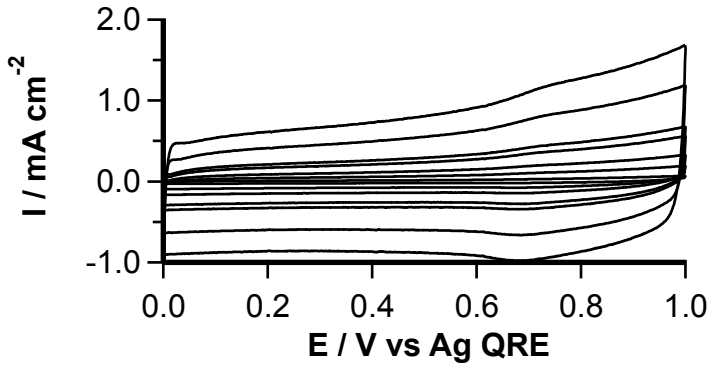

Figure 3-6. a) Cyclic-voltammograms at different scan rates (top to bottom 50, 25, 20, 10, 5 and 1 V s^{-1}) of [(CD-tpy)Os(tpy-SAc)]$(PF_6)_3$, 2 mM, in $CH_3CN:H_2O$ / 90:10 and 0.1 M tBAPF6.

The Ru and Os complexes showed a good linearity of the current peak with scan rate confirming a surface confined reaction [1].

The investigation using [(CD-tpy)Os(tpy-SAc)]$(PF_6)_2$ showed a really poor surface coverage, close to the detection limit (2 x10^{-13} mol cm^{-2}), in all the conditions used; probably the presence of such a bulky tail group (cyclodextrin) induces a high steric hindrance, decreasing the lateral interaction between neighbouring molecules. No further investigations were carried out with this

compound. The Ru^{II} complex with the thioctic ligand showed a higher surface coverage compared with the Os^{II} complex, because the presence of 2 sulphur groups seemed to facilitate a stronger binding on the substrate electrode.

3.3 Metal Complexes: Characterization in Solution

The Ru and Os complexes that gave reasonable SAM formation were investigated in solution in different solvents to evaluate the electrochemical reversibility [11] and calculate the diffusion coefficient. The reversibility was evaluated using a three electrode setup using a macroelectrode as working electrode (1 mm diameter disc). For a reversible redox system the peak to peak separation (oxidation and reduction peaks) is independent of the scan rate and is 59/n mV (n is the number of electrons exchanged, 1) at 298 K [11].

The diffusion coefficient was measured with a Pt UME (25 μm diameter) employing a 2 electrode setup. The faradaic current produced by the redox reaction at a micro disk electrode at steady state condition is described by eq (24) [11] from which it is possible to calculate the diffusion coefficient of the redox species.

$$j_{ss} = \frac{4nFDC^*}{\pi\ a} \qquad (24)$$

were j_{ss} (A cm^{-2}) is the steady-state current density, F (96.485 C mol^{-1}) is Faraday's constant, D (cm^2 s^{-1}) is the diffusion coefficient of the redox active specie and C^* (mol cm^{-3}) is its bulk concentration; a (cm) is the UME radius.

3.3.1 Osmium Metal Complex

3.3.1.1 Reversibility

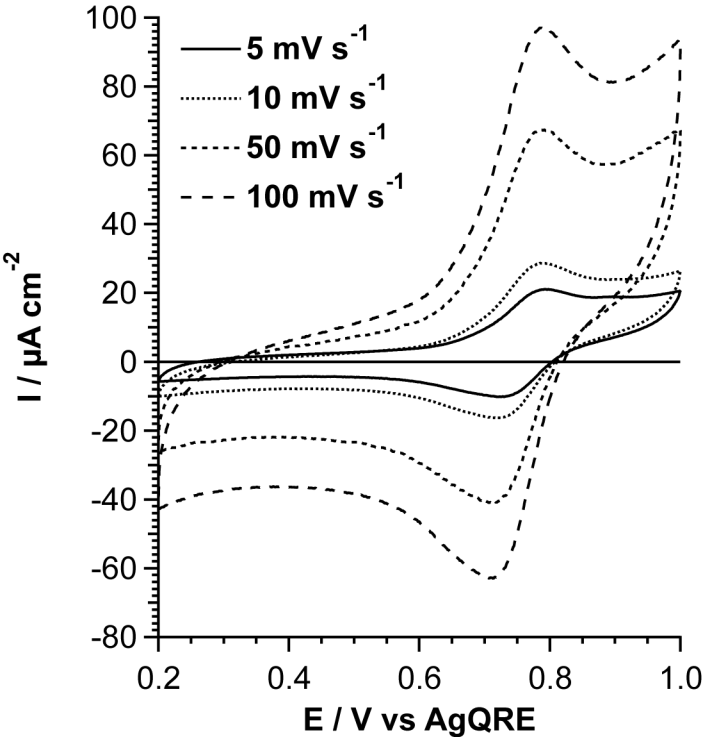

Figure 3-7. Cyclic-voltammograms at different scan rates of [(biph-tpy)Os(tpy-SAc)]$(NO_3)_2$], 0.5 mM, in MeCN (90%v/v) H_2O (10%v/v) and 0.1 M $tBAPF_6$.

In Figure 3-7 are plotted the second scan of the recorded voltammograms for the osmium metal complex and in Table 3-3 are reported the peak separations at different scan rates.

Table 3-3. Peak separation of [(biph-tpy)Os(tpy-SAc)]$(NO_3)_2$] at different scan rate.

Scan rate / mV s^{-1}	*ΔE /V*
5	0.062 ±0.002
10	0.063 ±0.002
50	0.068 ±0.002
100	0.078 ±0.002

The reaction showed a small deviation from reversibility; the peak separation increased with the scan rate, but the extent of this was not significant.

3.3.1.2 Diffusion Coefficient Measurement

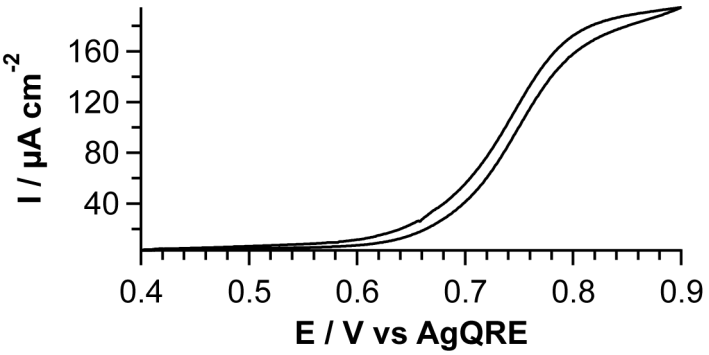

Figure 3-8. Cyclic-voltammogram at 5 mV s^{-1} of [O(biph-tpy)Os(tpy-SAc)]$(NO_3)_2$] 0.5 mM and 0.1 M $tBAPF_6$ in MeCN (90%$_{v/v}$) H_2O (10%$_{v/v}$).

Figure 3-8 shows the second scan of the recorded voltammograms at 5 mV s^{-1}. The current peak is 185 (±4) x10^{-6} A cm^{-2} and the half wave potential is 0.74 V. From the steady state current the diffusion coefficient of the specie in solution was calculated as 3.7 (±0.2) x10^{-6} cm^2 s^{-1}.

3.3.2 Ruthenium Metal Complex

3.3.2.1 Reversibility

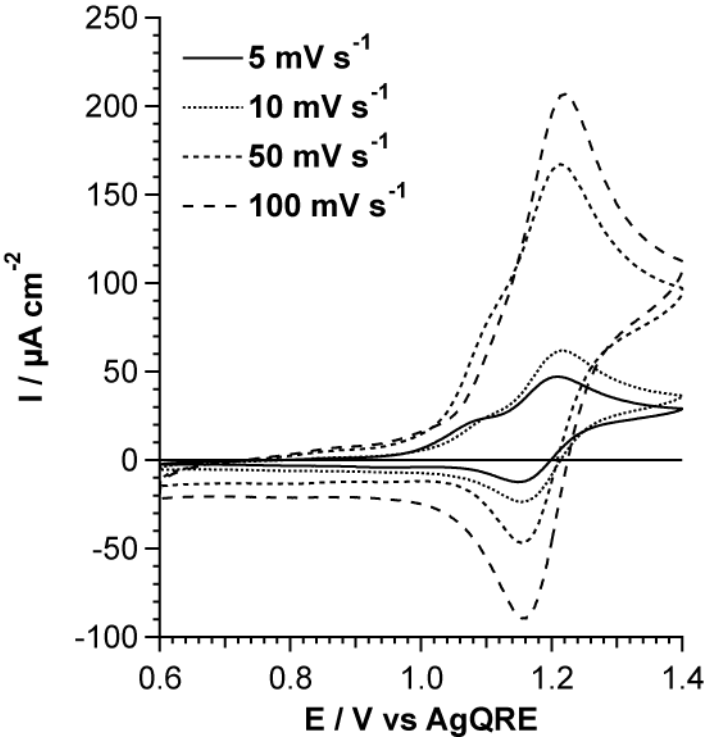

Figure 3-9. Cyclic-voltammograms at different scan rates of [(biph-tpy)Ru(tpy-thioctic)]$(PF_6)_2$, 1.3 mM, in MeCN and 0.1 M tBAPF6.

Figure 3-9 shows the second scan of the recorded voltammograms for the ruthenium metal complex and Table 3-4 reports the peak separation and current peak at different scan rates. Clearly visible in Figure 3-9 is a second peak at 1.07–1.10 V, that indicates the formation of a SAM of this compound. This is a clear indication of a better affinity of the di-thiols to bind to the Pt surface compared to the thiols present in the osmium complex. In this case the SAM is formed quickly.

Table 3-4. Peak separation of [(biph-tpy)Ru(tpy-thioctic)]$(PF_6)_2$ at different scan rates.

Scan rate / mV s^{-1}	*ΔE /V*
5	0.056 ±0.002
10	0.059 ±0.002
50	0.058 ±0.002
100	0.057 ±0.002

The redox reaction is reversible, since the peaks separation does not increase with scan rate and has value of ca. 59 ±2 mV.

3.3.2.2 Diffusion Coefficient Measurement

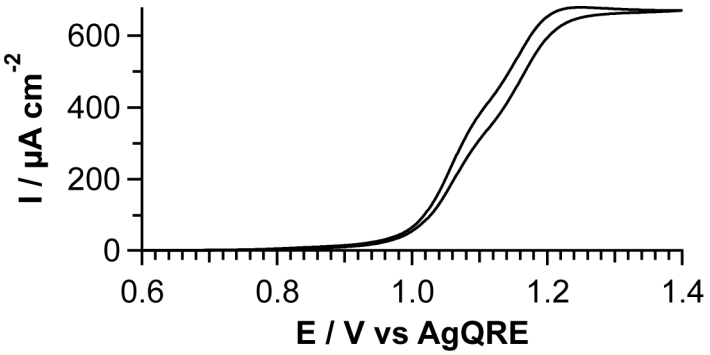

Figure 3-10. Cyclic-voltammogram at 5 mV s^{-1} of 1 mM [(biph-tpy)Ru(tpy-thioctic)]$(PF_6)_2$ and 2 M tBAPF6 in MeCN.

In Figure 3-10 is the second scan of the recorded voltammogram at 5 mV s^{-1} at the UME (25 µm diameter). The steady state current is 668 (±4) x10^{-6} A cm^{-2} and the redox potential is 1.11 V. From the steady state current the diffusion coefficient of the specie in solution was calculated as 3.4 (±0.2) x10^{-6} cm^2 s^{-1}. The presence of the second peak is also visible, attributed to surface-adsorbed material, as discussed above.

3.3.3 Potential Assisted Deposition

3.3.3.1 SAM Deposition Procedure

Two different strategies were performed to functionalise the electrode with [(biph-tpy)Ru(tpy-thioctic)]$(PF_6)_2$, which showed the most interesting characteristics to form a well-defined and compact SAM with a good electrochemical reversibility compared to the osmium complex. Immersion of the electrode in a solution of the molecule (either 0.5 mM or 1 mM) and 0.1 M $tBAPF_6$ was the first procedure followed. This procedure is the most commonly used to functionalise metal surfaces with self-assembled monolayers. In the second procedure, a sweep potential was applied for the time the electrode was immersed in the solution. The potential range was chosen to include the redox potential of the core metal of the complex. Electrochemical investigations of the functionalised electrode —to ascertain the amount adsorbed— were carried out by transferring the electrode to a freshly prepared solution of 0.1 M $tBAPF_6$ in acetonitrile. The ruthenium $2^+/3^+$ redox potential is higher than water oxidation and consequently acetonitrile, previously dehydrated and a sealed in a electrochemical cell, was employed to avoid water contamination.

3.3.3.2 Photophysical Properties of Solutions and Monolayers.

Acetonitrile solutions of [(biph-tpy)Ru(tpy-thioctic)]$(PF_6)_2$ display weak red luminescence from the ^{3}MLCT band, centred at 660 nm upon excitation at 480 nm (Figure 1). Monolayers of [(biph-tpy)Ru(tpy-thioctic)]$(PF_6)_2$ on Pt electrodes showed emission with maximum around 650 nm, despite the weak

luminescence signal. The blue shift in emission is also observed in powder samples of the complex (Figure 3-11). Powder samples of other biphenyl-terpyridine metal complexes showed similar blue shifts in the solid state [12], and in our case confirms that the signal observed is from the surface attached complex. The emission of monolayers of ruthenium bipyridine complexes attached to Au surfaces have been observed previously [4] and the results herein also confirm that the luminescence of the monolayers is not completely quenched by electron transfer from the excited state into the electrode.

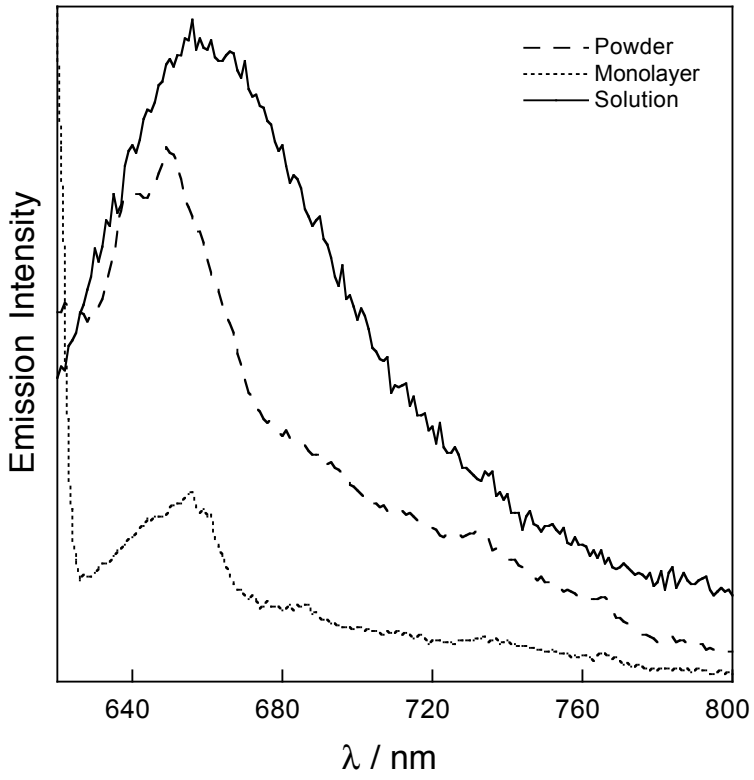

Figure 3-11. Luminescence spectra of [(biph-tpy)Ru(tpy-thioctic)]$(PF_6)_2$ acetonitrile solution, powder and monolayers on Pt, λ_{exc} =480 nm.

3.3.3.3 Electrochemical Characterisation of Self-assembled Monolayers

Figure 3-12 (○) shows the surface coverage as a function of time for the preparation of a functionalised electrode, from a solution 1.1 mM of [(biph-tpy)Ru(tpy-thioctic)]$(PF_6)_2$ and 0.1 $tBAPF_6$ without sweeping the potential at the electrode.

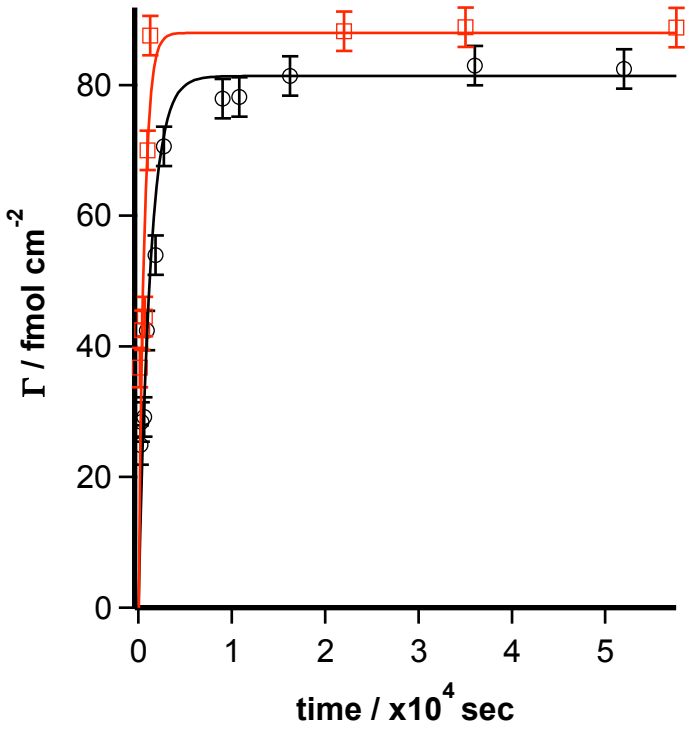

Figure 3-12. Time dependence of surface coverage of [(biph-tpy)Ru(tpy-thioctic)]$(PF_6)_2$ adsorbed on platinum microelectrode: (□) potential-assisted deposition (0.5 mM in CH_3CN (0.1 M $tBAPF_6$), (○) 1.2 mM in CH_3CN (0.1 $tBAPF_6$) conventional deposition. Solid line fits for kinetic Langmuir equation.

Fitting of adsorption kinetics was carried out with kinetic Langmuir equation [4] that assumed no interaction between neighbouring molecules.

$$\Gamma(t) = \Gamma_{sat}(1 - \exp(-k_{ads} C_b t)) \qquad (25)$$

where Γ is the surface coverage, k_{ads} the rate constant and C_b the bulk concentration, a rate constant of 0.67 ±0.07 M^{-1} s^{-1} was obtained.

Figure 3-12 (□) shows the surface coverage with time for the deposition of a Ru SAM employing a potential-assisted technique. A clean microelectrode was immersed in a solution 0.5 mM of the Ru complex in acetonitrile (0.1 M $tBAPF_6$) and the potential was swept from 0.5 V to 1.5 V vs AgQRE at 50 mV s^{-1}. A quicker formation of the SAM was obtained (with an estimated k_{ads} =3.3 ±0.4 M^{-1} s^{-1}) and similar surface coverage (88 ±2 fmol cm^{-2}) compared to the surface coverage obtained employing the previous conventional method (82 ±2 fmol cm^{-2}). The surface coverage obtained was much larger compared to the values reported in section 3.2.1, since more effective cleaning procedure was employed for UMEs. After each experiment the UME surface was polished via the procedure in chapter 2.

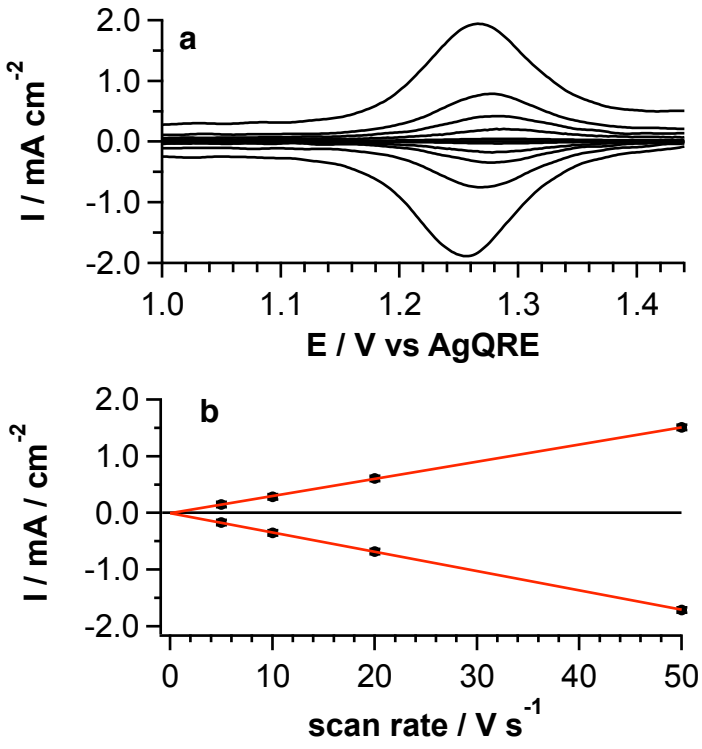

Figure 3-13. a) Cyclic voltammograms of [(biph-tpy)Ru(tpy-thioctic)]$(PF_6)_2$ self-assembled monolayer in acetonitrile (0.1 M $tBAPF_6$ electrolyte), prepared using the sweeping potential procedure. From top to

bottom 50, 20, 10, 5 and 1 V s^{-1}. b) shows the dependence of current peak on scan rate.

The SAM formed using the potential-assisted procedure showed excellent linearity between the current peaks and scan rate (Figure 3-13a ,b) confirming a surface confined reaction, ΔE_p ranged from 4 mV at 10 V s^{-1} to 16 mV at 50 V s^{-1}, showing a high electron transfer rate. The peak half-width (ΔE_{fwhm}) of the CV response, from which the data were derived, was in the range 98 ±5 mV (Figure 3-14) and was independent of the surface coverage. Slight deviation from the theoretical value of 90.6/n mV, independent of surface coverage, is attributed to a spread of the formal potential rather than interaction between molecules on the surface [2].

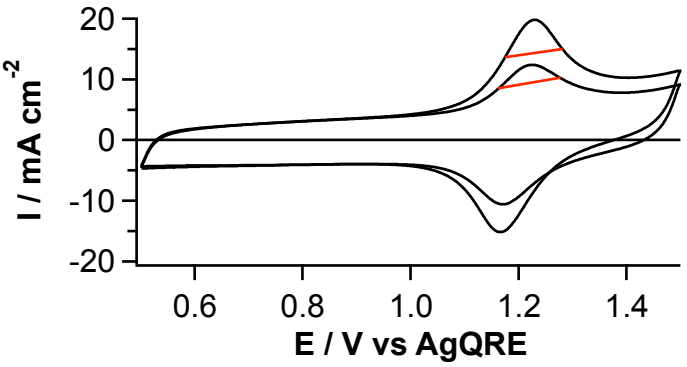

Figure 3-14. Cyclic voltammograms (200 V s^{-1}) of [(biph-tpy)Ru(tpy-thioctic)]$(PF_6)_2$ self-assembled monolayer in acetonitrile (0.1 M $tBAPF_6$ electrolyte), prepared using the sweeping potential procedure at different deposition time. Top 1240 s; bottom 680 s.

The main advantages of this procedure are removal of kinetically trapped and physisorbed molecules on the metal surface and the presence of molecules in both oxidation states in solution as well as in the SAM during the formation.

3.4 Characterisation of SAMs in Ionic Liquid Medium

Cyclic voltammograms of the SAMs were also measured using the droplet setup, in which the solution/electrolyte employed was BMI (ionic liquid). The SAMs were deposited without applying any potential, and the surface coverage (Table 3-5) was measured from the electrochemical investigation in ionic liquid medium following the above procedure (see chapter 1). The surface coverage of the SAMs was lower than the previous investigation reported in section 3.2.1.

Table 3-5. Deposition condition and surface coverage for different SAMs assembled at pt macro electrodes.

Compound	*Solvent*	*Conc./ mM*	*Deposition time / h*	Γ */ fmol cm*$^{-2}$
[(biph-tpy)Ru(tpy-thioctic)]$(PF_6)_2$	MeCN	3	20	59 ±2
[(biph-tpy)Os(tpy-SAc)]$(PF_6)_2$	MeCN	1	42	12 ±2

Further investigations at different scan rates were performed for the Ru complex (Figure 3-15 and Figure 3-16) showing linearity of current peaks with the scan rate, as expected for a surface-confined process.

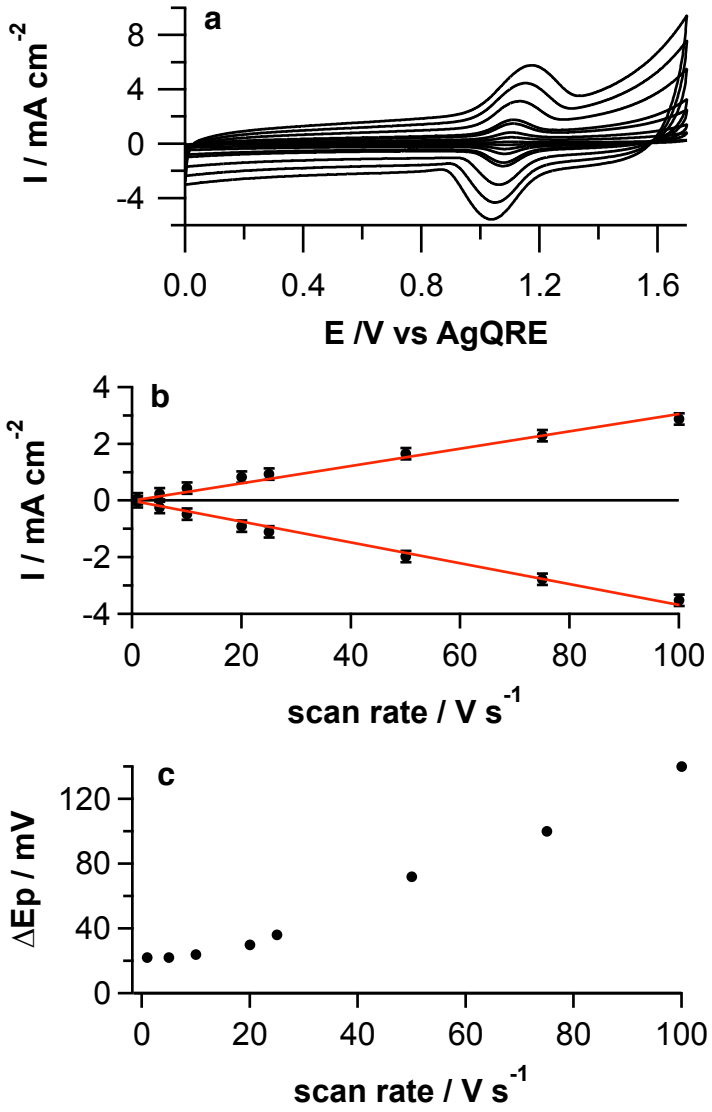

Figure 3-15 a) Cyclic voltammograms for an adsorbed monolayer of [(biph-tpy)Ru(tpy-thioctic)]$(PF_6)_2$ in BMI. Scan rates from 1 V s^{-1} to 100 V s^{-1}. b) Current peaks (anodic and cathodic) c) peak separation vs scan rate.

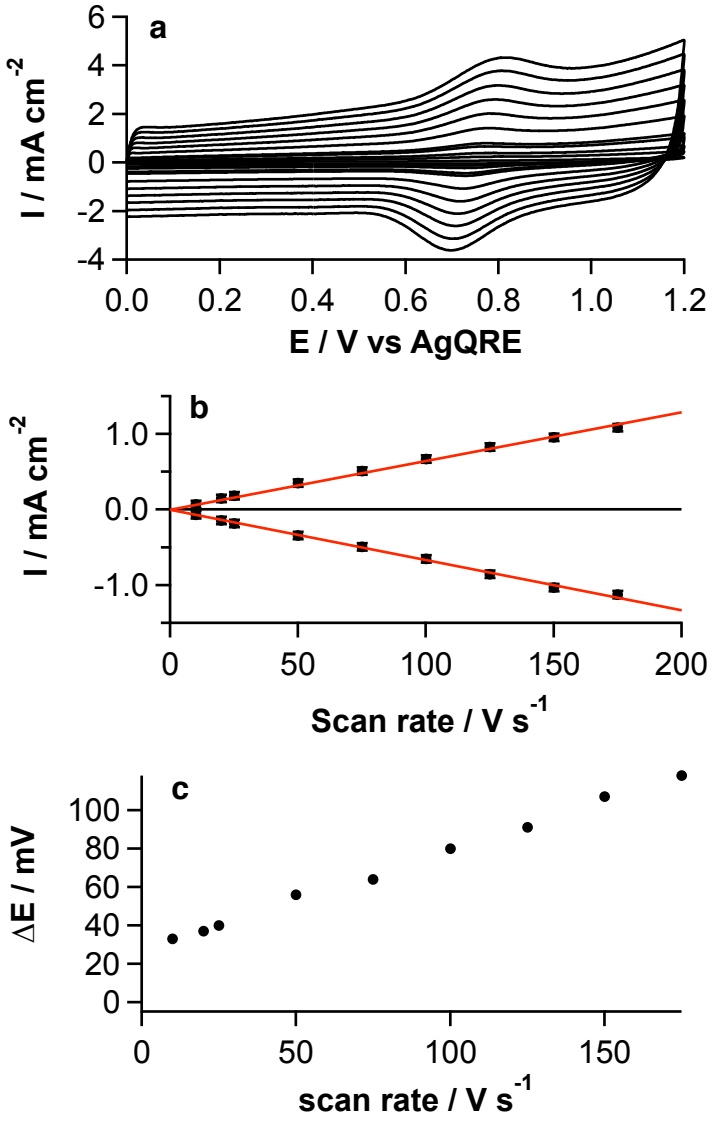

Figure 3-16 a) Cyclic voltammograms for an adsorbed monolayer of [(biph-tpy)Os(tpy-SAc)](PF$_6$)$_2$ in BMI. Scan rates from 1 V s^{-1} to 175 V s^{-1}. b) Current peaks (anodic and cathodic) c) peak separation vs scan rate.

The linear dependence of I vs scan rate confirms a surface confined process. The increasing peak separations with scan rate attaining 24 mV and 33 mV (at scan rate of 10 V s^{-1}) for Ru^{II} and Os^{II} complexes, respectively, indicates a quasi-reversible process that could be due to an interaction between the solvent and the SAM.

3.5 Conclusions

The Ru^{II} complex with the thioctic ligand results in strong adsorption on platinum electrodes and shows higher surface coverage compared with the Os^{II} complexes. The presence of 2 sulphur atoms in a tensioned 5 atoms cycle seems to facilitate the stronger formation of the SAM. The potential-assisted method resulted in a shortening of the deposition time. This procedure may be generally useful for the formation of SAMs. Based on the highest surface coverage, the Ru^{II} complex results to be the most interesting for quick formation of a monolayer and it is promising to be the first building block for tailoring the functional group with a second metal complex functionalised with a cyclodextrin.

3.6 Bibliography

[1] Steinberg, S.; Tor, Y.; Sabatani, E.; Rubinstein, I. *JACS* **1991**, *113*, 5176-5182

[2] Rojas, M. T.; Koeniger, R.; Stoddart, J. F.; Kaifer, A. E. *JACS* **1995**, *117*, 336-343

[3] Maskus, M.; Abruna, H. D. *Langmuir* **1996**, *12*, 4455-4462

[4] Bertoncello, P.; Kefalas, E. T.; Pikramenou, Z.; Unwin, P. R.; Forster, R. J. *J. Phys. Chem. B* **2006**, *110*, 10063-10069

[5] Faiz, J. A.; Williams, R. M.; Silva, M. J.; De Cola, L.; Pikramenou, Z. *JACS* **2006**, *128*, 4520-4521

[6] Barigelletti, F.; Flamigni, L. *Chem. Soc. Rev.* **2000**, *29*, 1-12

[7] Cardenas, D. J.; Collin, J. P.; Gavina, P.; Sauvage, J. P.; Cian, A. D.; Fischer, J.; Armaroli, N.; Flamigni, L.; Vicinelli, V.; Balzani, V. *JACS* **1999**, *121*, 5481-5488

[8] Ward, M. D. *Chem. Soc. Rev.* **1997**, *26*, 365-375

[9] Hu, Y. Z.; Tsukiji, S.; Shinkai, S.; Oishi, S.; Hamachi, I. *JACS* **2000**, *122*, 241-253

[10] Haider, J. M.; Chavarot, M.; Weidner, S.; Sadler, I.; Williams, R. M.; De Cola, L.; Pikramenou, Z. *Inorg. Chem.* **2001**, *40*, 3912-3921

[11] Bard, A. J.; Faulkner, L. R. *Electrochemical methods: fundamentals and applications* , 2nd ed.; John Wiley & Sons, Inc.: United States of America, 2001.

[12] Alcock, N. W.; Barker, P. R.; Haider, J. M.; Hannon, M. J.; Painting, C. L.; Pikramenou, Z.; Plummer, E. A.; Rissanen, K.; Saarenketo, P. *J. Chem. Soc., Dalton Trans.* **2000**, *2000*, 1447-1462.

Chapter 4 DECORATION OF CONDUCTIVE SUBSTRATE WITH ELECTROACTIVE METAL NANOPARTICLES A: PALLADIUM NANOPARTICLES ULTRA-THIN NAFION FILM

A simple method for producing electrochemically-active palladium nanoparticles within ultra-thin Nafion films via impregnation and chemical reduction is described. Atomic force microscopy studies showed the thickness is highly controlled for the preparation of Nafion film at the nanoscale range. Electrochemical investigation of this nano-composite material produced showed excellent electrochemical catalytic properties on hydrogen oxidation reaction. The methodology used for the preparation of this nano-composite material shows promise for applications in nano devices such as sensors or fuel cells.

4.1 Introduction

The synthesis of nanometer-sized particles is of tremendous interest in different fields of chemistry and allied disciplines [1-3]. However, the synthesis of naked metal nanoparticles remains challenging, with aggregation and sintering providing an obstacle in practical applications [4]. To overcome such problems, metal nanoparticles are often synthesized or immobilized on solid supports (zeolites, polymers) [5-11] or stabilized by capping with small organic ligands or polymers, in order to reduce agglomeration processes [12-15]. The dispersion of nanoparticles in polymer films is attractive, as it may enhance the processibility and allow a wider variety of surfaces and interfaces to be functionalised with nanoparticles.

Pd nanoparticles are attracting considerable interest for hydrogen-related applications, such as hydrogenation, hydrogen evolution and hydrogen oxidation [16]. Several strategies have recently emerged for the preparation of nanostructured Pd films, including template electrodeposition at solid/liquid and liquid/liquid interfaces [17-20]. This chapter report a simple strategy for fabricating relatively monodisperse palladium nanoparticles embedded in a Nafion ultra-thin polymeric film.

4.2 Experimental

A simple method for producing electrochemically-active palladium nanoparticles within ultra-thin Nafion films is described. The method takes advantage of the fact that Nafion films have a structure in which the hydrophilic sulfonated end groups aggregate in domains located within the hydrophobic

matrix, constituted by the fluorocarbon backbone [21]. The hydrophilic domains can be loaded with Pd(II) which, upon reduction, facilitates the formation of small particles in these nanocompartments.

4.2.1 Nafion Ultra-thin Film Deposition

Nafion (Figure 4-1) is a perfluorinated ionomeric cation exchanger, well known for its thermal, chemical and electrochemical stability [22]. As a membrane, Nafion is used extensively as an electrolyte in methanol and hydrogen fuel cells [23-25]. Traditionally, Nafion films have been rather thick (>1 μm), but recent developments have seen the use of the Langmuir-Schaefer (LS) technique [26], to produce Nafion films on solid supports at the nanometer and mesoporous scale. Such films have proved useful for incorporating different species such as metal oxides [27] and redox mediators [28-28].

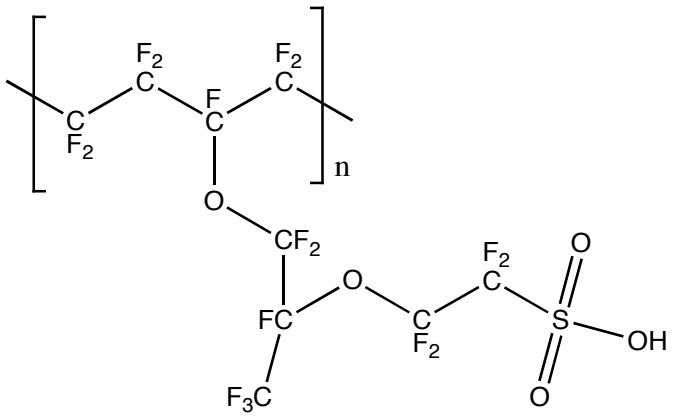

Figure 4-1. Nafion molecular structure.

The film was deposited using LS technique [26], on ITO, silicon passivated slide and microscopy slides. The glass slides were silanised to ensure a hydrophobic surface for better adhesion. The substrates were cleaned by sonication in isopropanol, acetone and chloroform for 5 minutes before use of the Nafion films. A commercial stock solution of Nafion was diluted with methanol

to obtain a final concentration of 0.85 mg mL^{-1}. The Langmuir monolayer was prepared employing Langmuir trough 540 cm^2 size (Figure 4-2) (Nima Technology, Coventry, England) by spreading 200 - 300 µl of the dilute solution over the water subphase. Because Nafion is slightly soluble in water, 0.1 M $NaNO_3$ was added to the subphase to reduce its solubility.

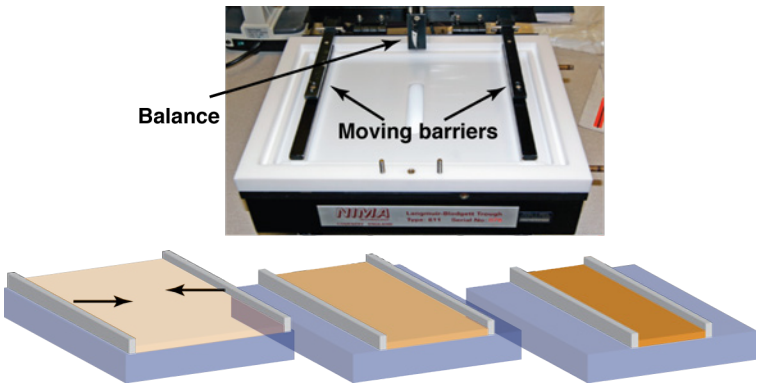

Figure 4-2. Langmuir trough.

A period of two minutes was allowed to elapse before compression of the floating films. The fabrication of the Nafion LS films were performed by holding a surface pressure of 20 mN m^{-1} (Wilhemy balance, ±0.1 mN m^{-1} accuracy). This surface pressure corresponds to the liquid phase of the Nafion layer as shown in Figure 4-3, which is a typical isotherm with the same experimental conditions used for the deposition.

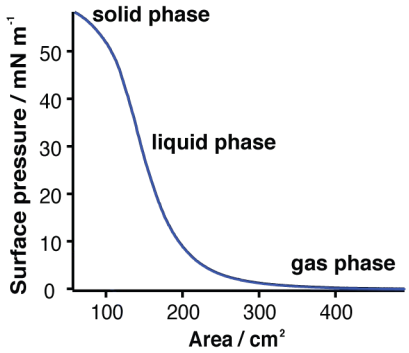

Figure 4-3. Isotherm of a Nafion monolayer on $NaNO_3$ 0.1 M water solution subphase.

Transferring the monolayer from the interface of the trough to the substrate was performed by approaching the substrate horizontally to the floating film and then moving it up (Figure 4-4). Any excess water on the substrate was removed by a nitrogen gas flux.

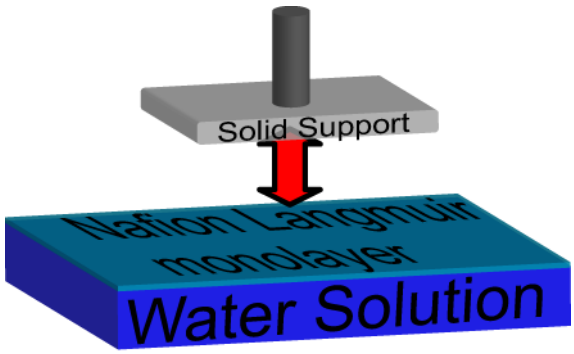

Figure 4-4. LS technique schematic.

Repeating this procedure enable the preparation of substrates with different film thickness, by means of different numbers of layers transferred.

The thickness of three samples prepared by deposition of 20 layers of Nafion on a silicon slide was measured using a scratch technique with an AFM. With the AFM (in contact mode) tip a portion of the film was removed and then by scanning across the step it was possible to measure the height of the film (Figure 4-5),

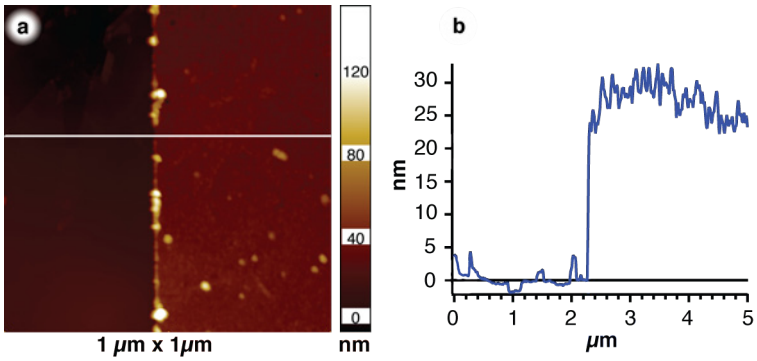

Figure 4-5. Thickness layer.

from the step height the average film thickness of a single layer deposited resulted in 1.5 ±0.2 nm.

4.2.2 Palladium Nanoparticles Incorporation

A schematic of the procedure used to incorporate Pd NPs is illustrated in Figure 4-6. The substrates after fabrication of Nafion LS films between 10 and 50 layers, corresponding to film thicknesses ranging from 15 to 75 nm, were dipped for 30 minutes in 4.8 mM $PdNO_3$ 17.7 mM HNO_3 solution, prepared by dilution of the commercial solution (see chapter 2) in water and addition of Nitric acid. This allowed the electrostatic incorporation of Pd(II) within the negatively charge of Nafion LS film. After removing the electrode from this loading solution and rinsing with water to remove the excess of solution, Pd(II) ions incorporated in the films were reduced to Pd(0) by dipping the substrate in freshly prepared 10 mM $NaBH_4$ in water for 2 minutes, which acted as reducing a agent. After each step, the samples were gently washed with water.

Figure 4-6. Schematic of the fabrication of palladium nanoparticles within a Nafion LS films.

4.2.3 Morphology Imaging

Transmission electron microscope (TEM) analysis were performed on 20 layers Nafion LS films deposited onto bespoke ion-beam thinned silicon substrates (3 mm diameter) prepared in–house, while for TM-AFM analysis, 300 nm oxidized silicon was used (IDB Technologies Ltd., UK) as the substrate for film deposition.

Typical TEM image (Figure 4-7) of Pd NPs incorporated within a 20 layer Nafion LS film shows clearly that Pd NPs are formed and that although there is some clustering, the particles are discrete. The diameter of Pd NPs measured by TEM was in the range 5 ±1 nm.

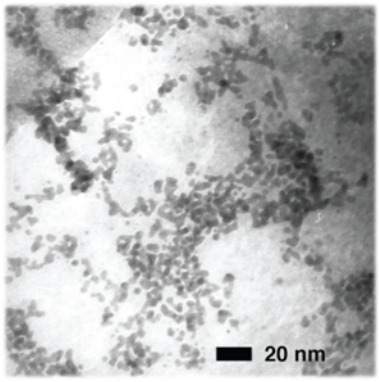

Figure 4-7. TEM image of palladium nanoparticles in a 20 layer Nafion LS film.

Figure 4-8 shows typical TM-AFM images of a 10 layer Nafion LS film before (a) and after (b) reduction of Pd(II) to Pd(0) by $NaBH_4$: a relatively smooth and uniform film is evident for the pristine Nafion film, while features with a characteristic size of 20 – 30 nm are visible after treatment with $NaBH_4$, which is reasonably consistent with the scale of the nanoparticle clustering observed by TEM.

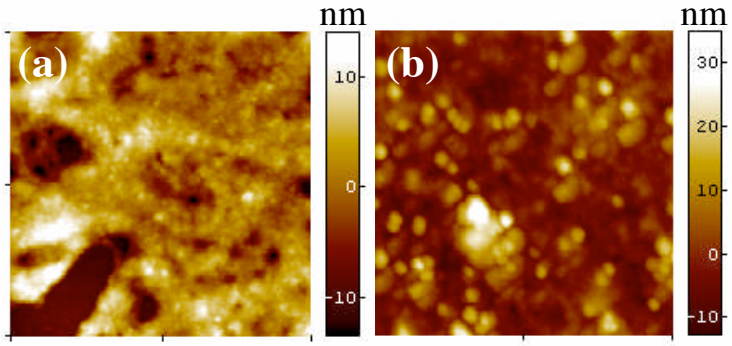

Figure 4-8. TM-AFM topography images of a 10 layer Nafion LS film before (a) and after (b) formation of Pd nanoparticles. The lateral scale of the images is 1 µm x 1 µm.

4.2.4 Electrochemical Setup

Electrochemical investigations were carried out using a three electrode setup, with the ITO-functionalised substrate as the working electrode (0.3 - 0.6 cm^2), a platinum wire as counter and a silver wire coated with silver chloride (Ag/AgCl) as reference electrode. A sealed cell (glass cell with a PTFE base and lid) (Figure 4-9) was employed for experiments in inert atmosphere (N_2) or saturated with hydrogen or nitrogen gas. The cell was provided with inlet and outlet tubing, making it possible to saturate the solution with nitrogen or hydrogen gas.

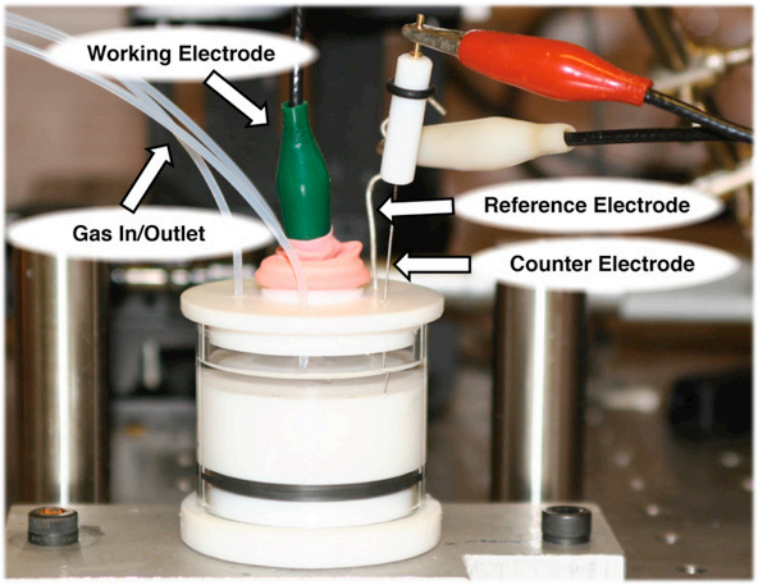

Figure 4-9. Sealed cell used for electrochemical measurements.

4.2.5 Scanning Electrochemical Microscopy (SECM) Setup

The SECM system was situated inside a built in–house Faraday cage and equipped with z-axis piezo electric positioner holding the working electrode, an ultra-microelectrode (UME). A sealed electrochemical cell (glass cell with a

PTFE base and lid) was used to avoid interference by oxygen and before every measurement nitrogen was bubbled inside the solution for 10 minutes. During the measurement the nitrogen tubes was moved away from the solution surface preserving a slight positive flux. A platinum wire was used as counter electrode and Ag/AgCl as reference electrode.

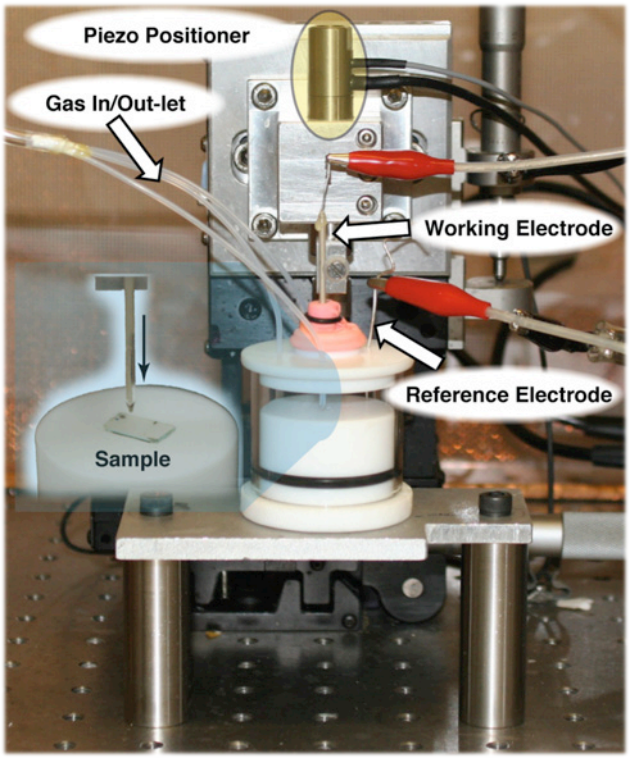

Figure 4-10. SECM setup.

The piezoelectric positioner (Jena, Germany) was connected to the piezo controller (NV 40/1 Cl, Piezo system, Jena, Germany). The working electrode was connected to a triangular wave generator and the reference electrode was connected to a current amplifier. The piezo controller and the potential generator were controlled by a PC.

A negative working window was needed (-0.9 V), and so a gold UME was electrochemically coated with mercury, to give a good cathodic window. The coating was performed in a solution of 0.5 M $HgNO_3$ and 1 % in HNO_3 on a

gold UME of 25 µm diameter with *Rg* 10 (*Rg* = *R*/*a*) (Figure 4-11). The electrochemical cell comprising the UME as working electrode and Ag/AgCl as reference electrode was degassed with nitrogen to eliminate the oxygen. The potential was set at -0.9 V for ~2 minutes to reduce the mercury and form a hemisphere of liquid mercury on the surface of the gold wire (Figure 4-11).

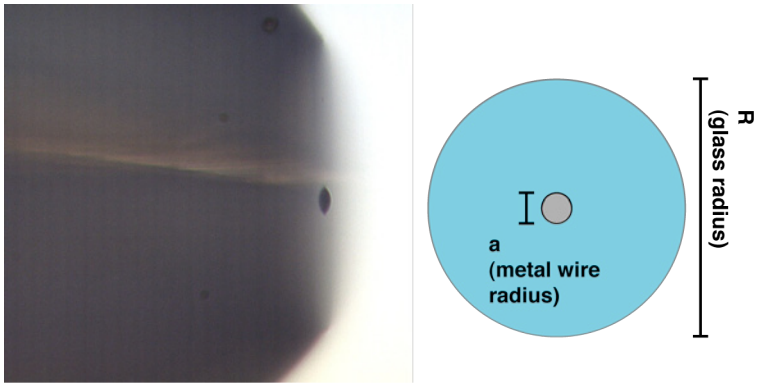

Figure 4-11. Au/Hg UME.

4.3 Results and Discussion

4.3.1 Nafion Film Thickness Effect

Cyclic voltammetry (CV) was used to investigate whether the Pd NPs incorporated within the Nafion LS film were in electrical contact with the underlying ITO electrode. Figure 4-12a reports typical CVs of a 10, 20, 30, 40 and 60 layers nanocomposite film in 0.1 M $NaNO_3$ at pH 3 (HNO_3).

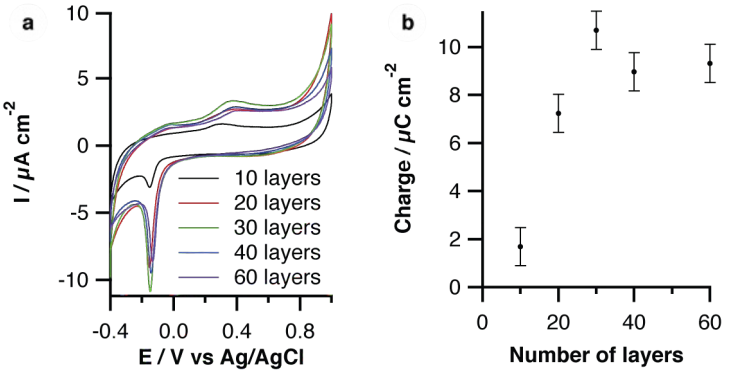

Figure 4-12. (a) CVs of a 10, 20, 30, 40, 60 layer Pd/Nafion LS film in 0.1 M KNO_3, pH 3 (HNO_3), scan rate 50 mV s^{-1}. (b) Pd oxide reduction charge vs numbers of Nafion layers deposited.

The CVs shows a small broad oxidation wave at about 0.3 V and sharp reduction peak at about -0.15 V (vs Ag/AgCl). These peaks are attributed to the formation of palladium oxide (forward anodic scan), while on the return cathodic sweep, the surface oxide is reduced giving rise to a well-defined cathodic stripping peak [17]. These results suggest that although Pd is embedded in the Nafion LS film, the surface activity is similar to naked Pd.

Studies on different thickness films suggested a close correlation of the magnitude of the oxide stripping peak with film thickness, an initial increase of total charge was measured with the thickness of the film, reaching a plateaux for higher than 30 layers deposited. The total active surface area of Pd nanoparticles was estimated by integrating the charge passed in the Pd oxide stripping reaction (50 mV s^{-1}, 4^{th} scan) (Figure 4-12b). Following the procedure of Rand, a conversion factor of 424 μC cm^{-2} was used [31]. The surface area of a single nanoparticle has been approximated to be 7.85 x10^{-13} cm^2 considering 5 nm as the average diameter of the nanoparticles, as estimated by TEM. The number of particles incorporated within the film per unit volume of samples with different film thickness is listed in Table 4-1.

Table 4-1. Surface area and number of Pd particles.

Number of layers (thickness)	*Charge density / μC cm^{-2}*	*Surface Ratio / cm^2 Pd per cm^2 ITO*	*Active NPs density / number NPs x10^{15} cm^{-3}*
10 (15 nm)	1.69 ±0.8	0.4 x10^{-2} (±0.1) x10^{-2}	3.4 ±1
20 (30 nm)	7.25 ±0.8	1.7 x10^{-2} (±0.1) x10^{-2}	7.2 ±1
30 (45 nm)	10.1 ±0.8	2.5 x10^{-2} (±0.1) x10^{-2}	7.1 ±1
40 (60 nm)	9.0 ±0.8	2.1 x10^{-2} (±0.1) x10^{-2}	4.5 ±1
60 (90 nm)	9.3 ±0.8	2.2 x10^{-2} (±0.1) x10^{-2}	3.8 ±1

The nanoparticle density for the first 10 layers (15 nm thick film) deposited resulted sensibly lower (~3 x10^{15} NPs cm^{-3}) with respect the constant value obtained for 20 and 30 layers (~7 x10^{15} NPs cm^{-3}). A costant value obtained for 20 and 30 layers denotes a uniform formation of NPs within the film. Two effects can explain a lower density for the 10 layers samples: the first layers deposited form a film that could be less uniform; and/or the vicinity of the ITO surface could have an effect on the Pd(II) incorporation and reduction. When the thickness exceeded 30 layers (45 nm), the overall charge reached a constant value. This behaviour indicates that NPs located too far away from the conductive substrate are not in electrochemical contact.

4.3.2 Cyclic Voltammetry Investigations

The activity of the Pd ultra-thin Nafion LS films was further considered through studies of hydrogen oxidation. Palladium is receiving considerable attention in fuel cell technologies due to low cost, greater availability compared to platinum and its capability to absorb large quantities of hydrogen [16]. Figure 4-13 reports typical CVs for various modified ITO electrodes, specifically functionalised with a pristine 40 layers Nafion LS film (black line) and a 40

layers Pd/Nafion LS film, before (red line) and after (blue line) purging an aqueous 0.1 M KNO_3 solution with H_2.

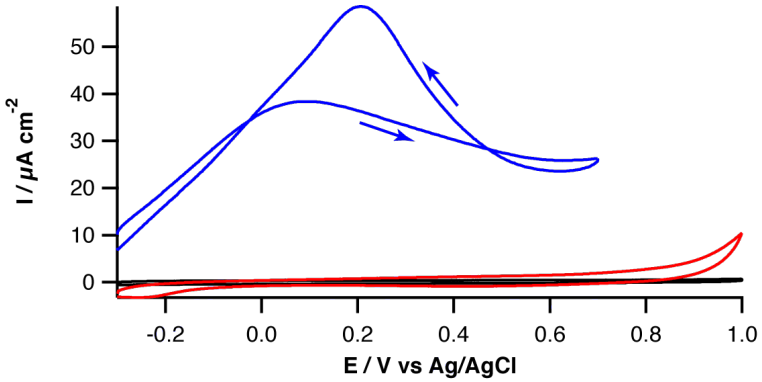

Figure 4-13. CVs of a 40 layer Pd/Nafion LS film before (red line) and after saturation with H_2 (blue line) in 0.1 M KNO_3 supporting electrolyte, scan rate 20 mV s^{-1}. The black line shows a CV of a 40 layer Nafion LS film on ITO after saturation of the solution with H_2.

The CV for Nafion on ITO after purging with H_2 reveals that the electrode is essentially inert with respect to the oxidation of H_2 over the potential range shown. The CV of the 40 layer Pd/Nafion film purged with N_2, shows the presence of the typical peak for the cathodic stripping of Pd oxide at about -0.22 V (vs Ag/AgCl). Note that the potential of the cathodic peak is shifted cathodically by about 0.2 V compared to the peak evidenced in Figure 4-12, because the pH of the solution was *ca*. 6, causing the stripping of palladium oxide to occur at a more negative potential.

A dramatic change in the response was observed when the solution was purged with H_2: the CV reveals an oxidation peak at about 0.1 V (vs Ag/AgCl), characteristic of the oxidation of hydrogen [32]. Note that the peak current density value of 35 μA cm^{-2} is about half that expected for a diffusion-limited reaction, assuming 10^{-3} mol dm^{-3} as the concentration of H_2 after saturation in aqueous solution and a diffusion coefficient of 5 x10^{-5} cm^2 s^{-1} [33]. At potentials

beyond the peak value, the current magnitude decreases significantly and then, surprisingly, increases during the reverse scan. This behaviour can be attributed to the fact that during the oxidation scan there is the concomitant formation of Pd oxide with hydrogen oxidation. Oxide formation leads to passivation of the Pd nanoparticles thus resulting in a decrease in the rate of hydrogen oxidation. Thus, during the reverse (reduction) scan, the electrode is bathed in hydrogen and, as oxide is removed from the surface, the hydrogen oxidation reaction is able to occur at driving potentials.

4.3.3 Scanning Electrochemical Microscopy Studies

Ultra-thin Nafion LS films of 15 layers on glass supports were employed to incorporate the Pd NPs and the hydrogen evolution reaction (HER) was investigated using the SECM technique [34, 35]. The potential at the Au/Hg UME was set at -0.9 V, 0.3 mM methyl-viologen (MV) was used as mediator and 0.1 M KNO_3 as supporting electrolyte. An increase of the current was expected approaching the surface of the sample because of the regeneration of the mediator involved in the HER (1). When in bulk MV^{2+} was reduced to MV^{+} at the working electrode (Au/Hg UME) giving a steady state current, but approaching the substrate with the UME the MV^{+} diffuses toward the substrate and in presence of Pd NPs it acts as reducer in the hydrogen evolution reaction (Figure 4-14) regenerating MV^{2+}. If the HER is effective, then decreasing the distance between the UME and the substrate results in increasing regeneration of MV^{2+} (oxidation) at the substrate.

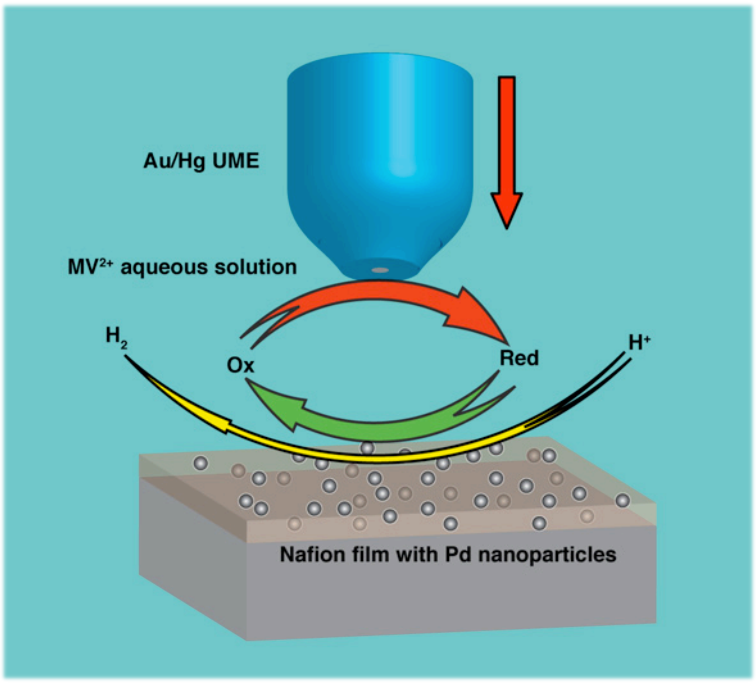

Figure 4-14. SCEM schematic for hydrogen evolution promoted by Pd nanoparticles.

$$\begin{aligned} &UME: && MV^{2+} + e^- \rightarrow MV^{\bullet+} \\ &Substrate: && 2MV^{\bullet+} + 2H^+ \xrightarrow{Pd} H_2\uparrow + 2MV^{2+} \end{aligned} \qquad (1)$$

Consistent with this process, an increase of the MV^{2+} feedback current was expected with higher concentration of protons (lower pH). To prove this, a series of approach curve measurements were produced in buffered (phthalate/HCl/NaOH) solutions at different pH (pH 3, 4 and 5).

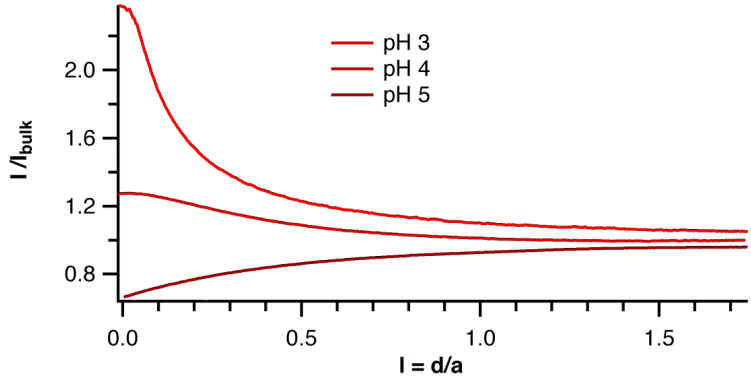

Figure 4-15. Normalized experimental approach curves for the reduction of MV^{2+} at of a Au/Hg UME at different pH approaching an ultra-thin Nafion LS film incorporated Pd NPs.

Figure 4-15 plots the feedback current normalized by the bulk current against the distance from the surface normalized by the radius of the metal wire of the UME (12.5 μm). The increase of the feedback current at lower pH, as stated in (1), confirmed the dependence of the reaction on the protons concentration, proving the evolution of hydrogen catalyzed by the palladium nanoparticles inside the Nafion LS film.

4.3.4 Improvement of Electroactivity by Potential Preconditioning

The results in Figure 4-13 suggested that it might be beneficial to precondition the electrode by forming Pd oxide at anodic potentials, quickly stripping it from the surface, followed by an anodic sweep for hydrogen evolution. The beneficial effect is clearly visible in Figure 4-16 which reports the forward anodic linear sweep voltammograms (LSVs) for hydrogen oxidation for the same 40 layer Pd/Nafion LS film without (red line) and with (black lines) the application of a conditioning anodic potential (various values in the range 0.5 - 1.2 V, 30 s duration). The magnitude of anodic peak current under these conditions increased with increasingly anodic preconditioning potential, reaching a maximum value at 1 V and beyond (Figure 4-16). Each LSV at different preconditioning potential was followed by a test LSV in which the preconditioning potential was kept at 1.1 V (30 s), and always giving the same current response. Thus, the trend shown is entirely due to the preconditioning potential.

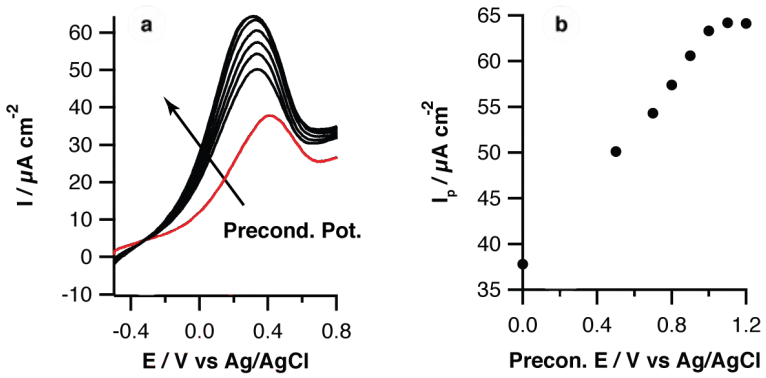

Figure 4-16. (a) LSV of a 40-layer Pd/Nafion LS film, supporting electrolyte 0.1 M KNO_3, scan rate 100 mV s^{-1}, after saturation with H_2: without preconditioning (red line) and with preconditioning at 0.5, 0.7, 0.8, 0.9, 1.1 and 1.2 V for 30 s (solid line). (b) LSV peak current magnitude, I_p, vs preconditioning potential.

Coupled with the earlier observations, these results suggest that the procedure herein produces electrochemically active Pd NPs, without any protecting group, which are characterised by the usual oxide formation/stripping of naked Pd nanoparticles.

4.4 Conclusions

In summary, a very simple procedure has been developed for functionalising ultra-thin Nafion LS films with relatively monodisperse Pd nanoparticles. The nanoparticles have typical characteristics of naked Pd and are electrochemically active towards the catalytic oxidation of hydrogen.

4.5 Bibliography

[1] Fendler, J. H.; *Nanoparticles and Nanostructured Films: Preparation Characterization and Applications*; WILEY-VCH Verlag Weinheim: Germany, 1998.

[2] Thomas, J. M.; Johnson, B. F.; Raja, R.; Sankar, G.; Midgley, P. A.; *Acc. Chem. Res.* **2003**, *36*, 20-30.

[3] Lewis, L. N.; *Chem. Rev.* **1993**, *93*, 2693-2730.

[4] Campbell, C. T.; Parker, S. C.; Starr, D. E.; *Science* **2002**, *298*, 811-814.

[5] Mandal, S.; Roy, D.; Chaudhari, R. V.; Sastry, M.; *Chem. Mater.* **2004**, *16*, 3714-3724.

[6] Riahi, G.; Guillemot, D.; Polisset-Thfoin, M.; Khodadadi, A. A.; Fraissard, J.; *Cat. Today* **2002**, *72*, 115-121.

[7] Moreno-Mañas, M.; Pleixats, R.; Villarroya, S.; *Chem. Commun.* **2002**, 60-61.

[8] O'Mullane, A. P.; Dale, S. E.; Macpherson, J. V.; Unwin, P. R.; *Chem. Commun.* **2004**, 1606-1607.

[9] Nicholson, P. G.; Ruiz, V.; Macpherson, J. V.; Unwin, P. R.; *Chem. Commun.* **2005**, 1052-1054.

[10] Zhao, J.; Bradbury, C. R.; Huclova, S.; Potapova, I.; Carrara, M.; Fermín, D. J.; *J Phys Chem B* **2005**, *109*, 22985-22994.

[11] Ruiz, V.; Nicholson, P. G.; Jollands, S.; Thomas, P. A.; Macpherson, J. V.; Unwin, P. R.; *J. Phys. Chem. B* **2005**, *109*, 19335-19344.

[12] Gittins, D. I.; Caruso, F.; *Angew. Chem. Int. Ed. Engl.* **2001**, *40*, 3001-3004.

[13] Henglein, A.; Giersig, M.; *J. Phys. Chem. B* **1999**, *103*, 9533-9539.

[14] van Herrikhuyzen, J.; Janssen, R. A.; Meijer, E. W.; Meskers, S. C.; Schenning, A. P.; *JACS* **2006**, *128*, 686-687.

[15] Lévy, R.; Thanh, N. T.; Doty, R. C.; Hussain, I.; Nichols, R. J.; Schiffrin, D. J.; Brust, M.; Fernig, D. G.; *JACS* **2004**, *126*, 10076-10084.

[16] Rao, C. R. K.; Trivedi, D. C.; *Coord. Chem. Rev.* **2005**, *249*, 613-631.

[17] Bartlett, P. N.; Gollas, B.; Guerin, S.; Marwan, J.; *Phys. Chem. Chem. Phys.* **2002**, *4*, 3835-3842.

[18] Guerin, S.; Attard, G. S.; *Electrochem. Commun.* **2001**, *3*, 544-548.

[19] Platt, M.; Dryfe, R. A. W.; Roberts, E. P. L.; *Electrochim. Acta* **2004**, *49*, 3937-3945.

[20] Dryfe, R. A.; Simm, A. O.; Kralj, B.; *JACS* **2003**, *125*, 13014-13015.

[21] Gierke, T. D.; Munn, G. E.; Wilson, F. C.; *J. Polym. Sci., Part B: Polym. Phys.* **1981**, *19*, 1687-1704.

[22] Kordesch, K.; Simader, G.; *Fuel Cells and their Applications*; WILEY-VCH Verlag Weinheim: Germany, 1996.

[23] Rikukawa, M.; Sanui, K.; *Prog. Polym. Sci.* **2000**, *25*, 1463-1502.

[24] Mauritz, K. A.; Moore, R. B.; *Chem. Rev.* **2004**, *104*, 4535-4586.

[25] Smitha, B.; Sridhar, S.; Khan, A. A.; *J. Membr. Sci.* **2005**, *259*,

10-26.

[26] Bertoncello, P.; Ram, M. K.; Notargiacomo, A.; Ugo, P.; Nicolini, C.; *Phys. Chem. Chem. Phys.* **2002**, *4*, 4036-4043.

[27] Bertoncello, P.; Notargiacomo, A.; Nicolini, C.; *Langmuir* **2005**, *21*, 172-177.

[28] Ugo, P.; Bertoncello, P.; Vezzà, F.; *Electrochim. Acta* **2004**, *49*, 3785-3793.

[29] Bertoncello, P.; Ciani, I.; Li, F.; Unwin, P. R.; *Langmuir* **2006**, *22*, 10380-10388.

[30] Bertoncello, P.; Ciani, I.; Marenduzzo, D.; Unwin, P. R.; *J. Phys. Chem. C* **2006**, .

[31] Rand, D. A. J.; Woods, R.; *J. Electroanal. Chem.* **1971**, *31*, 29-38.

[32] Zurowski, A.; Lukaszewski, M.; Czerwiński, A.; *Electrochim. Acta* **2006**, *51*, 3112-3117.

[33] Macpherson, J. V.; Unwin, P. R.; *Anal. Chem.* **1997**, *69*, 5045-5051.

[34] Sun, P.; Laforge, F. O.; Mirkin, M. V.; *Phys. Chem. Chem. Phys.* **2007**, *9*, 802-823.

[35] Edwards, M. A.; Martin, S.; Whitworth, A. L.; Macpherson, J. V.; Unwin, P. R.; *Physiol. Meas.* **2006**, *27*, R63-108.

Chapter 5 DECORATION OF CONDUCTIVE SUBSTRATE WITH ELECTROACTIVE METAL NANOPARTICLES B: ELECTRODE FUNCTIONALISATION BY POTENTIAL-ASSISTED ASSEMBLY OF PLATINUM NANOPARTICLES

A method for Assembling Pt Nanoparticles (5 nm diameter) on ITO and HOPG electrodes, via the potential-assisted deposition of pre–formed perthiolated-ß-cyclodextrin-capped Pt nanoparticles is described. Cyclic voltammetry allowed control over the surface coverage of monodisperse Pt nanoparticles in a simple fashion, as evidenced by the voltammetric response and atomic force microscopy of the resulting electrode surface. The Pt nanoparticle arrays formed in this way were electrocatalytically active towards proton reduction-hydrogen evolution. The methodology described thus opens up a new approach for the deposition of metal nanoparticles with controlled surface density for the investigation of electrocatalytic processes.

5.1 Introduction

The assembly of metal nanoparticles on surfaces is currently of considerable interest due to widespread applications, ranging from catalysis to sensing. Among metal nanoparticles, platinum is of primary importance and significant efforts have been made to develop strategies to functionalize conductive (electrode) substrates; the resulting nanostructured interfaces have applications in sensors, fuel cell development and other electrocatalytic processes [1-3]. A significant goal is to obtain uniform deposition of monodisperse nanoparticles with good electrical connection to the substrate. Controlling the nanoparticle density is a key step to understand its effect on electrocatalytic performance and extract single particle reactivity. There are two basic approaches. First, the preparation of metal nanoparticles by stabilization in solution via partial or complete coverage with organic ligands [4-8], followed by deposition [9-10]. Size control of platinum nanoparticles with a narrow dispersion has been achieved, but surface immobilization sometimes requires that the substrate be functionalized with organic monolayers or polymers that could restrict the electrical contact. In addition, the nanoparticle protecting layer may decrease the catalytic activity [11]. The second approach is direct synthesis on solid supports using chemical [12] or electrochemical methods [13, 14]. Notably, Penner and coworkers reported the electrodeposition of various metal nanocrystallites (eg Pt, Pd, Ag) on HOPG using a pulsed potentiostatic procedure to deposit metal from the corresponding metal salt solution [15, 16]. This affords some control of the nanoparticles size although variation of the particle coverage over a wide range of values is more difficult and deposition may occur

preferentially at favourable nucleation sites on the surface, leading to a spatially inhomogeneous distribution.

Here we describe a convenient method for obtaining arrays of monodisperse Pt nanoparticles on conductive surfaces in a controlled fashion, through potential-assisted deposition of pre–formed perthiolated-β-cyclodextrin-capped Pt nanoparticles utilising CV. We show that this method allows the precise quantitative control of the attachment of Pt nanoparticles on indium thin oxide (ITO) and HOPG and that the assembled Pt nanoparticles have good electrochemical characteristics. The ability to assemble nanoparticles on electrodes with precise coverage, by potential cycling, opens up interesting possibilities on using such an approach for the fabrication of nanostructured interfaces.

5.2 Experimental

5.2.1 Synthesis of Perthiolated β-CD-Capped Platinum Nanoparticles

Perthiolated-β-cyclodextrins were synthesized according to known literature procedures with slight variations, using the per-6-iodo-β-cyclodextrin as an intermediate [17, 18]. The synthesis was carried out under an inert gas (nitrogen) atmosphere.

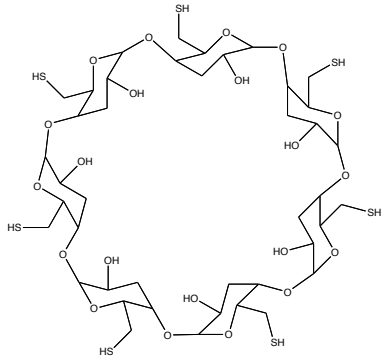

Figure 5-1. Perthiolated-b-cyclodextrins structure.

Perthiolated-β-Cyclodextrin-capped Pt nanoparticles (PtCD NPs) were synthesised via a procedure based on that of Kaifer and coworkers [19].

Briefly, 90 mg of K_2PtCl_4 (0.220 mmol) was dissolved in 20 ml of DMF (dried over activated molecular sieves, 4Å). 30 mg of the stabilizing ligand $CD(SH)_7$ (0.025 mmol) was added, along with 90 mg of sodium borohydride (2.4 mmol). The reaction mixture was stirred at room temperature for 48 hours. During the last 12 hours, the mixture turned into a dark brown colour, indicating the formation of a Pt colloid. The crude product was centrifuged at 15000 rpm for 20 minutes, resulting in the precipitation of a brown waxy substance. This substance was re-suspended in 10 ml DMF and again centrifuged. This washing procedure was repeated 3 times to eliminate any excess of the cyclodextrin. The brown precipitate was then re-suspended in 10:1 (v/v) ethanol:water with 15 minutes ultrasonication and centrifuged again at 15000 rpm for 20 minutes. The last procedure was repeated 3 times to wash away the DMF. Finally, the nanoparticles were dried under high vacuum for 48 h at 40 ºC.

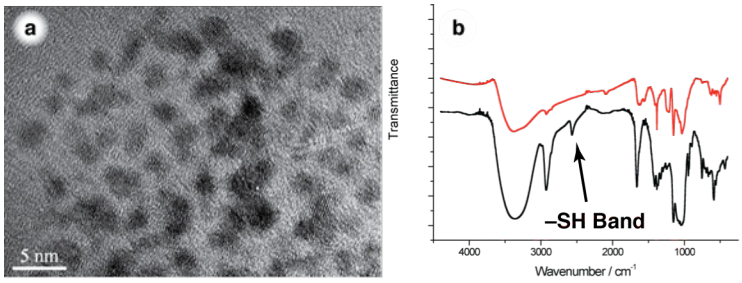

Figure 5-2. (a) HR-TEM images of PtCD NPs, (b) IR spectra of Perthiolated-β-cyclodextrin (black line) and PtCD NPs (red line).

The size of the chemically-synthesized PtCD NPs was determined using HR-TEM (Figure 5-2a). The average size of these Pt nanoparticles was 5 ±1 nm with a Pt spacing lattice of 2.27 Å, which is consistent with the known lattice parameter of 2.265 Å for the (111) plane for the platinum fcc crystal structure [20].

In Figure 5-2,b the IR spectrum of pure perthiolated-β-CD shows the typical SH band at 2500 cm^{-1} which disappears after the formation of the PtCD NPs since the sulphur is bound to the platinum surface.

5.2.2 Potential-assisted Deposition

For nanoparticle deposition on ITO, a one-compartment cell was used with a defined area of the electrode sample exposed, which allowed the solution to be maintained under a nitrogen atmosphere (Figure 4-9). Deposition on HOPG substrate were performed using a simple purpose-built Teflon sheath cell (Figure 5-3), gently positioned on a freshly prepared HOPG.

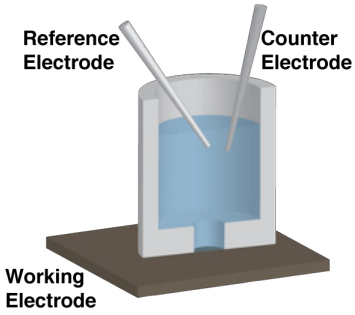

Figure 5-3. Teflon sheath cell electrochemical set up.

Typically, solutions of perthiolated-β-CD-capped Pt nanoparticles contained 1 mg of β-CD-capped Pt nanoparticles in 2.5 mL deionised water together with supporting electrolyte (1 M KCl) were sonicated for 2 hours and then filtered using Sartorius Minisart High-Flow 0.22 μm filters before use.

Cyclic voltammetry and CV were recorded using the cell in Figure 4-9 and in Figure 5-3, respectively. A conventional three-electrode configuration was used, where the working electrode was an ITO glass plate or HOPG substrate, a platinum coil as a counter electrode and a Ag/AgCl electrode was used as the reference electrode.

5.3 Results and Discussion

5.3.1 Platinum Nanoparticles Deposition

A typical set of 100 CVs for the deposition of perthiolated-β-CD-capped Pt nanoparticles on an ITO electrode is shown in Figure 5-4. The potential was scanned from +1.0 V to -0.8 V (0.1 V s^{-1}) to ensure that a wide range of electrode/electrolyte potentials were covered and also so that the characteristic voltammetric features associated with the Pt surface could be ascertained.

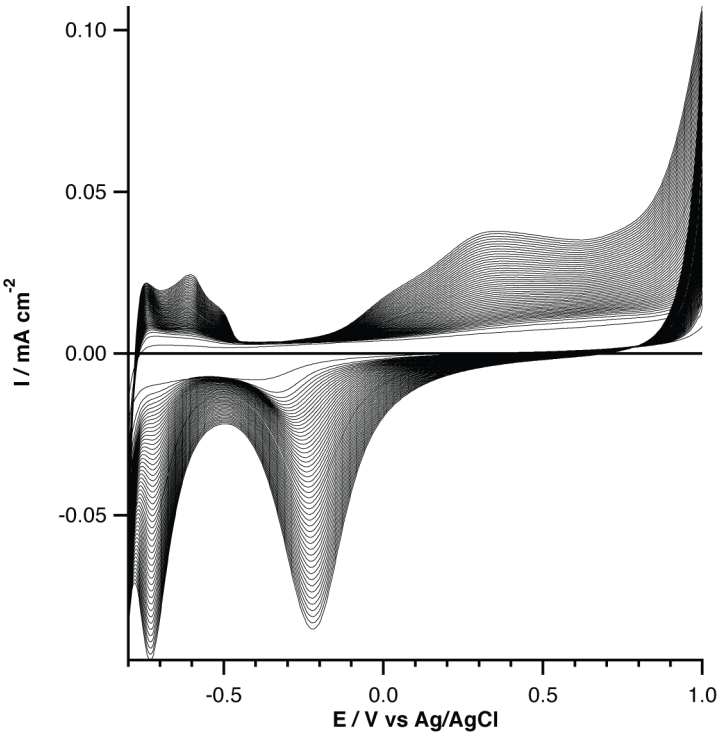

Figure 5-4. CVs (100 cycles) of β-CD-capped Pt nanoparticles on an ITO electrode substrate from 0.1 M KCl supporting electrolyte (scan from +1 V to -0.8 V); scan rate 0.1 V s^{-1}.

In particular, the CVs show a peak for the surface oxidation of Pt at around 0.4 V vs Ag/AgCl, and a corresponding reduction peak of Pt oxide at -0.2 V. There are also clear hydrogen adsorption-desorption peaks at -0.7 V and -0.6 V, respectively [20]. The wide potential scan employed and the fact that negative potentials are applied is expected to be effective in promoting the reductive desorption of the mediated ligand leaving a native Pt surface. All of these features increase monotonically as the number of cycles increase, indicating an increasing amount of Pt deposited on the surface. Figure 5-5 summarises how the surface coverage changes with the number of potential cycles. To compute the surface concentration of NPs the charge passed in the oxide stripping peak was evaluated, and using a conversion factor of 410 μC cm^{-}

^{2} [21] the total surface area was obtained which was converted to particles number assuming spherical particles of diameter 5 nm.

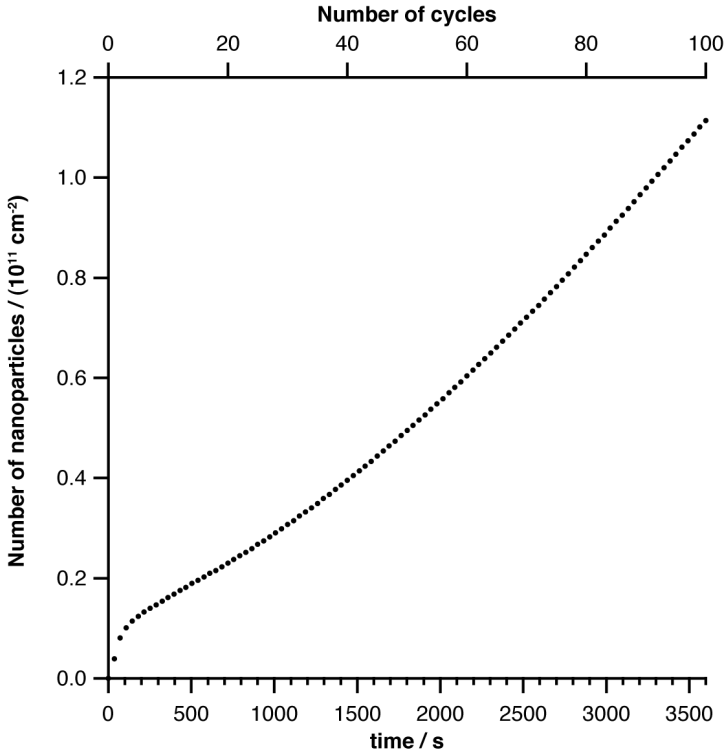

Figure 5-5. Pt nanoparticle number vs time (lower x-axis) and vs number of voltammetric scans (upper x-axis).

In the time domain from 1000 s to 3000 s the Pt nanoparticles coverage increase by 10 μm^{-2} in each cycle, highlighting the high control over deposition obtainable. Similar behaviour to that in Figure 5-4 was observed for the HOPG electrode. In this case it was possible to visualize the result of deposition using TM-AFM.

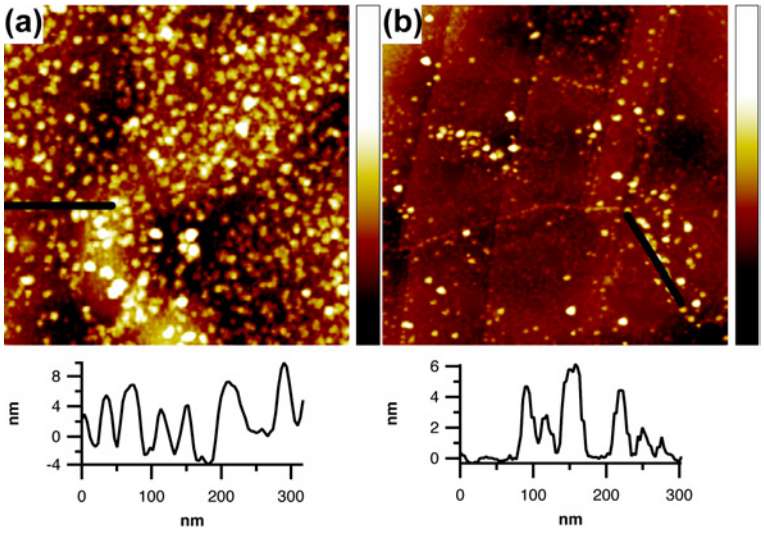

Figure 5-6. AFM topography images (1 x 1 µm) Pt nanoparticles deposited on HOPG by potential-assistance (a) and without (b). The profiles correspond to the black lines in each image. The z full colour scale corresponds to 26 and 9.5 nm respectively.

Figure 5-6 shows typical TM-AFM topography images of the PtCD NPs electrodeposited on HOPG after 1 hour (100 cycles) (a) and compares this to the case of unbiased HOPG substrate (1h) (b). The images clearly show that potential-assisted deposition results in a high surface density of nanoparticles that are uniformly deposited, with evidence of only a little aggregation at this relatively high surface coverage. Notably, the deposition of nanoparticles is much less extensive without applying a potential sweep. These are particularly interesting results which contrasts markedly with the electrodeposition of Pt nanoparticles on HOPG that leads to a non–uniform Pt deposition, with preferential formation at step edges [15].

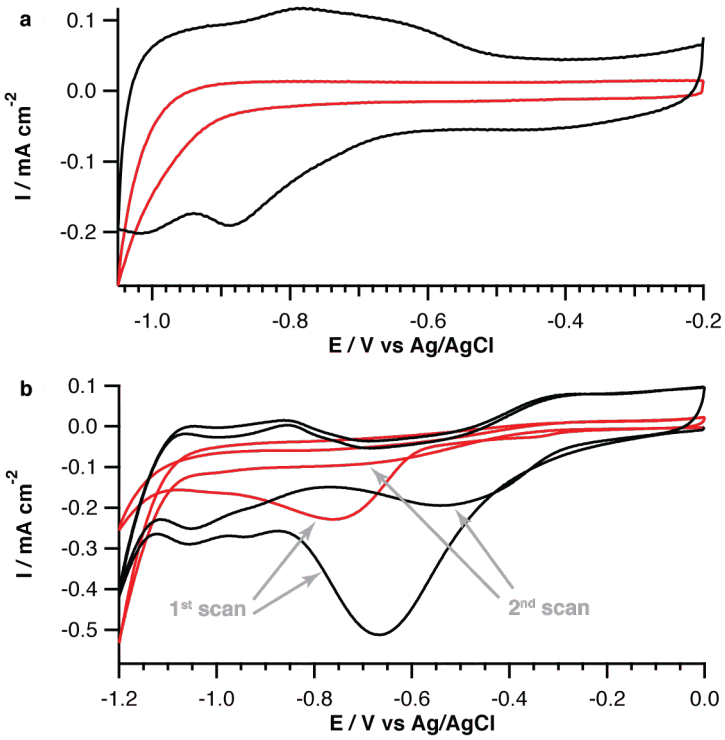

Figure 5-7. CVs of PtCD NPs deposited on an ITO electrode for 60 minutes by the potential-assisted method (black line). For 100 cycles, and without (red line); 0.1 M KNO_3 solution scan rate 0.5 V s^{-1}. (a) degassing with N_2 and (b) without degassing the electrolyte solution.

Figure 5-7a provides further evidence of the effectiveness of the potential-assisted method for promoting nanoparticle deposition. This figure compares CVs recorded at Pt-functionalised-ITO surfaces, following 100 voltammetric cycles (60 minutes) and without applying a potential for the 60 minutes using the sealed electrochemical cell with deaeration of the electrolyte solution (0.1 M KNO_3) with N_2. The resulting CV for the potential-cycled electrode clearly shows hydrogen adsorption/desorption features on platinum, denoting that there is significant Pt deposition, whereas without cycling, these features are almost absent. In Figure 5-7b the same experiment was carried out, but without deaerating the solution. In this case, dissolved oxygen is in solution, in equilibrium with the atmosphere. The first scan in both

the samples, potential assisted and not assisted deposition, shows a peak for the reduction of platinum oxide at -0.66 V and -0.75 V, respectively. For the NPs deposited with the potential-assisted protocol, a higher peak current evidences a greater Pt deposition with respect the sample deposited without applying any potential. The second scan supports this behaviour, showing clear diffusive oxygen reduction peak at -0.5 V for the potential-assisted deposited NPs which is almost missing in the scan for the other sample. This again confirms the role of the potential sweep in depositing the PtCD NPs to achieve greater (and controlled) deposition, consistent with the TM-AFM images (Figure 5-6) where the amount of PtCD NPs was substantially lower without the application of a deposition potential programme.

5.3.2 Oxygen Reduction Evaluation

Oxygen reduction at platinum surfaces follows several different pathways depending on the pH, crystal plane and electrolytes dissolved in solution [23-26]. Normally a mixed behaviour is found. The possible complex reactions can be summarised in terms of two different pathways: a direct 4-electron reduction or a two steps comprising 2-electron reduction in each, (2), (3), respectively:

$$O_2 + 4H^+ + 4e^- \rightarrow 2H_2O \qquad (2)$$

$$\begin{aligned} O_2 + 2H^+ + 2e^- &\rightarrow H_2O_2 \\ H_2O_2 + 2H^+ + 2e^- &\rightarrow 2H_2O \end{aligned} \qquad (3)$$

CA was employed to evaluate which type of pathway reaction oxygen reduction followed at the PtCD NP functionalized electrode. Reactions of a solute at a single NP isolated is regulated by a hemispherical diffusive-controlled system, hence a functionalized surface can act as an array of nanoelectrodes

depending on the dispersion of the NPs. For a high density NPs on an electrode, the electrode behaves like a planar diffusive controlled system due to the overlap of the hemispherical diffusion profile of the NPs (Figure 5-8) [27, 28].

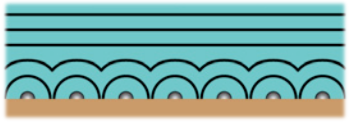

Figure 5-8. Overlapping hemispherical diffusion.

The behavior of the current density, i_d for a potential-driven reaction under planar diffusion is described by the Cottrell equation [29]

$$i_d = \frac{n\mathrm{F}D^{1/2}C}{\pi^{1/2}t^{1/2}} \qquad (4)$$

Where C is the concentration of O_2 dissolved in water in equilibrium with the atmosphere (2.5×10^{-7} mol cm^{-3} [24]), D is the O_2 diffusion coefficient (2.28×10^{-5} cm^2 s^{-1} [24]), n is the number of electrons involved in the reaction, F (94.485 C mol^{-1}) is the Faraday constant and t the time. Since the equation shows linearity between the density current and the reciprocal of the square root of time, the number of electrons involved on the reaction (n) can be easily obtained from the gradient. For a 2 electron reaction the theoretical gradient is 1.3×10^{-4} A s$^{1/2}$ cm^{-2}, while it is 2.6×10^{-4} A s$^{1/2}$ cm^{-2} for a 4 electron process.

To obtain a constant and reproducible active area for the working electrode (Pt NP functionalized ITO), the electrochemical cell depicted in Figure 4-9 was used and to avoid interferences due to the presence of platinum oxide during the reduction of O_2, which is normally formed by applying a positive potential >0.1 V vs Ag/AgCl or long oxygen exposure, a 3 step CA procedure was employed: i) an initial negative potential of -0.8 V was applied for 5 s to reduce any platinum oxide on the metal NPs; ii) the potential was then held at -

0.1 V vs Ag/AgCl for a further period of 5 s in which no electrochemical processes occurred; iii) the potential was jumped again to -0.8 V vs Ag/AgCl to perform the actual CA measurement used to evaluate the number of electrons involved in the oxygen reduction (Figure 5-9a).

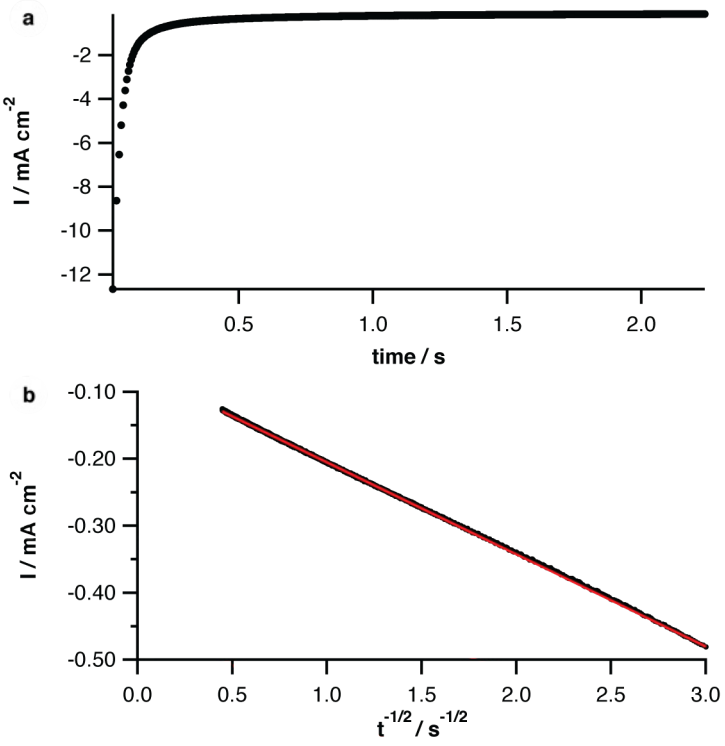

Figure 5-9. (a) CA voltammogram of Pt NPs functionalized ITO in buffered solution (pH 7, Table 2-2) and (b) Cottrell plot.

Figure 5-9b shows the current density against the reciprocal square root of time for the last step of the CA. Note that at times shorter than 100 ms have not been considered because the capacitative current plays a non–negligible role in the overall current. The curve shows a strict linear behaviour supporting a planar-diffusion controlled system required to validate the Cottrell equation. The data were fitted by a linear equation and the gradient of the curve resulted -1.4 x10^{-4} A $s^{1/2}$ cm^{-2} very close to the theoretical value of -1.3 x10^{-4} A $s^{1/2}$ cm^{-2} suggesting a strong predominant 2-electron reaction pathway.

5.3.3 Hydrogen Reduction and Evolution Activity

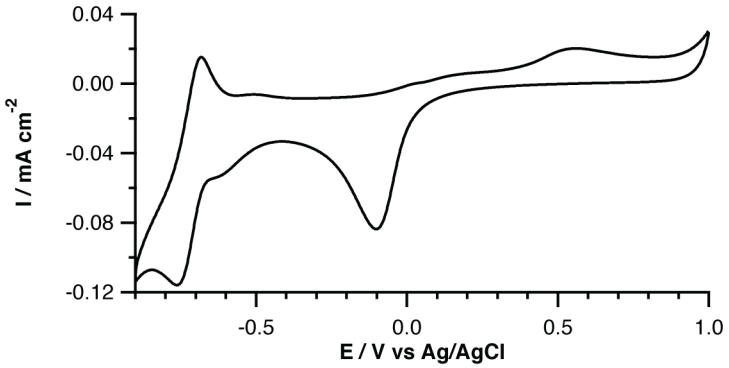

Figure 5-10. CV (0.1 V s^{-1}) of PtCD NPs functionalised ITO electrode in 0.1 M KNO_3 solution acidified to pH 3 with HNO_3.

Figure 5-10 shows a typical CV of immobilized Pt nanoparticles recorded in a solution of 0.1 M KNO_3 acidified to pH 3 by addition of nitric acid. In addition to the typical oxidation and reduction peaks, ascribed to the formation and stripping of Pt oxide (at 0.5 V and -0.1 V, respectively), the CV clearly depicts a reduction peak of protons to hydrogen (-0.75 V) in the cathodic-going scan and the corresponding oxidation of hydrogen to protons (-0.7 V) in the anodic scan. The reversibility of the H^+/H_2 couple, which compares very favourably to that of bulk Pt under similar conditions [30], is further proof of the excellent electrocatalytic activity of the Pt nanoparticles deposited using the method described herein.

5.4 Conclusions

We have demonstrated a simple method to precisely tune the density of functionalized Pt nanoparticles on electrode surfaces (ITO and HOPG) using CV

has been demonstrated. The various CV responses reported herein also indicates that such Pt nanoparticles are active, showing the classical voltammetric signal for oxide formation and stripping and hydrogen adsorption/desorption. It is likely that this is a consequence of stripping of the protecting thiolate ligand during the deposition process. The method described provides an effective means for depositing metal nanoparticles on an electrode surface where a precise density of relatively uniformly dispersed nanoparticles is desired.

5.5 Bibliography

[1] Templeton, A. C.; Wuelfing, W. P.; Murray, R. W.; *Acc. Chem. Res.* **2000**, *33*, 27-36.

[2] Thomas, J. M.; Johnson, B. F.; Raja, R.; Sankar, G.; Midgley, P. A.; *Acc. Chem. Res.* **2003**, *36*, 20-30.

[3] Taton, T. A.; Mirkin, C. A.; Letsinger, R. L.; *Science* **2000**, *289*, 1757-1760.

[4] Gittins, D. I.; Caruso, F.; *Angew. Chem. Int. Ed. Engl.* **2001**, *40*, 3001-3004.

[5] van Herrikhuyzen, J.; Janssen, R. A.; Meijer, E. W.; Meskers, S. C.; Schenning, A. P.; *JACS* **2006**, *128*, 686-687.

[6] Lévy, R.; Thanh, N. T.; Doty, R. C.; Hussain, I.; Nichols, R. J.; Schiffrin, D. J.; Brust, M.; Fernig, D. G.; *JACS* **2004**, *126*, 10076-10084.

[7] Ye, H.; Crooks, R. M.; *JACS* **2005**, *127*, 4930-4934.

[8] Ye, H.; Crooks, R. M.; *JACS* **2007**, *129*, 3627-3633.

[9] Ruiz, V.; Nicholson, P. G.; Jollands, S.; Thomas, P. A.; Macpherson, J. V.; Unwin, P. R.; *J. Phys. Chem. B* **2005**, *109*, 19335-19344.

[10] Grabar, K. C.; Smith, P. C.; Musick, M. D.; Davis, J. A.; Walter, D. G.; Jackson, M. A.; Guthrie, A. P.; Natan, M. J.; *JACS* **1996**, *118*, 1148-1153.

[11] Zamborini, F. P.; Hicks, J. F.; Murray, R. W.; *JACS* **2000**, *122*, 4514-4515.

[12] Rao, C. R. K.; Trivedi, D. C.; *Coord. Chem. Rev.* **2005**, *249*, 613-631.

[13] Tel-Vered, R.; Bard, A. J.; *J. Phys. Chem. B* **2006**, *110*, 25279-25287.

[14] Day, T. M.; Unwin, P. R.; Wilson, N. R.; Macpherson, J. V.; *JACS* **2005**, *127*, 10639-10647.

[15] Zoval, J. V.; Lee, J.; Gorer, S.; Penner, R. M.; *J. Phys. Chem. B* **1998**, *102*, 1166-1175.

[16] Liu, H.; Penner, R. M.; *J. Phys. Chem. B* **2000**, *104*, 9131-9139.

[17] Ashton, P. R.; Kniger, R.; Stoddart, J. F.; Alker, D.; Harding, V. D.; *J. Org. Chem.* **1996**, *61*, 903-908.

[18] Rojas, M. T.; Koeniger, R.; Stoddart, J. F.; Kaifer, A. E.; *JACS* **1995**, *117*, 336-343.

[19] Alvarez, J.; Liu, J.; Román, E.; Kaifer, A. E.; *Chem. Commun.* **2000**, 1151-1152.

[20] Willwohl, H.; Wolfrum, J.; Zumbach, V.; Albers, P.; Seibold, K.; *J. Phys. Chem.* **1994**, *98*, 2242-2247.

[21] Furuya, N.; Koide, S.; *Surf. Sci.* **1989**, *220*, 18-28.

[22] Trasatti, S.; Petrii, O. A.; *J. Electroanal. Chem.* **1992**, *327*, 353-376.

[23] Shao, M. H.; Liu, P.; Adzic, R. R.; *JACS* **2006**, *128*, 7408-7409.

[24] PLETCHER, D.; SOTIROPOULOS, S.; *J. Electroanal. Chem.* **1993**, *356*, 109-119.

[25] Genies, L.; Bultel, Y.; Faure, R.; Durand, R.; *Electrochim. Acta* **2003**, *48*, 3879-3890.

[26] Yeager, E.; *Electrochim. Acta* **1984**, *29*, 1527-1537.

[27] Davies, T. J.; Moore, R. R.; Banks, C. E.; Compton, R. G.; *J.*

Electroanal. Chem. **2004**, *574*, 123-152.

[28] Davies, T. J.; Ward-Jones, S.; Banks, C. E.; del Campo, J.; Mas, R.; Munoz, F. X.; Compton, R. G.; *J. Electroanal. Chem.* **2005**, *585*, 51-62.

[29] Bard, A. J.; Faulkner, L. R.; *Electrochemical methods: fundamentals and applications* , 2nd ed.; John Wiley & Sons, Inc.: United States of America, 2001.

[30] Macpherson, J. V.; Unwin, P. R.; *Anal. Chem.* **1997**, *69*, 5045-5051.

Chapter 6 NUCLEATION AND GROWTH OF CALCIUM CARBONATE ON FOREIGN SUBSTRATES AT HIGH-SUPERSATURATION

The work presented in this chapter is focused on the dynamics of calcium carbonate deposition at high-supersaturated conditions onto foreign solid substrates. The deposition was investigated with a variety of techniques, both in–situ and ex–situ. Quartz crystal microbalance and optical microscopy studies allowed for a time resolved analysis of the deposition process, while scanning electron microscopy and microRaman gave a morphological characterisation of the phase deposited. Significant observations and outcomes of the studies undertaken include a detailed picture of phase transformations and the role of mass transport in the deposition process.

6.1 Introduction

The formation of $CaCO_3$ from supersaturated solution has been of primary importance in the fields of industrial chemistry, geochemistry and the life sciences, attracting considerable research effort for more than a century [1-5]. Scaling affects both daily life and industry, and is manifested, for example, as the incrustation of pipelines or the deposition on textiles during laundry. In nature, $CaCO_3$ is the most used material for biomineralisation. In the former area, many studies have been carried out to understand how the deposition of calcium carbonate on surfaces can be avoided [6-10]. In the later area, in contrast, investigations aim to understand the mechanism by which organisms are able to control the deposition and formation of different polymorphs of calcium carbonate [11-15].

Calcium carbonate is present as 3 anhydrous polymorphs (and 3 highly unstable hydrates) each with a distinctive crystallographic unit cell: trigonal calcite, orthorhombic aragonite and hexagonal vaterite, in order of thermodynamic stability (Figure 6-1) [16].

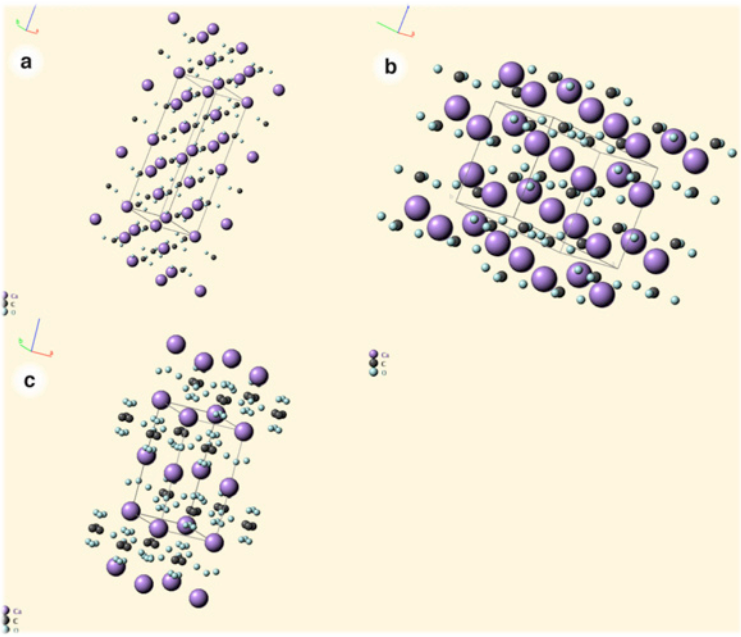

Figure 6-1. Crystallographic unit cell of (a) calcite, (b) aragonite and (c) vaterite.

In addition to a different unit cell all the polymorphs have characteristic morphologies. Calcite has a rhombohedral structure, while aragonite is needlelike and vaterite is typically found with a polycrystalline structure (Figure 6-2).

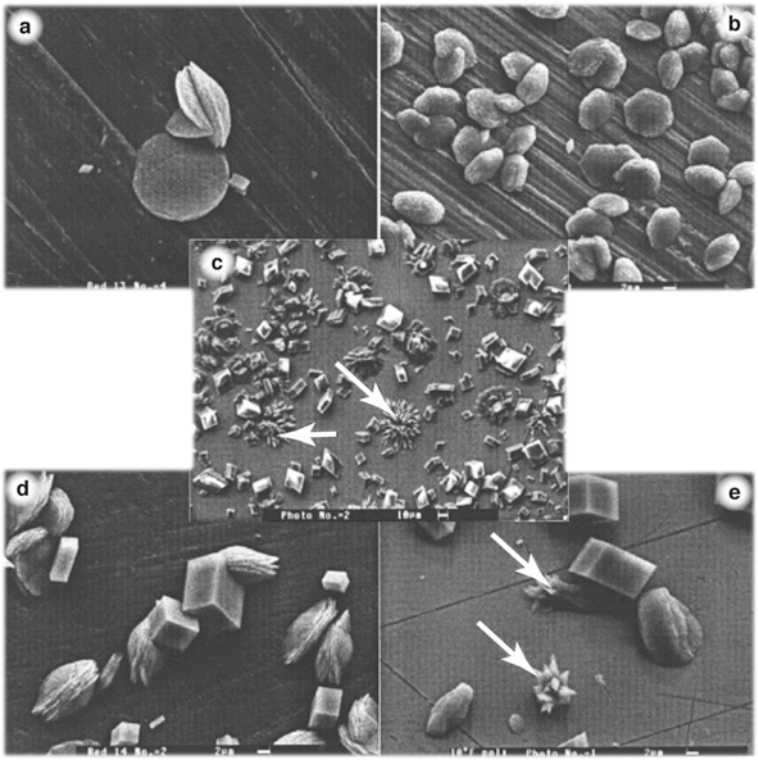

Figure 6-2. SEM images of calcium carbonate: (a) vaterite on bronze; (b) vaterite on stainless steel; (c) vaterite, calcite and aragonite on gold; (d) calcite and vaterite on vitreous carbon; (e) vaterite, calcite and aragonite on gold. Aragonite crystals are specified indicated with arrows (reproduced from reference [17]).

Both vaterite and aragonite are driven to a phase change to the more stable calcite [4, 18]. While aragonite always changes to calcite, vaterite is only driven directly to calcite a low temperatures (< 60 °C), while at higher temperatures (> 60 °C) an initial change to aragonite has been identified prior to transformation to calcite [16].

A focus of some work in the past few decades has been to investigate the processes of calcium carbonate nucleation and growth at solid/liquid interfaces. Heterogeneous nucleation and consequent growth has been mainly studied in low supersaturation environments. Under these conditions, the growth is slowed down and different types of kinetic investigation are facilitated. For example,

atomic force microscopy has been employed to characterise the speed at which steps move in a single growth spiral under conditions [19-23]. This approach gives a good understanding of growth kinetics at the nanoscale at low supersaturation conditions. A completely different approach is normally employed to investigate the nucleation of calcium carbonate crystals.

Research has mainly focused on homogeneous nucleation rather than heterogeneous. Interesting recent work of Gebauer *et al.* [24] indicates the formation of stable calcium carbonate clusters in equilibrium with the solution and, eventually, the formation of two different forms of ACC with different K_{sp} values, in the form of nanoparticles. Supersaturation was attained by increasing the concentration of calcium ions in solution from an initially undersaturated solution. This "soft" approach is different from conditions used in the work reported herein where high-supersaturation was reached almost instantly by mixing calcium and carbonate solutions, and a high driving force for nucleation was expected. Rieger *et al.* [25] used a similar procedure to investigate the initial stage of the homogeneous nucleation process. At high-supersaturation the process of crystal nucleation and growth is much more complex. In particular, kinetics prevails over thermodynamics and —for homogeneous nucleation— the less thermodynamically stable ACC polymorph is formed [26]. ACC nucleates as nanoparticles with a short-range order [27-29] that can be considered as the seed for the consequent phase change into vaterite or calcite.

Phase changes from ACC to vaterite and eventually calcite is the pathway considered to operate in the homogeneous nucleation and growth of calcite [18, 30]. Bolze *et al.* investigated the ACC formation process employing time-resolved small angle X-ray scattering (SAXS) [31], corroborating the initial

formation of ACC nanoparticles. Interestingly, the formation of vaterite or calcite was not observed in the first 300 s. Formation of ACC NPs occurred rapidly after a supersaturated solution was reached, the NP size (radius) increased quickly, reaching 75 nm after 1.5 s and a maximum of ~130 nm after 100 s [31].

In this chapter, a new system to investigate heterogeneous/homogeneous nucleation and growth at high-supersaturation conditions, under flow, is reported. The investigations aim to understand the processes which affect the growth of calcite. It is shown that heterogeneous nucleation and growth of calcite is influenced by the formation of ACC in solution, which deposits on the surface, and acts as a reservoir of material for the growing calcite, maintaining a high-supersaturated domain. A further important aspect of the work herein was that by utilising a solution composition that had carbonate as a limiting species, it was possible to evaluate which type of carbonate species in solution influenced the growth of calcite.

6.2 Experimental

6.2.1 Solution Preparation

Solutions of total concentration of calcium ion 20 mM and carbonate ion 10 mM were prepared by dissolving, respectively, $CaCl_2 \cdot 2H_2O$ and $NaHCO_3$ salts in MilliQ grade water; NaOH (1 M) was added to increase the pH to 10.50 ±0.05. The volume of NaOH added to the calcium solution was negligible. Two syringes were filled, one with the calcium ion solution and one with the

carbonate ion solution. These were prepared as quickly as possible to reduce exchange of CO_2 and satisfy the assumption of a closed system. The pH of the solutions after each step of the solution preparation and the amount of NaOH added to correct the pH was measured to compare experimental values with calculated ones. The model was consistent with the experimental pH measured and NaOH added for a close system (Table 6-1)

Table 6-1. Comparison of experimental and calculated pH and NaOH (1 M) added for 100 ml of carbonate solution.

Solution step preparation	*pH*		*NaOH added / µl*	
	Experimental	*Simulated*	*Experimental*	*Simulated*
Water	5.60 ± 0.05	5.60		
$NaHCO_3$ after dissolution	8.3 ±0.05	8.24		
$NaHCO_3$ after pH correction	10.5 ±0.05	10.50	700 ±20	700

Plastic syringes were filled with the solutions soon after the pH was adjusted to avoid exposure to atmosphere.

Table 6-2. Thermodynamic constants [24, 32] and activities of predominant solution species after mixing.

K_{sp}^{cal} *(calcite)*	3.44×10^{-9}	pH	9.99
K_{sp}^{ACC} *(ACC I)*	3.1×10^{-8}	$\{Ca^{2+}\}$	3.74×10^{-3}
S (calcite)	22.7	$\{CO_3^{2-}\}$	0.473×10^{-3}
S (ACC I)	8	$\{CaCO_3^{aq}\}$	2.61×10^{-3}

6.2.2 Time-lapse In–situ Growth Experiments

The microscopy cell was first filled with water and then calcium carbonate supersaturated solution was flowed in at 2 ml min^{-1} (1 ml min^{-1} for each solution) for a preset time. At the end of the experiment, the cell was filled with air and the glass substrate was quickly taken off and rinsed with acetone and blown dry with nitrogen. The glass substrates were cut into two pieces, through the centre, for micro-Raman spectroscopy and FE-SEM imaging after gold coating.

As highlighted in Table 6-2, high-supersaturation solution of ~23 with respect to calcite was reached after mixing of calcium and carbonate solutions. In–situ optical microscopy showed rapid formation of both calcite and ACC at the early stage of the experiment (see for example label 'a' in Figure 6-3), and a phase change from ACC to calcite is seen after ~500 sec (Figure 6-5).

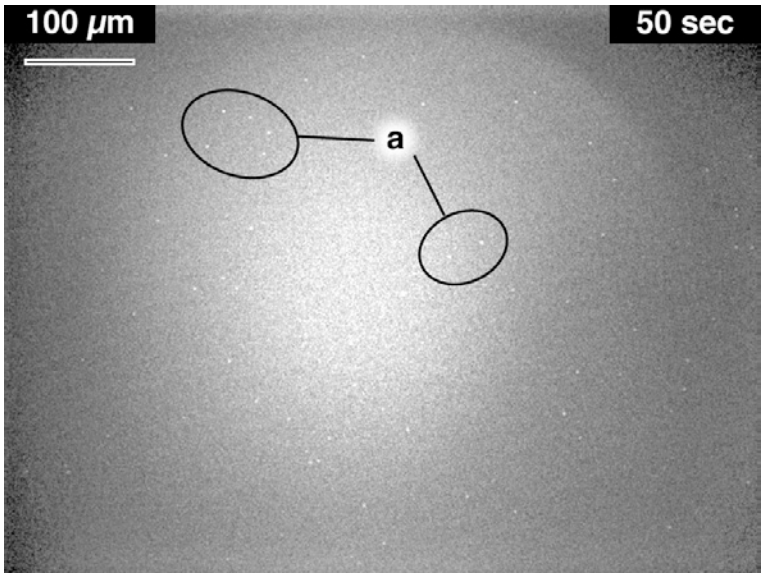

Figure 6-3. Time-lapse picture recorded with the in–situ microscopy set up at 50 s. 'a' initial heterogeneous nucleation of calcite.

An important observation was that after the initial nucleation further heterogeneous nucleation of calcite was not evident. At this stage of the process it is also possible to see formation of ACC with a floc structure on the surface (Figure 6-4). Since in our experiment, 22 s is needed for the solution to reach the substrate after the mixing, it is not clear if ACC nucleates directly on the surface where it growths or is formed in solution, leading to its agglomeration and aggregation on the surface. Bolze *et al.* [31] have shown an instantaneous nucleation of ACC in solution on a very rapid timescale (hundreds milliseconds), supporting the second hypothesis. On the movie 1 (see appendix), in which the microscope was focused in the solution near to the inlet, it is clear that there is the deposition of ACC with a floc structure on the surface of the glass confirming the formation of ACC in solution.

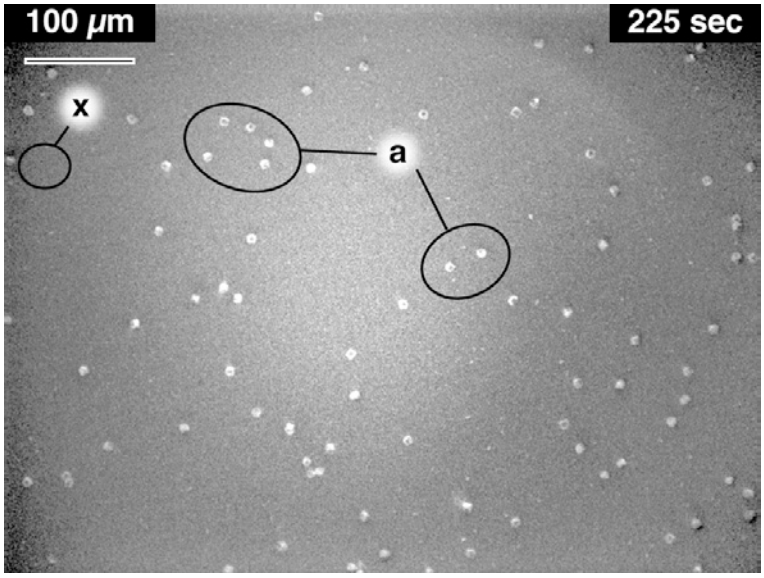

Figure 6-4. Time-lapse picture recorded with the in–situ microscopy set up at 225 s. 'a' calcite growth, 'x' highlights a region where some ACC subsequently lands (see Figure 6-5).

Figure 6-5 shows more clearly the presence of large agglomerates of ACC. Furthermore, comparing the region labelled 'x' in Figure 6-4 and the same

area (also labelled 'x') in Figure 6-5, it is clear that a flock of material has landed on the surface from the solution. As highlighted above, the formation of ACC in solution was proved by focusing the microscope in the solution and moving flocks of ACC in the range of few μm were visualised (pictures not shown). The work of Boltze *et al.* [31] shows that ACC is formed soon after a supersaturated solution is achieved. The work herein, which investigates ACC deposition on the surface, suggests the same mechanism operates.

After the initial instantaneous nucleation of calcite, a new stage of continuous nucleation take place after ~500 s (see regions labelled b from Figure 6-5 to Figure 6-7). This second nucleation stage is attributed to a change in phase from ACC to calcite. ACC has a short-range order as highlighted in the introduction (see section 6-1.1) and there is a slow transformation to a more thermodynamically stable calcite crystal [27, 28]. Fresh ACC is deposited continuously on the surface and continuous formation of new nuclei after ~500 s evidences that the phase change takes place in a continuous fashion.

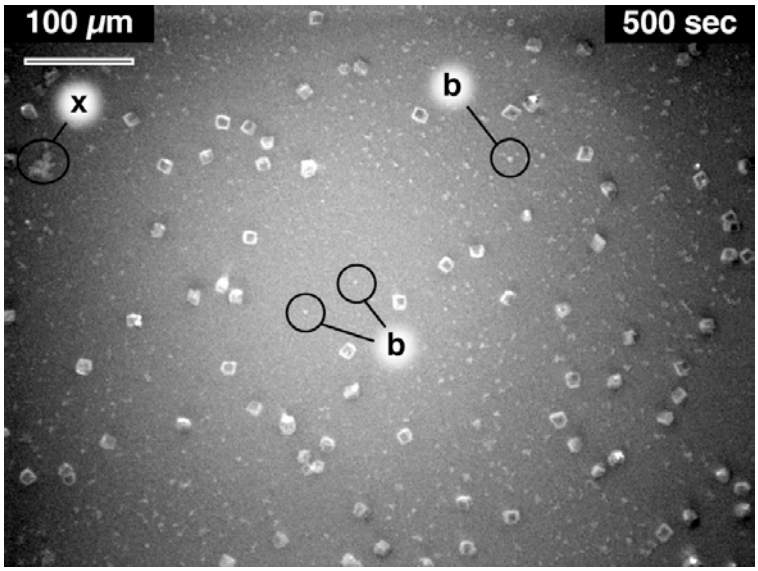

Figure 6-5. Time-lapse picture recorded with the in–situ microscopy set up at 500 s. 'b' phase change nucleation, 'x' landing of a ACC flock.

An interesting observation at later times is evidenced in Figure 6-6 and Figure 6-7 in the regions labelled ‘a’ and ‘c’. The ACC nearby the calcite crystals starts to dissolve. This process is initially quite subtle, but as the crystal size increases, surface depletion of ACC becomes more significant.

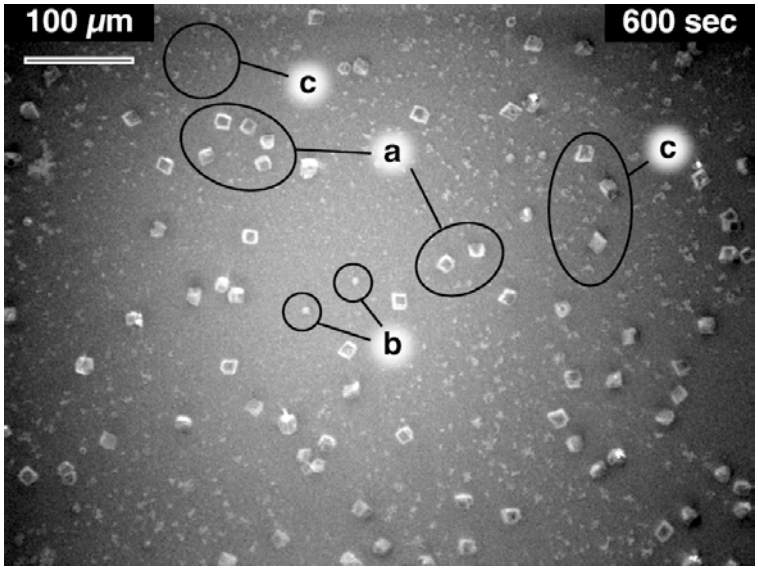

Figure 6-6. Time-lapse picture recorded with the in–situ microscopy set up at 600 s. ‘a, c’ ACC depletion, ‘b’ phase change nucleation.

This phenomenon is particularly interesting because the incoming fresh solution is still highly supersaturated, but is clearly unable to supply enough material to maintain the interface at high-supersaturation. Thus, the saturation level is clearly gradually decreasing due to the growing calcite crystals so that eventually the solution becomes undersaturated with respect the ACC, which drives the dissolution process. The fact that this process is mostly localised to regions where there are calcite crystals indicates there will be strong concentration gradient in these regions. Furthermore, this also means that the growth/dissolution dynamics are, at least partially, transport-controlled. This aspect is considered further below.

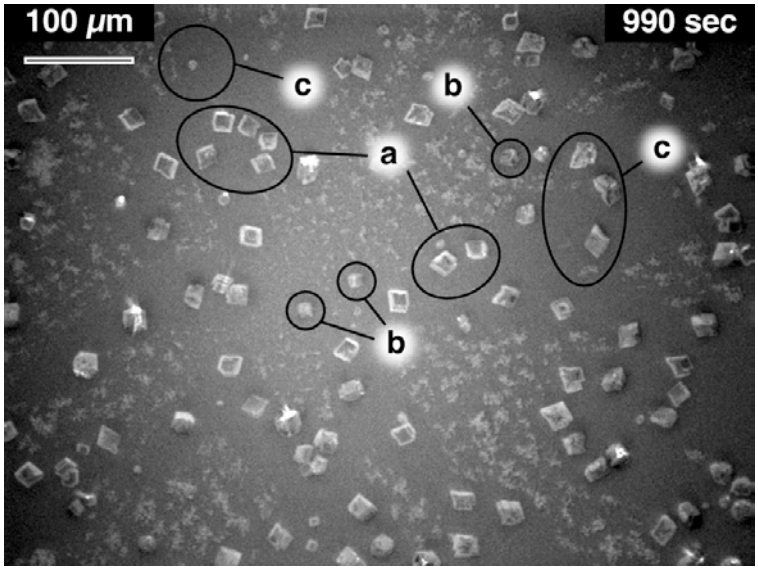

Figure 6-7. Time-lapse picture recorded with the in–situ microscopy set up at 990 s. 'a, c' ACC depletion, 'b' phase change nucleation.

In regions without calcite crystals, the ACC agglomerates were unaffected by this process (Figure 6-7) and the ACC continued to accumulate, indicating that the solution was supersaturated with respect to ACC (and hence calcite). The total absence of ACC close to the calcite crystals gave further important information: the ACC in solution that was approaching the crystal was dissolved before it reached the surface at this stage of the deposition process.

Heterogeneous nucleation and growth of calcite normally occurs on the more stable (104) plane [22], and the calcite crystals formed on the glass surface reproduce this behaviour. The density of calcite crystals formed in the initial nucleation process is 2.3 (±0.2) $x10^4$ crystals per cm. The second nucleation stage only produces a few extra crystals, 6.3 (±2) $x10^3$ crystals cm^{-2}, giving a total of 2.9 (±0.2) $x10^4$ crystals cm^{-2}. To estimate the growth rate, 3 crystals with a well-defined rhombohedric shape and with the (104) plane facing the microscope were chosen. The measurements were made for times greater than 250 s when the crystals were sufficiently large to measure the dimensions with

reasonable precision. The main diagonal (*D*) and the minor (*d*) of each crystal were measured at different times during the growth and the average size of the 3 crystals was used to calculate the total volume. The ratio of *D* over *d* (1.241) was very close to the ideal ratio of the unit cell (Figure 6-8), that is 1.233 (see below), allowing calculation of the volume of the crystals considering an isotropic growth of an ideal crystal.

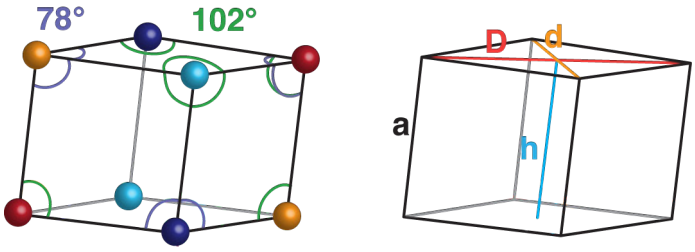

Figure 6-8. Representation of a unit cell of a calcite crystal with an isotropic growth along the {104} planes. In the unit cell only the calcium atoms are reported.

On the unit cell pictured in Figure 6-8 the edges (**a**) measure 4.65 Å, **D** is 9.980 Å, **d** is 8.095 Å and the height or interplanar distance (**h**) is 6.070 Å. The sizes were obtained using crystallographic software (CrystalMaker 7.1, CrystalMaker Software Limited, UK). The volume of the growing crystals was calculated from the relation between the main diagonal (**D**) and the volume of the unit cell and applying this relation to the growing crystal, bearing in mind that the crystals lay on the base and the growth is blocked on that plane. For this reason only half of the volume was considered. The volume of the unit cell was calculated by multiplying the base of the parallepiped by the height (**h**)

$$V = A_b \cdot h \qquad (26)$$

where **V** is the volume of the crystal, $\mathbf{A_b}$ the area of the base. By the relation **D** = **d** / 1.233 the area of the base results

$$A_b = D \bullet d = D \bullet D / 1.233 = \frac{D^2}{1.233} \quad (27)$$

The height (**h**) is related to the edge (**a**) by

$$h = a \cos(\alpha) \quad (28)$$

where **α** (19.135°) is the angle between the edge (**a**) and **h**. The relation between **a** and **D** is then

$$a = \sqrt{\left(\frac{D}{2}\right)^2 \bullet \left(\frac{d}{2}\right)^2} = \sqrt{\left(\frac{D}{2}\right)^2 \bullet \left(\frac{D}{2 \bullet 1.233}\right)^2} = 0.644\ D \quad (29)$$

and **h** results

$$h = a \cos(\alpha) = 0.608\ D \quad (30)$$

The relation between the volume **V** and the main diagonal (**D**) for the unit cell is then

$$V = A_b \bullet h = \frac{D^2}{1.233} \bullet 0.608\ D = 0.4931\ D^3 \quad (31)$$

the volume of the growing crystals was calculated by (31), but only half of the volume was considered since the bottom face lies on the substrate and there is not growth. The actual relation used was $V = D^3$ x0.2466, and the moles per crystal were calculated using the calcite density (2.71 g cm^{-3} [33]). The plot in Figure 6-9 shows the amount of moles intake for the average crystal with time. The plot shows a gradual increase of the gradient with time, until it reaches a constant value of 1.182 (±0.4) $x10^{-13}$ mol sec^{-1}. The fact that this limit is reached is strongly indicative of a strong transport control growth. The total amount of material per crystal after 1000 s was 8.6 (±0.8) $x10^{-11}$ mol.

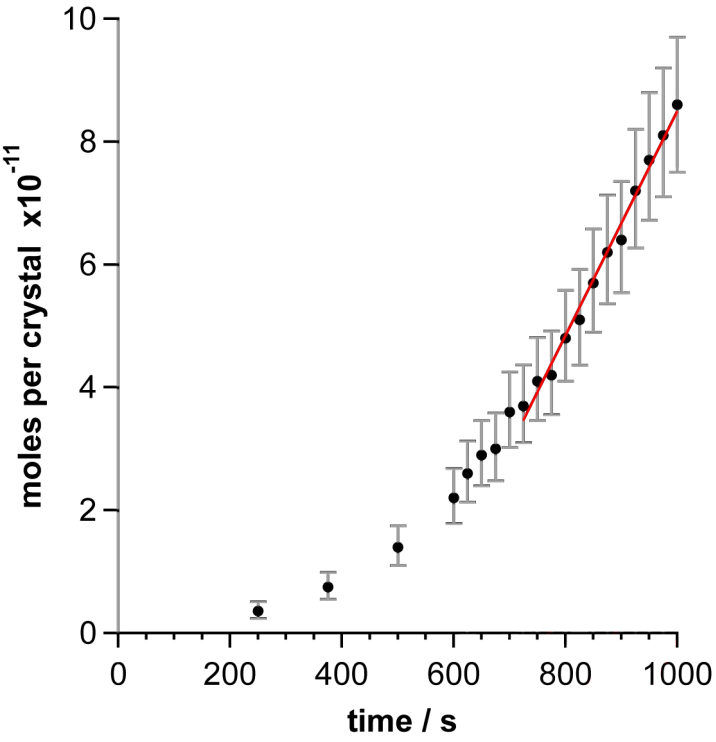

Figure 6-9. Mole intake per crystal with time.

The flux at the substrate can be attained by multiplying the limiting gradient in Figure 6-9 by the crystal density on the glass substrate and it results in 5.31 (±0.04) $x10^{-9}$ mol cm^{-2} s^{-1}.

6.2.2.1 ACC-Calcite Transformation Process

Closer examination of the dissolution process of ACC and its forms was carried out following the previous procedure to deposit calcium carbonate in both forms, as calcite and ACC, on glass substrate. After 725 sec of growth the flow was stopped and time-lapse pictures were recorded to follow the ACC dissolution and calcite growth. Using this procedure the dissolution process is accelerated compared to the previous experiment in which the system was under flow. Without fresh solution flow, calcium and carbonate taken up by the growing calcite crystals are depleted rapidly. When an undersaturated solution with respect ACC is attained dissolution commences, initially close to the

crystals then gradually on the whole surface. Time-lapse pictures (Figure 6-10) show the increase of the cleared area in a circular shape with a calcite crystal at the centre.

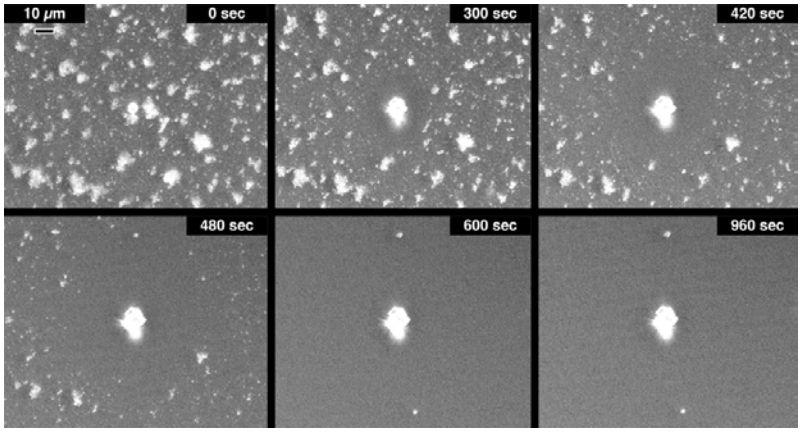

Figure 6-10. Time-lapse pictures recorded with the in–situ microscopy set up. ACC dissolution process for a single growing calcite crystal.

This pattern is typical of a diffusive process to a microscopic object [34]. The transition from individual diffusion fields to overlapped diffusion fields can furthermore be seen when there are two closely spaced crystals (Figure 6-11).

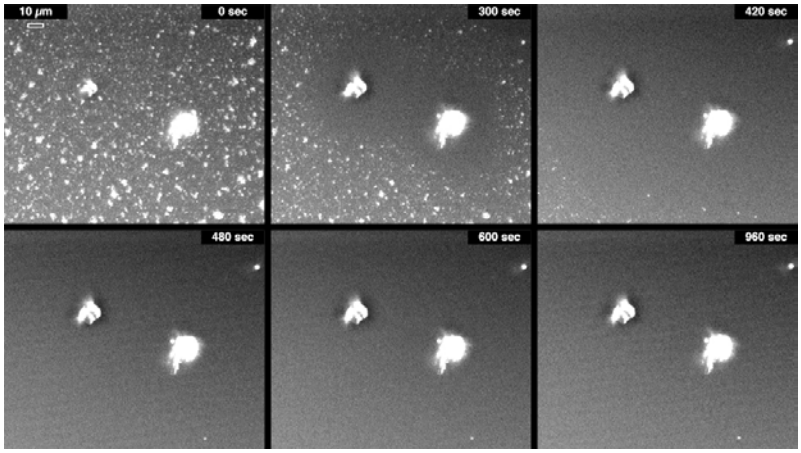

Figure 6-11. Time-lapse pictures recorded with the in–situ microscopy set up, ACC dissolution process in presence of overlap of diffusion field for two closely spaced growing calcite crystals.

Figure 6-12 is a representation of the process identified of both cases with or without flow.

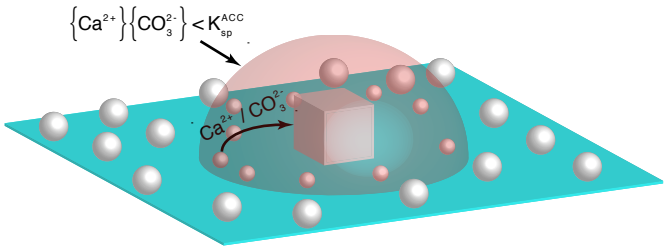

Figure 6-12. Feed process representation.

When ACC starts to dissolve the Ca^{2+} and CO_3^{2-} activity product within the dome boundary illustrated in Figure 6-12 is slightly smaller than K_{sp}^{ACC}, but ~10 times higher than calcite K_{sp}^{cal}. The ACC at the surface, as well as the ACC in solution, under flow, within the hemispherical dome dissolves and supplies material to calcite.

6.2.2.2 *Micro-Raman Characterisation of Surface Deposits*

Figure 6-13 reports a typical Micro-Raman spectrum recorded on glass substrates after calcium carbonate deposition; the beam was focused on a crystal.

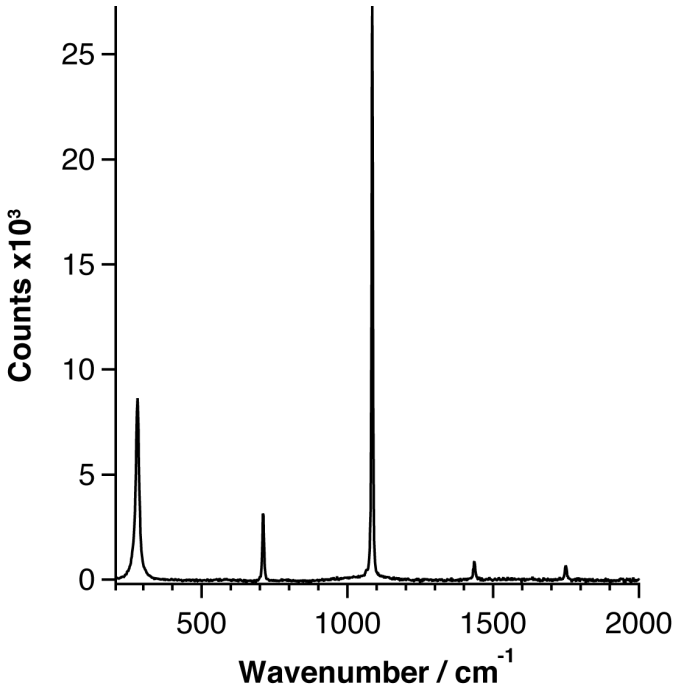

Figure 6-13. Micro-Raman spectrum with the laser beam focused on a calcite crystal on glass substrate after deposition within the optical cell.

In Table 6-3 are reported the peak position of the spectrum recorded and the corresponding literature values [17, 35]. The comparison confirm the presence of pure calcite crystals on the surface of the glass substrate.

Table 6-3. Experimental and tabulated [17, 35] Raman peaks for a calcite crystal.

Experimental peak / cm^{-1}	*Tabulated peak / cm^{-1}*	*Vibration mode*
280	280	Lattice mode
710	710	In plane bending
1086	1086	Symmetric stretching
1435	1435	Symmetric stretching
1749	1749	Overtones

6.2.3 QCM-flow Cell Experiments

The QCM experiments were performed using a similar procedure as for the optical flow experiments (above). The cell was filled with water before the supersaturated solution was diverted into the cell. The change of frequency versus time was recorded and converted to mass using the Sauerbrey equation (see chapter 2) and then to moles of $CaCO_3$ per unit area (probe area was 0.205 cm^2).

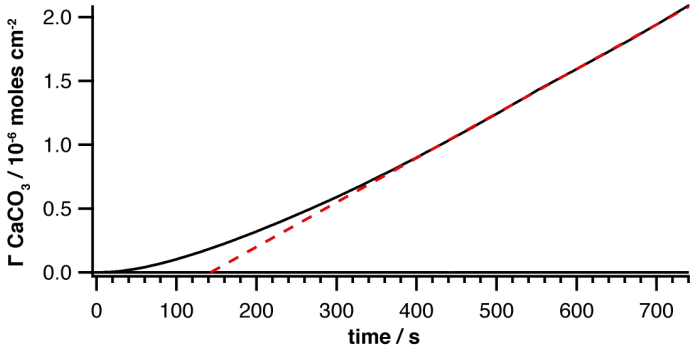

Figure 6-14. Deposition of calcium carbonate, using the QCM flow cell set up, as function of time. The red dashed line shows the behaviour for a constant flux.

The plot in Figure 6-14 shows the amount of $CaCO_3$ (moles cm^{-2}) deposited as function of time. In the initial phase (t <100 s) the overall flux is rather low and an essentially surface-controlled growth take place. However, at longer times a constant flux (dashed red line) is observed, which is consistent with mass transport controlled growth on the gold surface. This situation was reached after ~400 s, and the gradient (3.5 (±0.1) $x10^{-9}$ mole cm^{-2} s^{-1}) is the integral flux at the overall QCM probe surface. As discussed below, this value was used as a fitting parameter to obtain further mechanistic insight through simulations.

The crystal density after the experiment was measured via FE-SEM images (Figure 6-15). The number of crystal per cm^2 underneath the nozzle and at the edge was 2.3 (±0.2) $x10^5$ crystals cm^{-2} and 1.9 (±0.2) $x10^5$ crystals cm^{-2}, respectively. The supersaturation is constant along the substrate during the nucleation; therefore the same initial driving force was experienced over the whole substrate resulting in a uniform nucleation density. Interestingly, there is some evidence of formation of a different crystal polymorph, the area labelled c in Figure 6-15, that were completely absent on the glass surface.

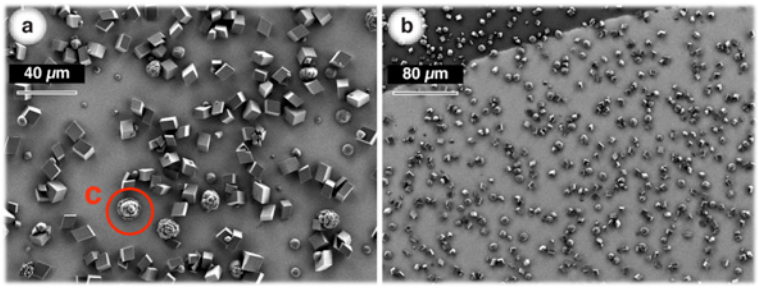

Figure 6-15. FE-SEM images of the QCM crystal after deposition. The images were taken underneath the nozzle outlet (a) and at the edge of the gold coated surface (b). (c) Vaterite crystal.

It is important to point out that although the crystal density is uniform across the surface there is a significant variation in size with those at the edge being smaller. An estimation of the mass deposited at the position directly underneath the nozzle and at the edge of the probe were calculated using the same procedure used for the in–situ optical experiment. Values of 1.5 (±0.2) x10^{-6} mol cm^{-2} and 2.5 (±0.2) x10^{-7} mol cm^{-2} were found. The value underneath the nozzle is higher compared to the microscopy experiment, but it can be explained easily since due to a higher crystal density the maximum constant flux (mass transport growth) was reached earlier and the total mass deposited was expected to be higher.

6.2.4 Simulation Model

The optical and QCM-flow cells were designed to have the same geometry to obtain the same fluid flow profile at the deposition surface. Figure 6-16a shows the geometry of the cell and the boundaries chosen (solid line) to define the boundary conditions employed for the numerical simulations, which solved the incompressible stationary Navier–Stokes equation for the flow in the ***r*** and ***z*** directions in the whole domain. On boundary **a**, that represents the nozzle inlet, a parabolic flow was imposed (32), the length of the nozzle was sufficient to reach a parabolic velocity profile before the outlet of the nozzle,

$$v(r) = -\frac{2V_f}{\pi}\left(r_{in} - r^2\right) \qquad (32)$$

where V_f is the volume flow rate of the solution, r_{in} (0.75 mm) is the inner radius of the nozzle and r the radial coordinate. The boundaries **b**, **c**, **d** and **e** are defined as ‘no slip’; an axial symmetry was defined along **f**.

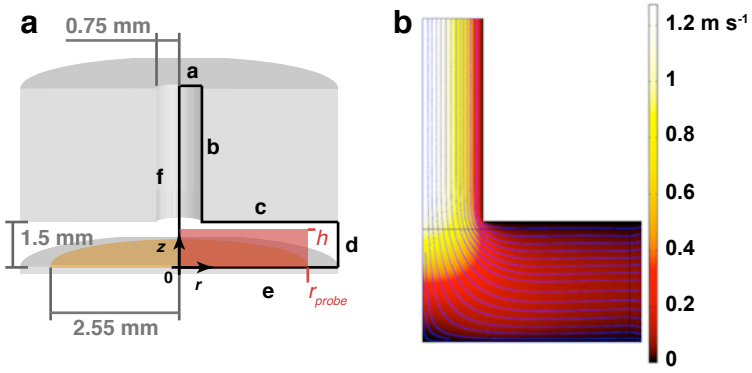

Figure 6-16. (a) Cell geometry and (b) velocity profile related to area within the black solid line.

Figure 6-16b shows the resulting solution flow (for $V_f = 2$ ml min^{-1}), highlighting a well-defined laminar flow in the whole domain. The velocities u and v, were used as the convective terms in the convection-diffusion part of the model which was solved on the red square in Figure 6-16a (encompassing the region where there were concentration gradients). The steady-state convection-diffusion equation was solved for the concentration (Figure 6-17a) of a single species, c, with the following boundary conditions applied; axial symmetry along $r = 0$, bulk concentration at $z = h$ (1.4 mm), a convective flux at $r = r_{probe}$ (2.55 mm) and concentration (c) equal to zero at $z = 0$ (the QCM probe boundary), in order to evaluate the transport-controlled flux. The numerical simulations were performed using commercial finite element software (Comsol Multiphysics 3.4, Comsol AB, Sweden) interfaced with Matlab (Matlab Release 2008a, MathWorks Inc., Cambridge, UK). The final mesh size employed was chosen to be sufficiently fine, such that further refinement did not give any significant change on the final concentration distribution.

In the experiments carried out, carbonate was the limiting species (total [carbonate] < [calcium]). Under mass transport-controlled growth at the surface of the crystals S = 1. This situation was simulated evaluating all the equilibria

involved during the deposition of a solid phase (calcite), when a solution with S = 1 was attained the activity of free CO_3^{2-} {1.065 x10^{-6}} was three order of magnitude lower then the free Ca^{2+} {3.149 x10^{-3}}. With these conditions fulfilled it is reasonable to consider the activity of free CO_3^{2-} (*c*) equal to zero at the surface of the crystals.

The concentration distribution of the free carbonate ions (Figure 6-17a) was used by the software to calculate the flux profile (Figure 6-17b) and the integral flux of CO_3^{2-} at the probe surface; the concentration (*c*) was then evaluated to obtain a total integral flux equal to the experimental value calculated with the QCM experiment (3.5 x10^{-9} ±0.1 x10^{-9} mol cm^{-2} s^{-1}) at mass transport-controlled growth condition. A concentration of 2.9 mM of the CO_3^{2-} in the bulk solution was necessary to attain such total integral flux.

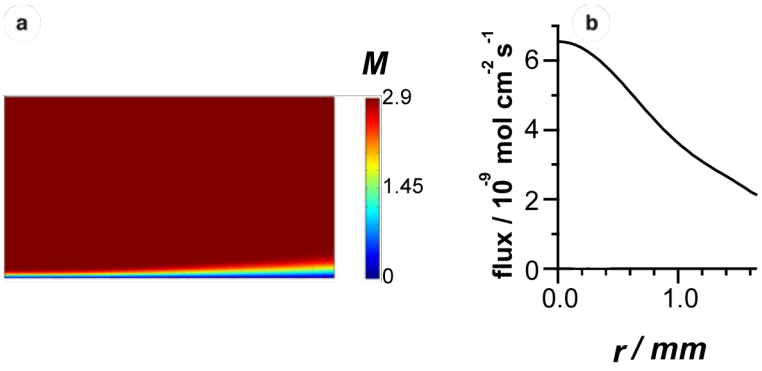

Figure 6-17. (a) Concentration distribution (in the region highlighted in Figure 6-16a) and (b) flux profile of the limiting species at the surface of the QCM probe.

In Table 6-4 are summarised the fluxes calculated experimentally via QCM and in–situ microscopy experiments, and the value calculated by simulation.

Table 6-4. Experimental and simulated flux and amount of calcite deposited.

	QCM experiment	*In–situ optic experiment*	*Simulation*
Average over the whole surface			
Flux [moles cm^{-2} s^{-1}]	3.5 (±0.1) $x10^{-9}$		3.5 $x10^{-9}$
Deposition [moles cm^{-2}]	2.1 (±0.1) $x10^{-6}$		2.8 $x10^{-6}$
Underneath the nozzle			
Flux [moles cm^{-2} s^{-1}]		5.31 (±0.04) $x10^{-9}$	6.6 $x10^{-9}$

The total calcium carbonate deposited, as measured with QCM, resulted in a lower value than the simulated, which considered a mass transport controlled growth during the whole deposition process. This is because the experimental deposition has a mixed behaviour, an initial surface controlled growth; and later a mass transport controlled growth. The average flux obtained by the in–situ microscopy is lower than the simulated; the simulation considers a situation in which all diffusion fields of each crystal are overlapped, in such a way as to have a planar diffusion towards the substrate. This situation is likely to occur for the QCM experiment in which the crystal density is really high, but in the case of the in–situ optical experiment in which the crystal density is 10 times lower this situation may not be satisfied.

The most important outcome of the simulation is that the bulk activity of the limiting species is 2.99 mM. The activity of the free carbonate ions is much lower (0.473 $x10^{-3}$) and it would not supply enough ions to sustain such flux. The only species in solution with a comparable activity is the calcium carbonate ion pair ($\{CaCO_3^{aq}\}$ = 2.61 $x10^{-3}$). This supports a process in which the addition of ions to a growing crystal is by ion pair addition [36].

6.3 Conclusions

The difference in the crystal density on the two different substrates, gold and glass, evidenced a higher affinity or lower heterogeneous nucleation energy barrier on the gold surface and that the formation of different polymorphs of calcium carbonate is promoted by the gold surface.

The systems set up gave the opportunity to investigate the processes of calcium carbonate deposition at high-supersaturation, which showed the influence of the ACC during the growth of calcite on the surface. Significantly, the in–situ microscopy experiment evidenced how the ACC serves as material storage during the initial phase of the deposition and afterwards, when the solution is not able to support the growing crystals, it dissolves thereby, supplying more material to the calcite crystals.

Dissolution of ACC is an extremely fast process. From the in–situ experiment, after the appearance of the undersaturated zone around the crystals, no further deposition of ACC is recognised on that area. The ACC formed in solution dissolved as soon it reaches the undersaturated interfacial region.

The QCM experiment proved to be a very powerful tool to obtain quantitative measurements of the scaling process, and it gave an indication that the addition of material to a growing crystal may be in ion pairs instead of single ions.

While the modelling provided very useful insight, it could be further developed in order to take into account the multiple equilibria. Moreover, to simulate a real system it is important to include the effect of the crystal size and density on the average flux over the surface.

6.4 Bibliography

[1] Mann, S.; Didymus, J. M.; Sanderson, N. P.; Heywood, B. R.; Samper, E. J. A.; *J. Chem. Soc. Faraday Trans.* **1990**, *86*, 1873-1880.

[2] Berman, A.; Addadi, L.; Weiner, S.; *Nature* **1988**, *331*, 546-548.

[3] Falini, G.; Albeck, S.; Weiner, S.; Addadi, L.; *Science* **1996**, *271*, 67.

[4] Spanos, N.; Koutsoukos, P. G.; *J. Phys. Chem. B* **1998**, *102*, 6679-6684.

[5] Tai, C. Y.; Chien, W. C.; Chen, C. Y.; *AIChE J.* **1999**, *45*, 1605-1614.

[6] Qingfeng, Y.; Yangqiao, L.; Anzhong, G.; Jie, D.; Ziqiu, S.; *J. Colloid. Interface Sci.* **2001**, *240*, 608-621.

[7] Hadicke, E.; Rieger, J.; Rau, I. U.; Boeckh, D.; *Phys. Chem. Chem. Phys.* **1999**, *1*, 3891-3898.

[8] Westin, K. J.; Rasmuson, A. C.; *J. Colloid. Interface Sci.* **2005**, *282*, 359-369.

[9] Wada, N.; Kanamura, K.; Umegaku, T.; *J. Colloid. Interface Sci.* **2001**, *233*, 65-72.

[10] Devos, O.; Gabrielli, C.; Tlili, M.; Tribollet, B.; *J. Electrochem. Soc.* **2003**, *150*, C494-C501.

[11] Mann, S.; *Nature* **1988**, *332*, 119-124.

[12] Faatz, M.; Grohn, F.; Wegner, W.; *Adv. Mater.* **2004**, *16*, 996-1000.

[13] Aizenberga, J.; Lambert, G.; Addadi, L.; Weiner, S.; *Adv. Mater.* **1996**, *8*, 222-226.

[14] Kulak, A. N.; Iddon, P.; Li, Y.; Armes, S. P.; Cölfen, H.; Paris, O.; Wilson, R. M.; Meldrum, F. C.; *JACS* **2007**, *129*, 3729-3736.

[15] Wucher, B.; Yue, W.; Kulak, A. N.; Meldrum, F. C.; *Chem. Mater.* **2007**, *19*, 1111-1119.

[16] Meldrum, F. C. and Coelfen, H. *Chemical Reviews*. **2008**, 108, 4332-4432.

[17] Gabrielli, C.; Jaouhari, R.; Joiret, S.; and Maurin, G. J. *Raman Spectrosc.* **2000**, 31, 497-502.

[18] Peric, J.; Vucak, M.; Krstulovic, R.; Brecevic, L. j.; Kralj, D.; *Thermochim. Acta* **1996**, *277*, 175-186.

[19] Teng, H. H.; Dove, P. M.; Orme, C. A.; De Yoreo, J. J.; *Science* **1998**, *282*, 724.

[20] Teng, H. H.; Dove, P. M.; De Yoreo, J. J.; *Geochim. Cosmchim. Acta* **2000**, *64*, 2255-2266.

[21] Teng, H. H.; Dove, P. M.; DeYoreo, J. J.; *Geochim. Cosmchim. Acta* **1999**, *63*, 2507-2512.

[22] Dobson, P. S.; Bindley, L. A.; Macpherson, J. V.; Unwin, P. R.; *Langmuir* **2005**, *21*, 1255-1260.

[23] Kwon, Y. I.; Dai, B.; Derby, J. J.; *Prog. Cryst. Growth and Charact. Mater.* **2007**, *53*, 167-206.

[24] Gebauer, D.; Völkel, A.; Cölfen, H.; *Science* **2008**, *322*, 1819-1822.

[25] Liu, J.; Rieger, J.; Huber, K.; *Langmuir* **2008**, *24*, 8262-8271.

[26] Rieger, J.; Frechen, T.; Cox, G.; Heckmann, W.; Schmidt, C.; Thieme, J.; *Faraday Discuss.* **2007**, *136*, 265-277.

[27] Lam, R. S. K.; Charnock, J. M.; Lennie, A.; Meldrum, F. C.; *CrystEngComm* **2007**, *9*, 1226-1236.

[28] Michel, F. M.; MacDonald, J.; Feng, J.; Phillips, B. L.; Ehm, L.; Tarabrella, C.; Parise, J. B.; Reeder, R. J.; *Chem. Mater.* **2008**, *20*, 4720-4728.

[29] Rodriguez-Blanco, J. D.; Shaw, S.; Benning, L. G.; *Mineral. Mag.* **2008**, *72*, 283-286.

[30] Rieger, J.; Thieme, J.; Schmidt, C.; *Langmuir* **2000**, *16*, 8300-8305.

[31] Bolze, J.; Peng, B.; Dingenouts, N.; Panine, P.; Narayanan, T.; Ballauff, M.; *Langmuir* **2002**, *18*, 8364-8369.

[32] Niel Plummer, L.; Busenberg, E.; *Geochim. Cosmchim. Acta* **1982**, *46*, 1011-1040.

[33] Lide, D. R.; others, O.; *CRC Handbook of Chemistry and Physics, 1998-1999*; CRC Press: 1998.

[34] Bard, A. J.; Faulkner, L. R.; *Electrochemical methods: fundamentals and applications* , 2nd ed.; John Wiley & Sons, Inc.: United States of America, 2001.

[35] Rutt, H. N.; Nicola, J. H.; *J. Phys. C: Solid State Phys.* **1974**, 4522.

[36] Gal, J. -Y.; Bollinger, J. -C.; Tolosa, H.; Gache, N.; *Talanta* **1996**, *43*, 1497-1509.

Chapter 7 Influence of Citrate on the Deposition of Calcium Carbonate on Foreign Surfaces

This chapter considers the influence of citrate concentration on the deposition of calcium carbonate at high–supersaturated (scaling) conditions on a gold surface. The investigation was carried out employing a QCM-flow cell (see chapters 2 and 6) to evaluate quantitatively the amount of calcium carbonate deposited in real time. In–situ microscopy experiments –with a glass substrate– were used to obtain further insight of the effect of citrate on the stabilisation of ACC at interfaces and in solution. A significant finding is that calcium carbonate deposition at high supersaturation shows a non–monotonic behaviour of the amount of scaling deposited with the citrate (CIT) concentration. The reasons for this are shown to be the interplay of CIT with the different polymorphs of calcium carbonate during the surface scaling process.

7.1 Introduction

As already highlighted in the previous chapter, calcium carbonate presents a number of polymorphs: calcite, aragonite and vaterite are dehydrated forms and more thermodynamically stable than the hexa and mono–hydrate polymorphs and that can be only obtained in particular conditions, such as at low temperature, high precipitation rate and in the presence of specific additives [1-3]. A non–crystalline form of calcium carbonate is also found; ACC is described as an agglomeration of calcium carbonate nanoparticles, which are formed via homogeneous nucleation under high supersaturation conditions, in which kinetics prevail over thermodynamic effects. Both Liu *et al*. [4] and Bolze *et al.* [5] have reported on the nucleation stage of ACC using cryo-TEM techniques and SAXS, respectively. It has been shown that the formation of ACC nanoparticles is an incredibly fast process, and the nanoparticles agglomerate to form flocks of ACC from a few microns to hundreds of microns in range depending on the experimental conditions. Innovative recent work by Gebauer *et al*. [6] reported the formation of stable clusters of $CaCO_3$ as a precursor for ACC formation, while Rieger *et al.* [7, 8] identified ACC as having a core with short-range structure that expanded if the ACC was kept in a high supersaturated environment. This eventually formed a crystalline nucleus of a dehydrated polymorph, calcite or vaterite.

The above considerations indicate that ACC is likely to be a highly significant initial stage for other polymorphs. ACC is a highly unstable and upon decreasing the supersaturation it quickly dissolves in favour of more thermodynamically stable calcium carbonate crystalline forms [2]. ACC is used in nature as a building block to create complex morphological structures as in the

Ascidian Skeleton [9] or simply to provide calcium and carbonate storage [10] for further use. Due to its transient nature it is stabilised by biological organisms via proteins or macromolecules [11, 12]. Moulding of the growth of calcium carbonate from the nanometer to micrometer range allows biological systems to produce materials with unusual strength properties as in shells or in exo/endoskeleton on a variety of organisms [13]. A common aim in material science is to mimic biomineralization, and a key step is to understand the stabilising properties of macromolecules or polymers on the formation of ACC [14, 15].

A related branch of science concerns understanding in the formation of scale and scale incrustation, and particularly its inhibition, which is of major relevance in many industrial processes involving water and its treatment. Decades of investigation have sought to identify the inhibitory properties of different molecules that range from small inorganic chelants for metal ions to polymers [16, 17] that may, for example: sequester calcium ions and reduce the supersaturation; affect the growth of crystals by interacting with their surfaces; or be incorporated within crystals, influencing their morphology [18-23]. Among these, CIT is commonly used as calcium carbonate growth inhibitor [22, 23] and shows a monotonic inhibitory effect.

Previous investigations with QCM have evaluated the scaling power of carbonate water with and without additives [24, 15]. Several such studies have been carried out at electrode surfaces, using the reduction of the O_2 at the surface of a gold coated quartz crystal to induce a local increase of the pH and hence an increase of the supersaturation, the deposition of $CaCO_3$ at the surface that can be monitored by the QCM [26, 27]. However, in this deposition protocol a

supersaturated solution is only obtained close to the substrate and may not be relevant to situations where the bulk solution is supersaturated, as commonly encountered in industrial applications.

Related studies of the growth of single faces of a crystal employing AFM [28] or optical microscopy [22] have demonstrated the inhibitory effect of additives at low supersaturated condition, showing –for example– how step morphology is altered. In contrast in this chapter, the focus is on the scaling process at high supersaturation, which is more applicable in real systems. To obtain a better understanding of the role of additives the whole process has to be considered, inducing the ACC nucleation at high supersaturation as well as the heterogeneous nucleation under well-defined condition of chemical speciation and flow. The aim of the work presented here is to understand the effect on scaling inhibition of CIT, which is one of the most common additives employed practically. The studies herein exploit the QCM and optical microscopy investigations in a flow system that allowed a well-defined flow of a solution with a constant supersaturation (as described in the previous chapter).

7.2 Experimental

7.2.1 Solution preparation

Solutions containing calcium ions at a concentration of 20 mM with different concentrations of CIT (1, 2, 3.5, 5 and 7 mM) were prepared by dissolving $CaCl_2$ xH_2O and NaH_2Citrate in Milli-Q reagent water. NaOH (1 M) was added to adjust the pH to 10.50 ±0.05. The carbonate solutions (10 mM)

were prepared by dissolving $NaHCO_3$ and the pH was adjusted to 10.50 ±0.05 with NaOH (1 M). Note that the CIT was added to the calcium ion-containing solution to favour complexation of calcium ions by CIT; at equilibrium, after mixing the two solutions (calcium/CIT and carbonate), simulations (Table 7-2) showed that at least 97% of the CIT was bound to calcium ions. The solutions were prepared as quickly as possible and the two syringes of the syringe pump (see Chapter 2) were filled as quickly as possible to reduce exchange of CO_2 and satisfying the assumption of a close system (see Chapter 2). The solution pH after each step of preparation was measured to compare experimental values with calculated ones (under the closed system model) and satisfactory agreement was found (Table 7-1).

Table 7-1. Experimental and simulated pH and NaOH (1 M) added for the various solutions and the value of NaOH added to 100 ml of solution.

Solution	*Experimental*		*Simulated*	
	pH	*NaOH added / µl*	*pH*	*NaOH added / µl*
Milli-Q water	5.60 ±0.05		5.60	
Carbonate	10.50 ±0.05	710 ±10	10.50	700
Ca/CIT 1 mM	10.53 ±0.05	302 ±10	10.50	300
Ca/CIT 2 mM	10.49 ±0.05	598 ±10	10.50	600
Ca/CIT 3.5 mM	10.49 ±0.05	995 ±10	10.50	1000
Ca/CIT 5 mM	10.49 ±0.05	1496 ±10	10.50	1500
Ca/CIT 7 mM	10.50 ±0.05	2101 ±10	10.50	2100

The speciation of the solution delivered to the QCM-flow cell and the optical flow cell are listed in Table 7-2; the speciation was calculated via speciation software, as explained in Chapter 2.

Table 7-2. Activity of the relevant species in solution after mixing.

[CIT]	*Blank*	*0.5 mM*	*1 mM*	*1.75 mM*	*2.5 mM*	*3.5 mM*
pH	9.99	10.13	10.34	10.63	11.08	11.3
$\{Ca^{2+}\}$ / M	3.74×10^{-3}	3.44×10^{-3}	3.11×10^{-3}	2.71×10^{-3}	2.33×10^{-3}	1.93×10^{-3}
$\{CaCIT^{-}\}$ / M		0.417×10^{-3}	0.831×10^{-3}	1.45×10^{-3}	2.05×10^{-3}	2.85×10^{-3}
$\{CIT^{3-}\}$ / M		1.58×10^{-6}	3.49×10^{-6}	6.99×10^{-6}	1.15×10^{-5}	1.93×10^{-5}
$\{CO_3^{2-}\}$ / M	0.473×10^{-3}	0.531×10^{-3}	0.627×10^{-3}	0.720×10^{-3}	0.827×10^{-3}	0.919×10^{-3}
S (calcite)	22.7	23.1	23.8	23.8	23.7	22.7

7.3 Results and Discussion

7.3.1 QCM Investigations

These measurements were performed to understand quantitatively the influence of CIT during the deposition of $CaCO_3$ on a gold surface. A set of chronogravimetric curves, shown in Figure 7-1 represents $CaCO_3$ deposited using as growth medium a supersaturated solution of calcium carbonate with the same *S* of ~23.5 but with different final concentrations of CIT (0.5, 1, 1.75, 2.5 and 3.5 mM). As might be expected, based on its known inhibitory properties, the addition of CIT resulted in a smaller amount of deposition on the surface, with respect to the blank experiment containing no CIT (Figure 7-1 '**f**'). However, it is striking that the amount of $CaCO_3$ deposited did not follow a monotonic behaviour with CIT concentration. As the concentration of CIT was increased from 0.5 to 1.75 mM, there was a clearly steady and significant increase in the rate at which $CaCO_3$ was deposited. Although, with further

increase of the CIT concentration (2.5 and 3.5 mM), there was a decrease of mass deposited.

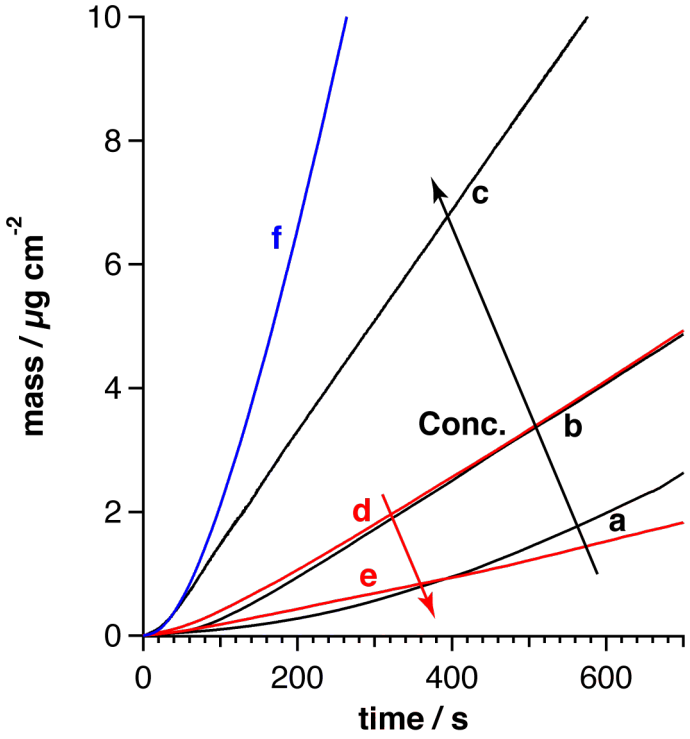

Figure 7-1. Chronogravimetric curves of delivered solution containing 0.5 'a', 1, 'b' 1.75 'c', 2.5 'd' and 3.5 mM 'e' of CIT; 'f' control experiment without CIT.

FE-SEM images are presented in Figure 7-2 at relatively low magnification, so as to show a wide area of the QCM crystal surfaces in the region directly underneath the nozzle inlet. The blank experiment shows the formation of a uniform deposition of calcite and few vaterite crystals, while there is no evidence of ACC, for the reasons already discussed in the previous chapter. Interestingly, deposition in presence of CIT shows the total absence of calcite crystals and the formation of ACC in the form of a film of NP aggregates whose morphology depends on the CIT concentration. At low concentration of CIT (0.5 mM) it is possible to see the formation of strips of material on the surface that follow the flow streamlines (Figure 7-2). At higher magnification (Figure

7-3) it is possible to see the NPs aggregates have a preferential direction along the flow, certainly in the CIT concentration range of 0.5–2.5 mM this would appear to be consistent with the idea that there is deposition from the solution of the NPs which aggregate during the growth of the film, an aspect discussed in the next section. By increasing the concentration of CIT, the deposition over the surface becomes more uniform (Figure 7-2) and at a concentration higher then 1.75 mM the amount of ACC NPs aggregates deposited decreases notably in size and amount (Figure 7-3).

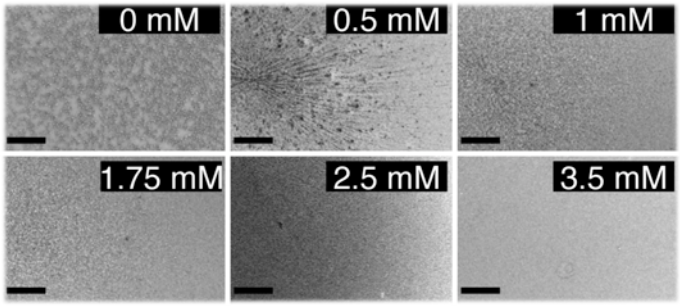

Figure 7-2: FE-SEM images (scale bar 200 µm) of QCM crystals after deposition for 800 s with different concentration of CIT.

As proposed herein by evaluation of the Raman data (see below), CIT is considered a constituent of the ACC NPs. It appears to stabilise ACC NPs formed at low concentrations as shown in Figure 7-3, while preventing formation of calcite.

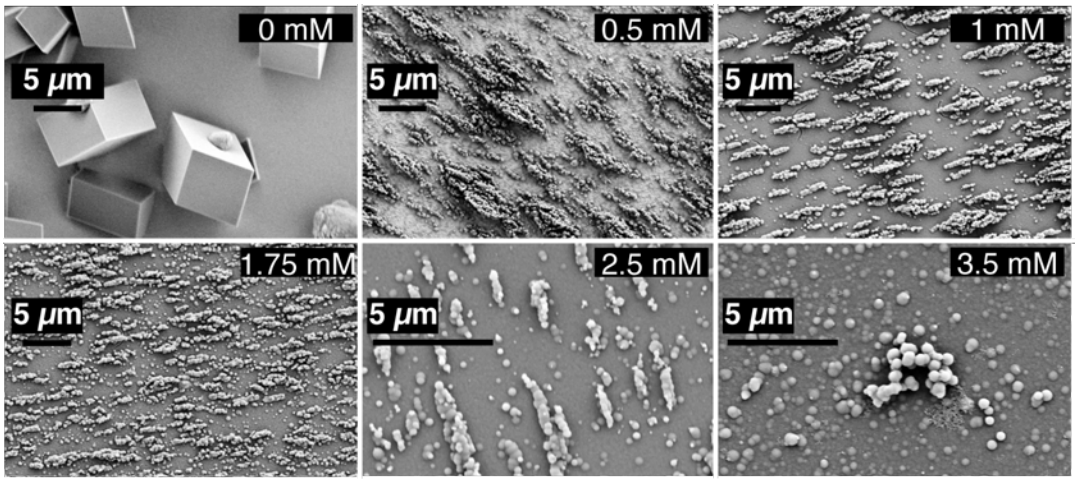

Figure 7-3. FE-SEM images of QCM crystals after deposition for 800 s with different concentration of CIT.

Interestingly, this is consistent with prior studies where the seeded growth in solution was little influenced by CIT [16], but CIT significantly inhibits growth in unseeded experiments [20, 29]. Calcite normally forms by heterogeneous nucleation or a phase change (as highlighted in the previous chapter). The work here shows that this phase change does not take place because the ACC is stabilised by the CIT.

7.3.2 In–Situ Microscopy

This evidenced a similar course as the QCM investigations, namely an initial increase of deposition of ACC NPs followed by diminution with further increase in the CIT concentration. With the in–situ microscopy setup it was possible to follow the deposition of ACC nanoparticle agglomerates formed in solution and eventually deposited on the glass surface. As shown in Figure 7-5 (and on the movies in the CD attached to the thesis) by increasing the concentration of CIT from 0.5 to 1.75 mM, there was actually an increment of ACC deposited on the surface, followed by a decrease when the CIT

concentration rose from 1.75 to 3.5 mM, where ACC deposition on the surface was no longer recognised. The initial increase of the NP agglomerates is related to a stabilisation effect of the CIT, but as shown in the QCM experiments at higher CIT concentration the formation of NPs decreased drastically. This effect is not related to a decrease of *S*, because the supersaturation is constant for all the CIT concentrations, but it is related to a destabilisation of the ACC.

While in the QCM experiments the surface was gold and the ACC formed a film; the substrate for the in–situ optical microscopy experiments was glass and the ACC did not form a film at the surface. Even a gentle flow of water at the end of the experiment rinsed away almost all the ACC from the surface, and only a few agglomerates were detectable by FE-SEM imaging. For example, Figure 7-4 shows the glass substrate for deposition with 0.5 mM CIT; these flocks were used to record Raman spectra.

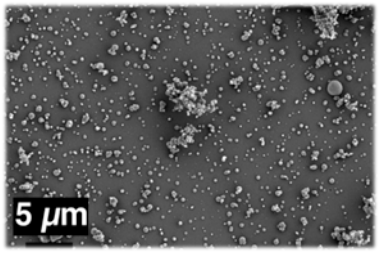

Figure 7-4. FE-SEM image of a glass substrate after deposition of calcium carbonate for 990 s with 0.5 mM CIT.

An interesting aspect of Figure 7-5 is that although a small amount of ACC is formed during the deposition without CIT, as expected at high supersaturation [7] calcite crystals are also formed and during the experiments the ACC deposited starts to dissolve in favour of calcite crystal (as found in the previous chapter). The ACC dissolved completely during the rinsing procedure.

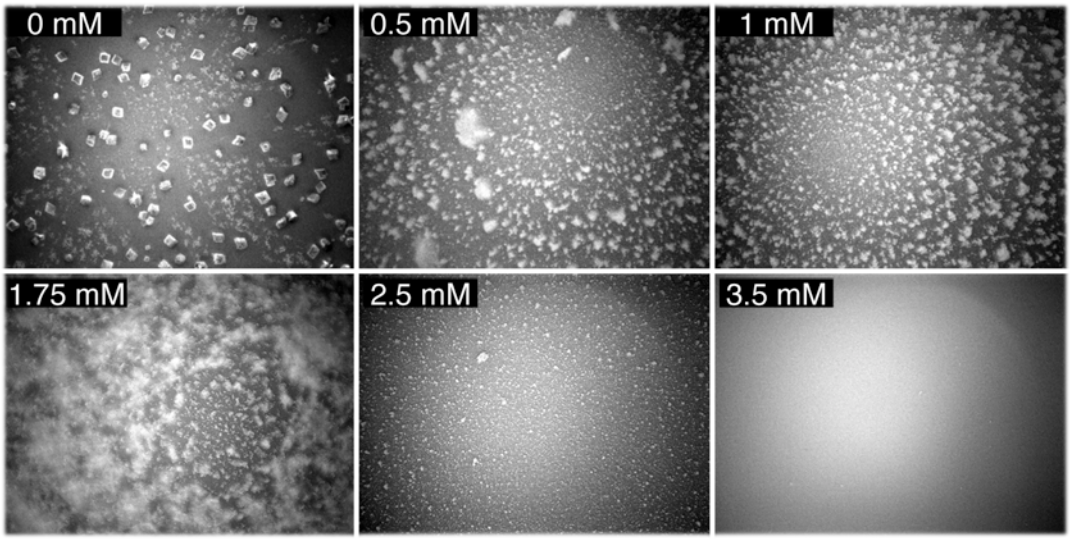

Figure 7-5. Images from in–situ microscopy after 990 s (699x525 µm) of deposition from solutions at different concentration of CIT (images captured from movies attached to the thesis).

7.3.3 Micro-Raman Spectroscopy

The spectra in Figure 7-6 are for samples deposited without additive (red line), where well-defined features of calcite are revealed (see chapter 6). Increasing the concentration of CIT from 0.5 to 1.75 mM (black solid and dashed lines, respectively) results in the main Raman band at 1086 cm^{-1} (carbonate symmetric stretching peak) broadening and it becomes indistinguishable at higher concentration (2.5 mM and 3.5 mM) of CIT (spectrum not shown).

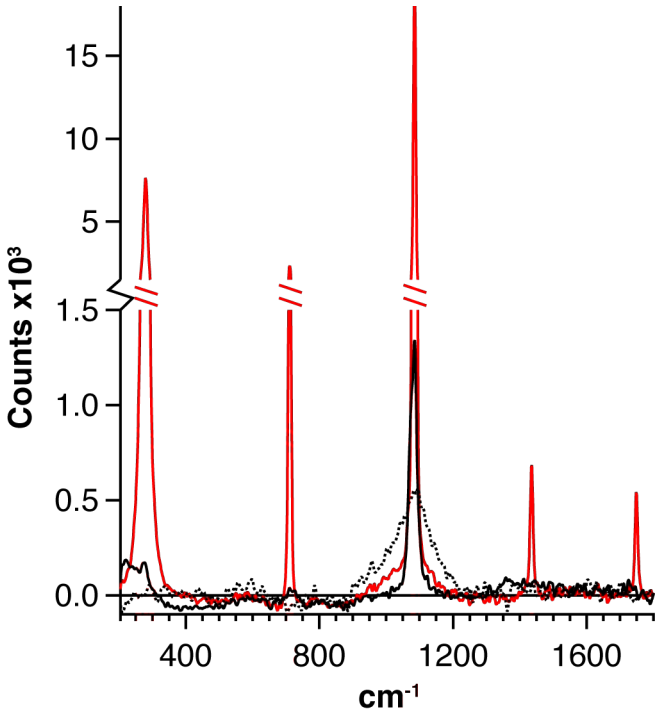

Figure 7-6. Raman spectra of calcium carbonate deposited on glass in the presence of different concentration of CIT: red solid line without; black solid line 0.5 mM and black dotted line 1.75 mM CIT.

ACC has short-range crystal domains [30] which is revealed by a Raman peak related to the symmetric stretching (the others peaks are almost suppressed) [31], which gives an insight into the crystalline order. By increasing the concentration of CIT in solution, it can be seen that this peak broadens, indicating an increase of disorder in the crystal structure of the deposited material. It is likely that CIT is a constituent of the ACC NPs, as stated by Phillips *et al.* [32] for different organic addictives. A broadening of the peak is also indicative of more stable ACC [33].

7.4 Conclusions

We have demonstrated that the concentration of an organic additive (CIT) plays a major role in controlling the quantity of calcium carbonate deposited on a gold surface, but that the scaling of surfaces is not monotonically dependent on the concentration of the CIT at a constant supersaturation ratio. In the case of highly supersaturated solution, the nucleation and growth in solution (enhanced or inhibited by the CIT) influences the overall deposition on the substrate resulting in a non–proportional inhibitory effect with the concentration of the additive. The in–situ optical experiments highlighted that the stabilisation of ACC by CIT has a maximum at a particular concentration range. This stabilising effect and how the ratio between all the components needs to be investigated to obtain a deeper insight of the role of the CIT on the stabilisation of $CaCO_3$.

The experiments carried out on different substrates (gold and glass) evidenced a higher affinity of amorphous calcium carbonate stabilised by the CIT for the gold compared to glass. In fact stabilised ACC formed a stable film on gold, while on glass the majority of the ACC NP aggregates deposited on the surface were easily washed away with a gentle flow of water.

Further work focused on the mechanisms of the nucleation and growth of stabilised ACC in solution is of paramount importance to understand how these processes influence the deposition on a surface at high-supersaturation.

7.5 Bibliography

[1] Clarkson, J. R.; Price, T. J.; Adams, C. J.; *J. Chem. Soc. Faraday Trans.* **1992**, *88*, 243-249.

[2] Brecevic, L.; Nielsen, A. E.; *J. Cryst. Growth* **1989**, *98*, 504-510.

[3] Koga, N.; Nakagoe, Y.; Tanaka, H.; *Thermochim. Acta* **1998**, *318*, 239-244.

[4] Liu, J.; Rieger, J.; Huber, K.; *Langmuir* **2008**, *24*, 8262-8271.

[5] Bolze, J.; Peng, B.; Dingenouts, N.; Panine, P.; Narayanan, T.; Ballauff, M.; *Langmuir* **2002**, *18*, 8364-8369.

[6] Gebauer, D.; Völkel, A.; Cölfen, H.; *Science* **2008**, *322*, 1819-1822.

[7] Rieger, J.; Thieme, J.; Schmidt, C.; *Langmuir* **2000**, *16*, 8300-8305.

[8] Rieger, J.; Frechen, T.; Cox, G.; Heckmann, W.; Schmidt, C.; Thieme, J.; *Faraday Discuss.* **2007**, *136*, 265-277.

[9] Aizenberg, J.; Lambert, G.; Weiner, S.; Addadi, L.; *JACS* **2002**, *124*, 32-39.

[10] Politi, Y.; Levi-Kalisman, Y.; Raz, S.; Wilt, F.; Addadi, L.; Weinr, S.; Sagi, I.; *Adv. Funct. Mater.* **2006**, *16*, 1289-1298.

[11] Raz, S.; Hamilton, P. C.; Wilt, F. D.; Weiner, S.; Addadi, L.; *Adv. Funct. Mater.* **2003**, *13*, 480-486.

[12] Berman, A.; Addadi, L.; Weiner, S.; *Nature* **1988**, *331*, 546-548.

[13] Aizenberg, J.; Weaver, J. C.; Thanawala, M. S.; Sundar, V. C.;

Morse, D. E.; Fratzl, P.; *Science* **2005**, *309*, 275-278.

[14] Cai, A.; Xu, X.; Pan, H.; Tao, J.; Liu, R.; Tang, R.; Cho, K.; *J. Phys. Chem. C* **2008**, *112*, 11324-11330.

[15] Tang, H.; Yu, J.; Zhao, X.; *Mater. Res. Bull.* **2009**, *44*, 831-835.

[16] Reddy, M. M.; Hoch, A. R.; *J. Colloid. Interface Sci.* **2001**, *235*, 365-370.

[17] Kim, I. W.; Robertson, R.; Zand, Z.; *Cryst. Growth Des.* **2005**, *5*, 513-522.

[18] Falini, G.; Fermani, S.; Goisis, M.; Manganelli, G.; *J. Cryst. Growth Des.* **2009**, *9*, 153-169.

[19] Wang, G.; Li, L.; Lan, J.; Chen, L.; You, J.; *J. Mater. Chem.* **2008**, *18*, 2789-2797.

[20] Wada, N.; Kanamura, K.; Umegaku, T.; *J. Colloid. Interface Sci.* **2001**, *233*, 65-72.

[21] Kulak, A. N.; Iddon, P.; Li, Y.; Armes, S. P.; Cölfen, H.; Paris, O.; Wilson, R. M.; Meldrum, F. C.; *JACS* **2007**, *129*, 3729-3736.

[22] Schmidt, M. H.; Ellison, I.; Holliday, K.; Kubin, M.; Trujillo, F.; *J. Cryst. Growth* **2008**, *310*, 804-815.

[23] Westin, K. J.; Rasmuson, C.; *Desalination* **2003**, *159*, 107-118.

[24] Gabrielli, C.; Keddam, M.; Khalil, A.; Maurin, G.; Perrot, H.; Rosset, R.; Zidoune, M.; *J. Electrochem. Soc.* **2005**, *145*, 2386.

[25] Devos, O.; Gabrielli, C.; Tribollet, B.; *Electrochemical and Solid-State Letters* **2001**, *4*, C73.

[26] Devos, O.; Gabrielli, C.; Tlili, M.; Tribollet, B.; *J. Electrochem. Soc.* **2003**, *150*, C494-C501.

[27] Devos, O.; Gabrielli, C.; Tribollet, B.; *Electrochimica Acta* **2006**, *52*, 285-291.

[28] Teng, H. H.; Dove, P. M.; De Yoreo, J. J.; *Geochim. Cosmchim. Acta* **2000**, *64*, 2255-2266.

[29] Meldrum, F. C.; Hyde, S. T.; *J. Cryst. Growth* **2001**, *231*, 544-558.

[30] Pouget, E. M.; Bomans, P. H.; Goos, J. A.; Frederik, P. M.; de With, G.; Sommerdijk, N. A.; *Science* **2009**, *323*, 1455-1458.

[31] Rodriguez-Blanco, J. D.; Shaw, S.; Benning, L. G.; *Mineral. Mag.* **2008**, *72*, 283-286.

[32] Phillips, B. L.; Lee, Y. J.; Reeder, R. J.; *Environ. Sci. Technol.* **2005**, *39*, 4533-4539.

[33] Addadi, L.; Raz, S.; Weiner, S.; *Adv. Mater.* **2003**, *15*, 959-970.

Chapter 8 Effect of Commercially Relevant Inhibitors on the Deposition of Calcium Carbonate on Gold Surfaces

This chapter reports investigations of the efficiency and mode of action of a series of commercially available scale inhibitors on the deposition of calcium carbonate on foreign surfaces, using gold as a model. The investigations have been carried out using the flow system built in house and described fully in chapter 2 to allow the delivery of high supersaturation calcium carbonate solutions within a flow cell specifically designed to accommodate a quartz microcrystal balance probe.

This system allowed the fast screening of different additives and a quantitative ranking of their inhibitory properties on calcium carbonate deposition on a gold surface.

8.1 Introduction

As highlighted in chapter 6 and 7, calcium carbonate precipitation is of great interest in industrial, geological and biological processes, and a wide body of literature concerns the effect of additives on the nucleation and growth [1-8].

In the introduction of this thesis a brief overview was provided of some of the effects of additives on the nucleation and growth of crystals. This chapter focuses on a qualitative and quantitative evaluation of the inhibitory effects of commercial inhibitors on the calcium carbonate scaling process. The QCM-flow system discussed in the previous chapters has been employed and elucidated for fast screening of the potency of additives. This system allows the in–line mixing and delivery of a high supersaturation calcium carbonate solution to a surface in a specifically designed cell, and under these conditions the deposition process is sped up, allowing a quick evaluation of the inhibitory properties of the additives. Two main categories of commercial inhibitors have been evaluated: small molecular weight molecules; and polymers. The mechanisms by which these two categories of additives operate have been investigated to understand if a synergistic utilisation would optimise their inhibitory effect on calcium carbonate scaling.

8.1.1 Nucleation and Growth in the Presence of Inhibitors

8.1.1.1 Molecular Additives

Most molecular additives for scale have two different possible actions: i) complexation of calcium ions in solution, leading to a decrease in the activity product and thus a lower supersaturation value; ii) surface interactions specifically a binding process of the additive at the crystal surface that hinders the further uptake of material to the crystal, by blocking the active sites such as kinks and steps [9].

The structure of the molecules is, of course, a major factor that regulates the competition between solution complexation and surface adsorption. Solution complexation is favoured through a flexible backbone that allows a molecule to form around the ion in such a way as to optimise the distances between the binding sites and the ion itself. A well-known example is ethylenediaminetetracetic acid (EDTA) [10] that forms a highly stable complex in solution surrounding a cation, such as Ca^{2+} with its carboxylic groups as shown in Figure 8-1.

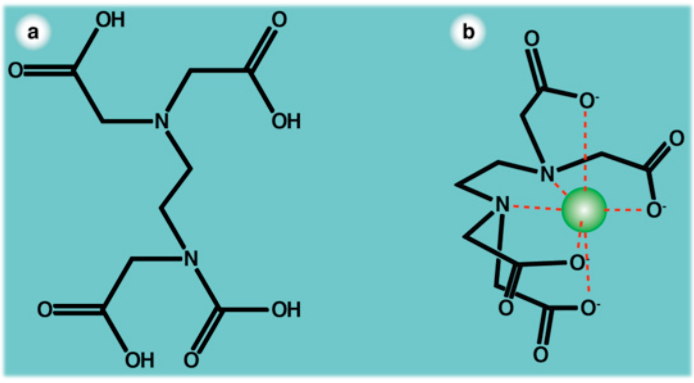

Figure 8-1. (a) EDTA structure; (b) EDTA-cation complex.

A flexible chain, while helping to form a more stable complex in solution, can be detrimental in the formation of a stable complex on the surface, it be can easily removed from the surface via one by one bond detachment. In contrast, a rigid molecule needs to break all the bonds simultaneously in order to detach from the surface. However, in this case the distance between the active functional groups requires significant regulation as a consequence of a rigid structure. Geffroy *et al.* [11] investigated this aspect, evaluating the adsorption of a set of dicarboxylates on calcite, reporting different surface adsorption for different chain lengths (Figure-8-2).

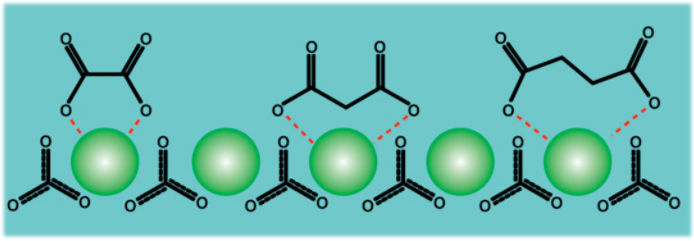

Figure-8-2. Adsorption of n-dicarboxylates in order of stability [11].

Moreover, the distance between functional groups can promote the preferential adsorption at particular crystal faces, depending on the lattice structure [12] or the inhibition of a specific polymorphs. For example, the work by Schmidt *et al.* [13] showed the inhibition of aragonite nucleation without affecting calcite growth using citrate and isocitrate.

8.1.1.2 Polymeric Additives

Polymeric additives with negatively charged functional groups, such as carboxylates or sulphonates, can sequester cations in solution forming complexes and decreasing the supersaturation in solution, hence inhibiting the precipitation of calcium carbonate [14]. However, the most interesting outcome is the effect on the formation of the ACC intermediate [15], since the polymer provides active

sites for the nucleation and formation of ACC nanoparticles in solution and can also control the aggregation of the nanoparticles as shown in the recent work of Park *et al.* [16].

In systems where a high supersaturation is reached in the presence of polymers, such as polycarboxylates, polyacrylic acid and poly-(aspartic acid), the formation of a liquid-like precursor appear to be favoured [3, 17-19]. Slowly adding carbonate to a supersaturated solution of $CaCl_2$ in the presence of a polymeric agent, leads to a critical concentration in which the solution undergoes a liquid-liquid separation, forming small droplets. The droplets behave as a liquid phase and a film can easily form at a wettable surface. Gower *et al.* have exploited this peculiar behaviour to form an array of different crystal polymorphs over a patterned substrate [19]. Spinodal separation is a rather well established process [20, 21] that takes place quickly when a supersaturated solution is formed, i.e. immediately following the rapid mixing of a calcium and carbonate solution. The liquid like phase is short lived and quickly decomposes to nanoparticles (ACC) [22], which are stabilised by polymeric additives as shown by Rieger *et al.* [2, 17].

8.1.2 Current Research

The mechanism of the initial formation of calcium carbonate at high supersaturation has been extensively investigated and the latest works of Reiger *et al.* [20] and Gebauer *et al.* [23] have provided notable insight on this process. Furthermore, chapter 6 considered in detail the process occurring during the heterogeneous deposition of $CaCO_3$ on glass and gold surfaces. The effect of additives/inhibitors on calcium carbonate crystallisation and growth has been

widely studied [7, 9, 24-29] and chapter 7 looked in detail at the case of CIT. However, little attention has been given to the effectiveness of surface inhibition and the influence of scale inhibitors on the deposited structure.

The dynamic calcium carbonate crystallisation process in the presence and absence of inhibitors has been studied by Dobson *et al.* [5, 30] and Orme *et al.* [31] using AFM. However, these studies require low supersaturation conditions in order to slow down growth. Notable studies at higher supersaturation are those performed by Garcia *et al.* [6] and Granit *et al.* [14] using electrochemical techniques to accelerate surface deposition in the presence of inhibitors. Such studies are important because there are often discrepancies between the crystallisation characteristics in the bulk and on a surface, particularly in the presence of inhibitors. Not only that, but in industrial water systems for example, the morphology of crystals formed upon a surface can effect the flow and cleaning procedures [14], and it is this essential to be at able to study the efficiency of inhibitors in the nucleation and growth of crystal on foreign substrates.

This chapter builds on the work in the previous two chapters and shows that the methodologies developed can be applied to access the action of a range of commercial scale inhibitors.

8.2 Experimental

8.2.1 Additives

The additives were commercial inhibitors used in consumer anti-scaling products supplied by Reckitt–Benckiser. The additives, as mentioned above comprised two main categories molecular and polymeric agents. The exact formulation of the additives were unknown, but the main component molecular structures are shown in Figure 8-3,

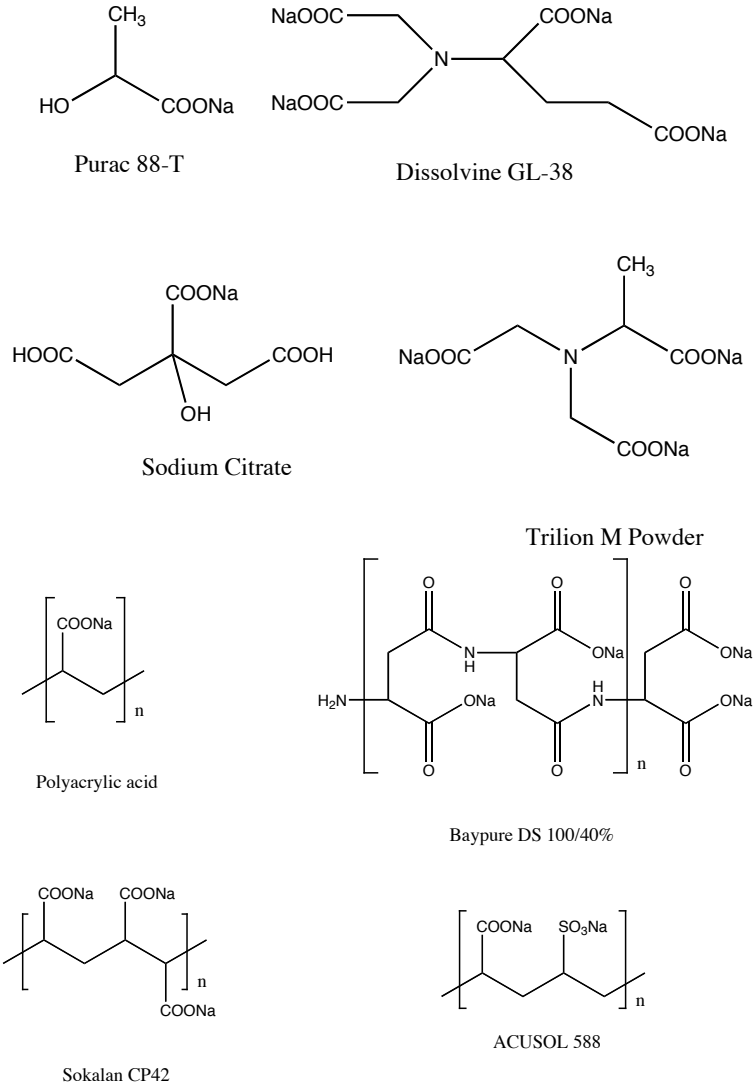

Figure 8-3. Main component molecular structures of additives investigated.

The solutions were prepared following the same procedure described in chapter 6 – 7 (10 mM $NaHCO_3$ and 20 mM $CaCl_2\,2H_2O$, both solutions corrected to pH 10.50 with 1 M NaOH). Unless otherwise stated, the additives were added to the calcium solution prior to adjusting the pH, which favoured the complexation of the calcium ions. In order to compare the inhibitory effects of the different additives, the concentrations were calculated in relation of the number of calcium ions that each unit of a polymer or molecule could complex. The concentration was equal to 5 mM before mixing, however for Acusol 588 a concentration of 2.5 mM was used because at higher concentrations no $CaCO_3$ deposition was seen. Further experiments were focused on comparing the synergistic effect of the acrylic polymer with CIT. Solutions with equal concentrations of both components were prepared with an overall concentration of 5 mM to compare the effect of the mixture with respect to solutions of each additive alone. Finally, some experiments with CIT explored whether there was any difference by adding the additives to the carbonate solution rather than the calcium solution.

Table 8-1. Chemical used, their purity/grade and suppliers.

Chemical	*Purity/Grade*	*Supplier*
$NaHCO_3$	99.5%	BDH
$CaCl_2\,2H_2O$	99.0%	Sigma
NaOH	Laboratory Reagent Grade	Fischer Scientific
Acetone	Analytical Grade	Fischer Scientific
Chloroform	Laboratory Reagent Grade	Fischer Scientific
Na Di-hydrogen Citrate	99%	Aldrich
Baypure DS 100/40%	38%	Reckitt Benckiser
Sokalan CP 42	40%	Reckitt Benckiser
Acusol 588G	-	Reckitt Benckiser

Chemical	*Purity/Grade*	*Supplier*
Trilon M Powder	86%	Reckitt Benckiser
Purac 88-T	88%	Reckitt Benckiser
Dissolvine GL-38	38%	Reckitt Benckiser
Polyacrylic acid	-	Reckitt Benckiser

Table 8-2. Additives used and concentrations, (*) added to carbonate solution.

Additive	*Mw unit / g mol^{-1}*	*Number of active sites*	*Mass added per 100 ml / g*	*Active groups / mM*
Acusol 588	224	1	0.0567	2.5
Sokalan CP2	254	2	0.1604	5.1
Trilon M Powder	90	1	0.0450	4.3
Purac 88-T	90	1	0.0513	5.0
Dissolvine GL-38	351	2	0.2170	4.7
Baypure DS 100/40%	137	1	0.1772	4.9
Polyacrylic acid	94	1	0.0431	4.6
Na di-hydrogen citrate	214	1	0.1077	5.0
Polyacrylic acid	94	1	0.0237	2.5
Na di-hydrogen citrate	214	1	0.0592	2.6
Polyacrylic acid*	94	1	0.0241	2.6
Na di-hydrogen citrate*	214	1	0.0591	2.6

8.3 Results and Discussion

The QCM-flow system was employed following the same protocol described in chapters 2, 6 and 7 with a total deposition time of 900 s. The QCM crystals were extracted after deposition and FE-SEM imaging was performed after gold coating to analyse the morphology of the precipitate on the surface.

Table 8-3 reports the mass deposited after 900 s under flow (flow rate of 2 ml min^{-1}) measured with the QCM-flow system for each of the additives examined.

Table 8-3. Total mass of $CaCO_3$ deposited after 900 s for each additives in descending order of efficacy. (#) Used half concentration with respect other addictives.

Additive solutions	*Molecular structure*	*Mass deposited / μg*
Acusol 588#	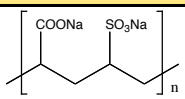 ACUSOL 588	0.03 ±0.01
Sokalan CP2	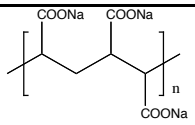	0.12 ±0.01
Baypure DS 100/40%	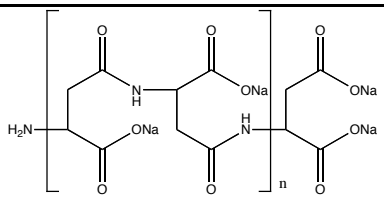	0.51 ±0.01
Dissolvine GL-38	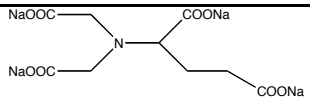	1.23 ±0.01
Na di-hydrogen citrate	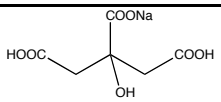	6.24 ±0.01
Polyacrylic acid	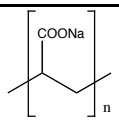	6.44 ±0.01
Purac 88-T	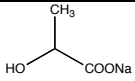	13.76 ±0.01
Trilon M Powder	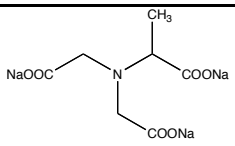	31.25 ±0.01
No additive		56.32 ±0.01

8.3.1 Polymeric Additives

The polymers investigated all contained negatively charged functional groups, which bind calcium ions in solution. Since the additives were added to the calcium ion containing solutions, the polymers will lead to form complexes with the calcium ions in solution and during the mixing process the CO_3^{2-} ions interacted with the bound calcium. Based on the work of Rieger *et al.* [17] that demonstrated the formation of ACC around the polymer this would be expected to form stable ACC particles in solution. Ex–situ FE-SEM images of the QCM crystals, Figure 8-4, showed the presence of material for all the additives employed, Baypure (a), Sokalan (b) and Acusol (c), while for Baypure and Sokalan the deposited material is in form of large particles. Acusol showed the formation of flocks on the surface. At higher magnification, it was possible to identify that the flocks were formed by small particles of few hundred nm dimension. The interaction of Sokalan with the nucleating calcium carbonate gave birth to polycrystals which were formed upon aggregation of small crystals with a pseudo rhomboid shape. This indicates that there is a strong interaction of the polymer with the inner crystal structure and it provides a bridge between crystals for the formation of agglomerates [7].

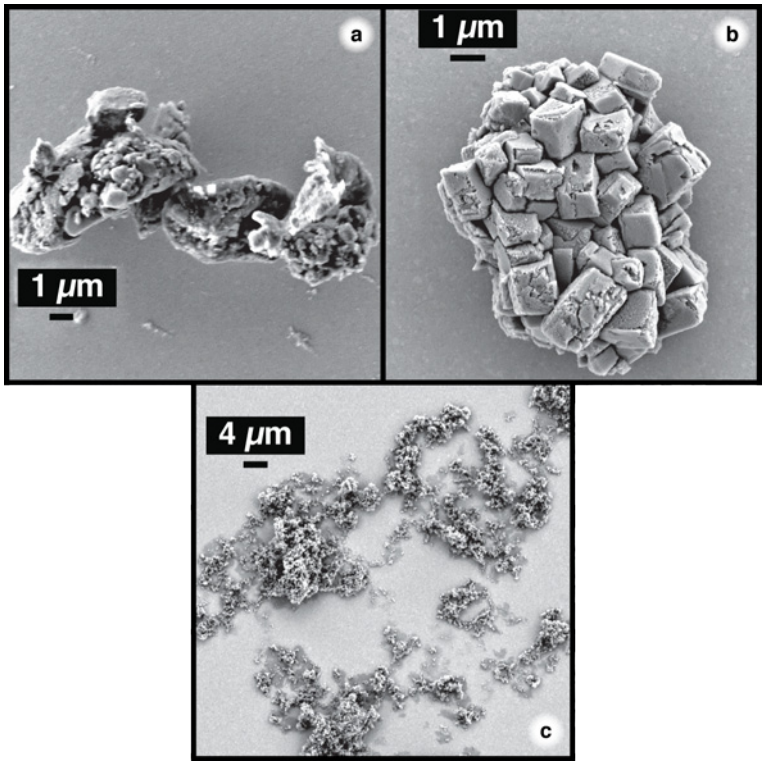

Figure 8-4. FE-SEM images of QCM crystals surfaces after deposition of calcium carbonate in the presence of: (a) Baypure, (b) Sokalan and (c) Acusol.

The deposition of $CaCO_3$ on the surface of the QCM probe is clearly retarded for all the additives. The chelating effect of the polymers with Ca^{2+} and the nucleation and growth of polymer-stabilised particles in solution [2] decreases the supersaturation at the QCM probe surface and, furthermore, the particles formed in solution are likely transported away, resulting in low scaling on the surface.

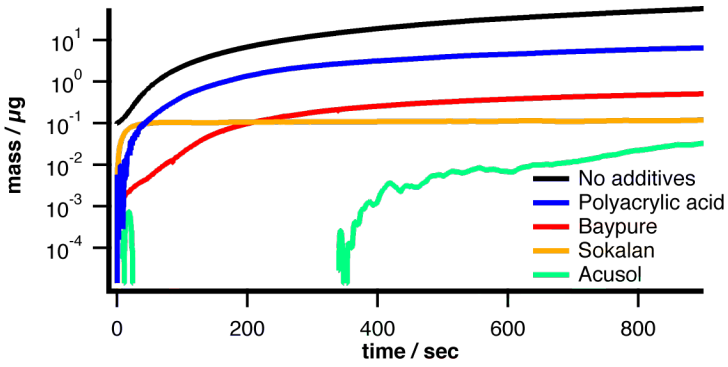

Figure 8-5. Gravimetric curves showing the deposition of calcium carbonate as function of time in the presence of polymeric additives. Note the scale in y axis.

Polyacrylic acid was found to be the least effective inhibitor of calcium carbonate deposition compared to the other polymers investigated (Figure 8-5). The structure of polyacrylic acid and the Acusol molecule only differ by one functional group; in Acusol one of the carboxylate groups is replaced by a sulfonate. It appears that the sulfonate group greatly increases the chelating and nucleating ability of this polymer relative to the polyacrylic acid. Similarly, Sokalan also has a closely related structure to polyacrylic acid, only differing in its tacticity. This difference may aid its ability to sequester calcium ions and enhance the nucleation of small polymer-functionalised particles.

8.3.2 Molecular Additives

The large amounts of nucleation observed on the surface of the QCM probes (Figure 8-7, Figure 8-9 and Figure 8-12) along with the high deposition recorded by QCM (Figure 8-6 and Table 8-3), indicates that the molecular additives examined are less effective than polymeric additives in sequestrating ions in solution and reducing the overall supersaturation. However, it can also be seen that in each case there is a morphological change from the rhombohedral

calcite crystals observed in the control experiment without additives (see chapter 6), indicating that this is induced by additive surface complexation (Figure 8-7, Figure 8-9 and Figure 8-12).

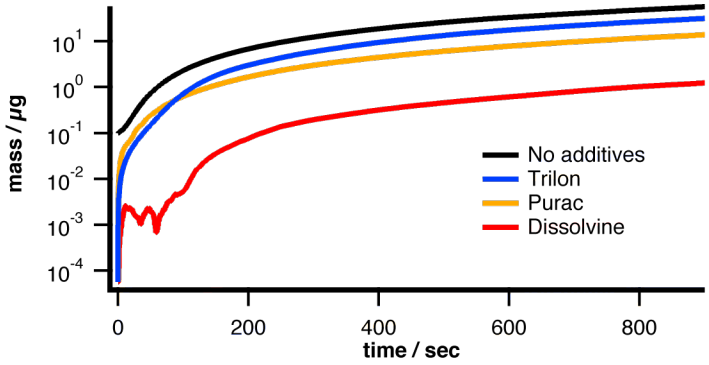

Figure 8-6. Gravimetric curves showing the deposition of calcium carbonate as function of time in the presence of molecular additives. Note the scale in y axis.

8.3.2.1 *Dissolvine GL-38*

Dissolvine was found to be the most effective molecular additive tested; with inhibition properties comparable to the polymeric additives, since the amount of calcium carbonate deposited was similar to that measured for some of the polymeric additives. The FE-SEM images (Figure 8-7) show relatively high heterogeneous nucleation, but the particles are small so that the overall mass deposition is low. In fact, from the FE-SEM images, it can be seen that Dissolvine induces a striking morphological change on calcium carbonate crystal growth.

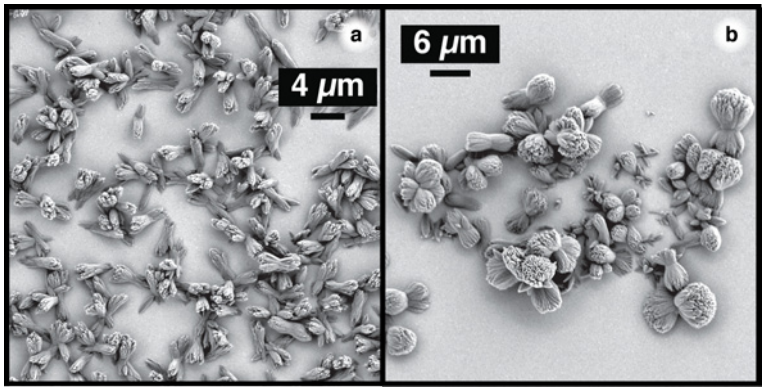

Figure 8-7. FE-SEM images of calcium carbonate grown in the presence of Dissolvine GL-38.

Interestingly, Yu *et al.* [32] have recently observed a similar morphological structure on calcium carbonate formed in the presence of magnesium ions in an ethanol solution. The proposed mechanism (Figure 8-8) for the deposition of these 'peanut'-like particles involves the stabilisation and subsequent aggregation of ACC rods in solution, followed by precipitation and further surface nucleation and growth of new sub-crystals on the rods sides.

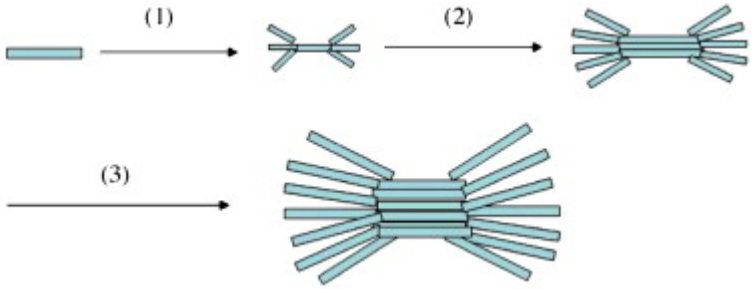

Figure 8-8. Schematic illustration of the formation of novel peanut-like $CaCO_3$ aggregates: (1) the growth of fractal structure through the nucleation and growth on the side-surface of the rods; (2 and 3) the evolution of peanut-like aggregates (based on reference [32]).

In this system, the magnesium ions and ethanol solvent were key components in the formation and stabilisation of the ACC rods. In fact, a control experiment was performed replacing the ethanol solvent by water and the morphology of the crystals obtained was completely different to that obtained in the presence of ethanol. Additionally, these crystals were precipitated from

solution. From Figure 8-7 it can be seen that the crystals obtained in the presence of the Dissolvine molecule were nucleated heterogeneously on the gold surface, therefore a similar aggregation type mechanism is unlikely to be involved in this case. A more likely possibility is a continuous growth in which the presence of bound Dissolvine molecules to the surface of crystals nucleated upon the gold surface leads to a change in growth patterns. Unfortunately, since the sample was grown upon gold, it was not possible to perform Raman spectroscopy to identify the polymorph formed. It may be that the Dissolvine molecule binds more favourably to one polymorph over another [1]. The deposition on a different substrate that allows Raman characterisation could be relevant to understand this aspect and to have an insight of the influence of the substrate on the growth.

The ability of Dissolvine to form strong solution complexes is evident from its structure. The Dissolvine molecule has four flexible side chains terminated by carboxylate groups. This enables it to wrap around the Ca^{2+} ions in a similar way to EDTA (Figure 8-1).

8.3.2.2 Trilon M Powder

Trilon was found to have the poorest inhibiting ability, with a mass deposition of 31.25 ±0.01 μg. From the FE-SEM images it can be seen that the Trilon molecule does bind to the co-ordinatively unsatisfied Ca^{2+} ions on the surface of nucleated $CaCO_3$ particles (Figure 8-10).

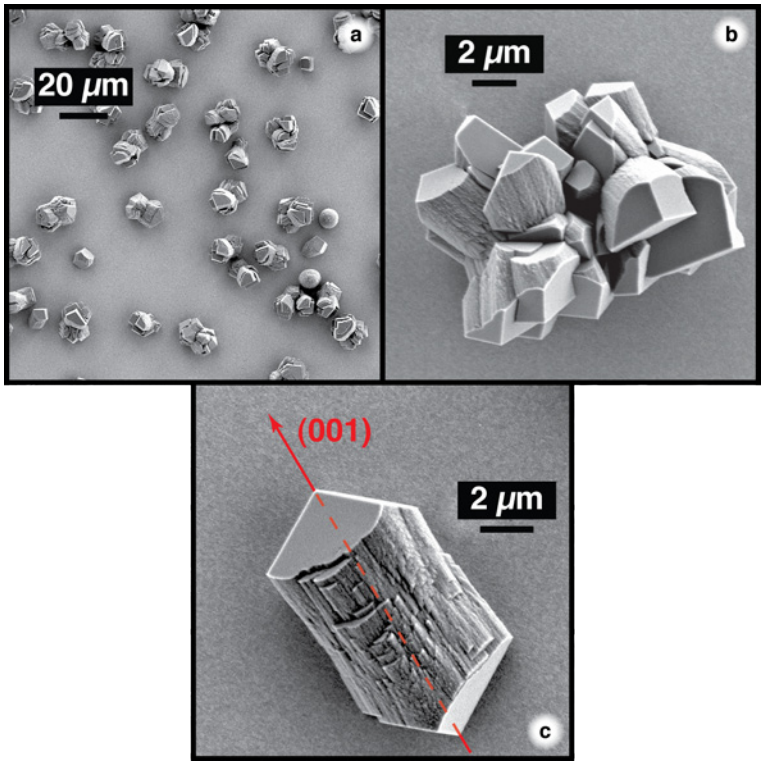

Figure 8-9. FE-SEM images of calcium carbonate grown in the presence of Trilon M Powder, (c) highlighted the (001) direction.

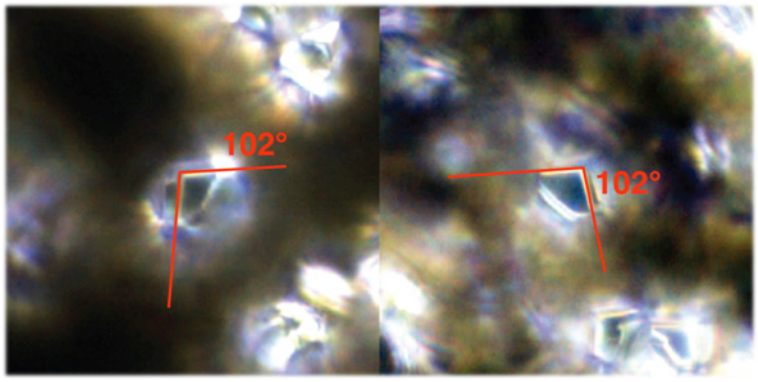

Figure 8-10. Optical images (at high magnification with small optical focus, only the planes perpendicular to the lens were on focus) of calcium carbonate grown in the presence of Trilon M Powder. Highlighted the angle of 102° of the (104) plane, the 78° angle was absent.

The crystals exhibited an elongated shape with rounded edges, thus the adsorption of the Trilon molecule onto the surface prevents the development of all of the rhombohedral facets. In the dark field optical images only the corners

with angles 102° are visible. Rhombohedral calcite presents only two corners in which all the vertexes are of 102° (see Figure 8-11), and thus it is proposed that the inhibitory of the Trilon mainly influences growth in the directions perpendicular to the diagonal that connects the two vertexes which corresponds to the (001) direction without interfering with the two dimensional nucleation growth (see chapter 1) on the {104} planes.

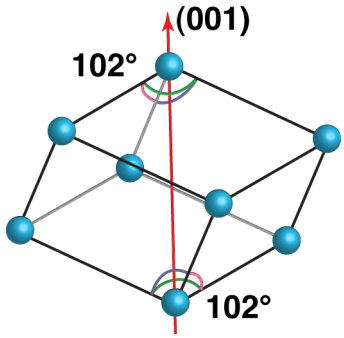

Figure 8-11. Representation of a rhombohedral calcite crystal, with the (001) direction ighlighted.

8.3.2.3 Purac 88-T

Purac was also found to be a poor inhibitor, with a deposition of 13.76 ±0.01 µg. However, many of the crystals observed were spherical in shape (Figure 8-12). This could mean that the Purac molecule is successful at binding to many calcite planes; completely inhibiting the formation of rhombohedral facets. The polymorph formed could be calcite, but it maybe a different polymorph. On the other hand, rhombohedral crystals are seen at the edge of the probe suggesting the formation of some calcite.

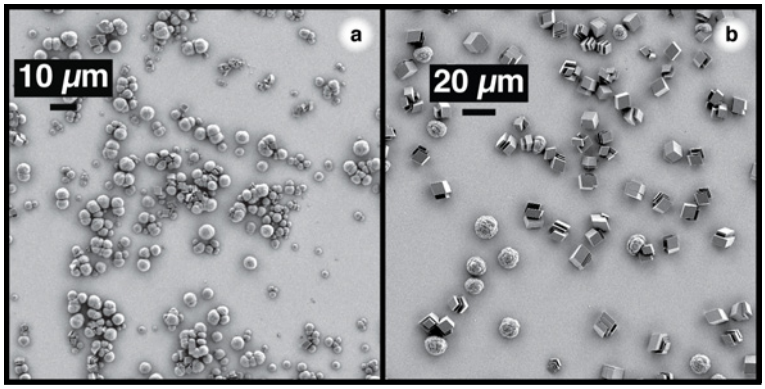

Figure 8-12. FE-SEM images of calcium carbonate grown in the presence of Purac (a) underneath the nozzle (b) at the edge of the probe surface.

Purac contains a carboxylate group with an α-hydroxide group, which has been shown to increase the strength of surface complexes by simultaneously binding to a calcium ion and a carbonate ion on the surface [11] (see Figure 8-13).

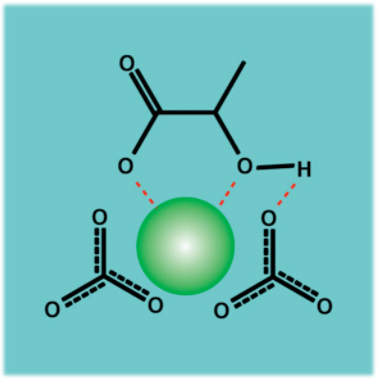

Figure 8-13. Schematic representation of the Purac molecule interacting with the surface of a calcium carbonate crystal.

8.3.3 Synergistic Effects

To examine whether the inhibition of calcium carbonate precipitation and growth could be improved by having both molecular and polymeric additives present, experiments were run in the presence of both polyacrylic acid and sodium citrate. These two additives were chosen because they both had fairly

average inhibiting ability in isolation (see above). First, an experiment was run in which these two additives were incorporated into the carbonate solution prior to mixing. The result was compared with that obtained when the two additives were incorporated into the calcium solution prior to mixing, in order to assess the effect of initial solution complexation.

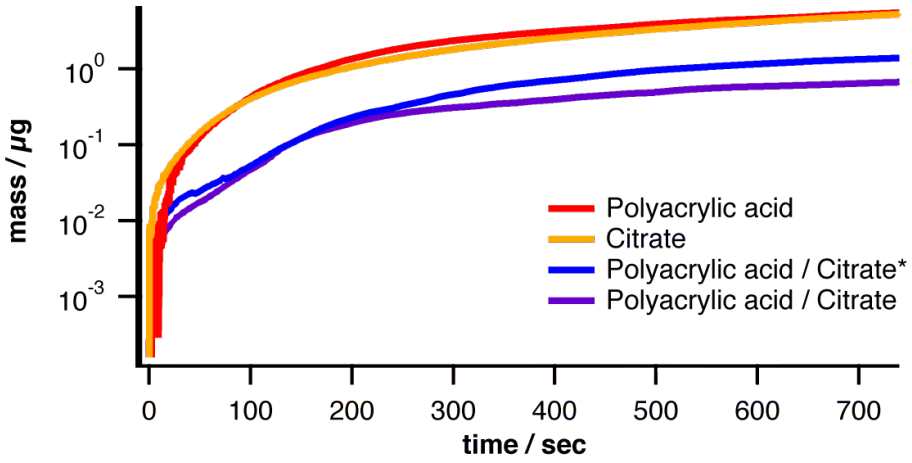

Figure 8-14. Gravimetric curves for Polyacrylic acid and sodium citrate, (*) the additive was added to the carbonate solution prior to mixing. Note the scale in y axis.

From Table 8-3, and the gravimetric curve (Figure 8-14), it can be seen that the combined additives show greatly enhanced performance.

It was also found that the additives are more effective when added to the solution containing calcium ions prior to mixing, presumably because this gives more time for the formation of Ca^{2+} additive solution complexes.

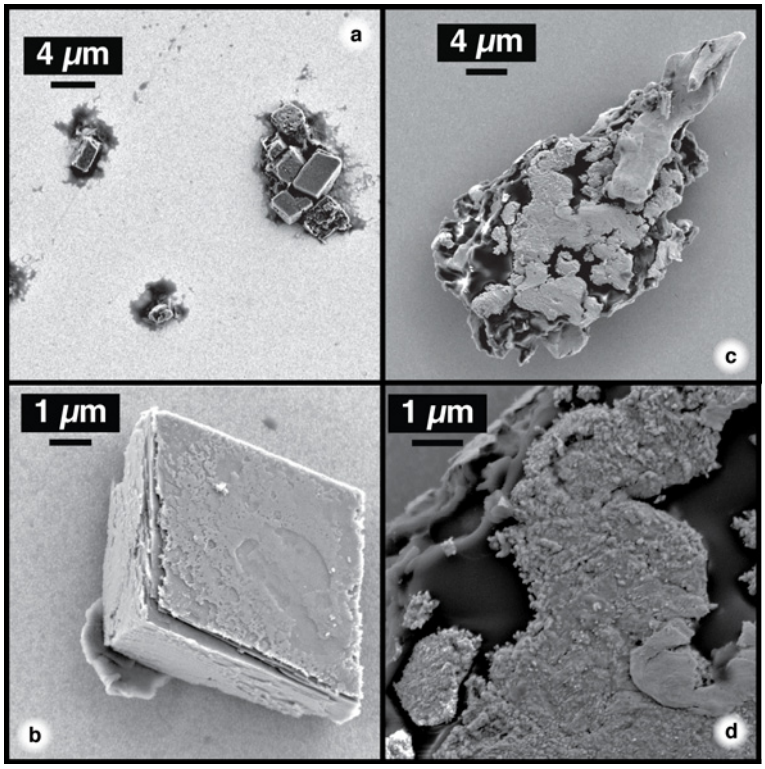

Figure 8-15. FE-SEM images of calcium carbonate grown in the presence of pure sodium citrate and polyacrylic acid. The additives were incorporated into the (a, b) carbonate solution and (c, d) calcium solution prior to mixing.

From the FE-SEM images (Figure 8-15) it can be seen that when the additives were incorporated into the calcium in solution prior to mixing, the small amount of material deposited on the gold surface is polymer-stabilised calcium carbonate. The rough surface of this particle is likely to be due to the combined influence of attachment of polymer molecules and the highly stabilising effect of CIT on ACC (see Chapter 7). When the additives were incorporated into the carbonate solution, prior to mixing, the nucleation and growth supported by the polymer was less effective. In fact, strikingly, the material deposited on the surface had a rhombohedral shape typical of calcite crystal.

8.4 Conclusion

The system developed in the earlier chapters (6 and 7) provides a very effective method to investigate quantitatively the inhibitory effect of a set of additives. This set up allows for the quick screening of a numbers of additives and the ability to work with well-defined high supersaturation conditions is very important for mimicking the conditions normally encountered in domestic or industrial environments.

The overall ranking of the inhibitors obtained showed that the polymeric additives were more effective as anti-scaling agents compared to the molecular additives, however the synergism obtained by combining both types of inhibitors resulted in an increase of the scaling inhibition efficacy. This is an interesting observation that needs to be investigated further to understand which mechanism leads to this synergistic effect between different types of inhibitors.

Further work could be to investigate the structure of the crystals formed in the presence of molecular and macromolecular additives and to obtain a better insight on the molecular interactions between the additives and the calcium carbonate solid phase. In this case, molecular modelling could be particularly fruitful. This information would be useful to aid understanding the inhibition mechanisms of the additives investigated.

8.5 Bibliography

[1] Westin, K. J.; Rasmuson, A. C.; *J. Colloid. Interface Sci.* **2005**, *282*, 359-369.

[2] Rieger, J.; Frechen, T.; Cox, G.; Heckmann, W.; Schmidt, C.; Thieme, J.; *Faraday Discuss.* **2007**, *136*, 265-277.

[3] Lam, R. S. K.; Charnock, J. M.; Lennie, A.; Meldrum, F. C.; *CrystEngComm* **2007**, *9*, 1226-1236.

[4] Quigley, D.; Rodger, P. M.; *J. Chem. Phys.* **2008**, *128*, 221101.

[5] Dobson, P. S.; Bindley, L. A.; Macpherson, J. V.; Unwin, P. R.; *ChemPhysChem* **2006**, *7*, 1019-1021.

[6] Garcia, C.; Courbin, G.; Ropital, F.; Fiaud, C.; *Electrochim. Acta* **2001**, *46*, 973-985.

[7] Kulak, A. N.; Iddon, P.; Li, Y.; Armes, S. P.; Cölfen, H.; Paris, O.; Wilson, R. M.; Meldrum, F. C.; *JACS* **2007**, *129*, 3729-3736.

[8] Gebauer, D.; Cölfen, H.; Verch, A.; Antonietti, M.; *Adv. Mater.* **2009**, *21*, .

[9] Westin, K. J.; Rasmuson, C.; *Desalination* **2003**, *159*, 107-118.

[10] Altay, E.; Shahwan, T.; Tanoglu, M.; *Powder Technol.* **2007**, *178*, 194-202.

[11] Geffroy, C.; Foissy, A.; Persello, J.; Cabane, B.; *J. Colloid. Interface Sci.* **1999**, *211*, 45-53.

[12] Falini, G.; Fermani, S.; Goisis, M.; Manganelli, G.; *J. Cryst. Growth Des.* **2009**, *9*, 153-169.

[13] Schmidt, M. H.; Ellison, I.; Holliday, K.; Kubin, M.; Trujillo, F.; *J. Cryst. Growth* **2008**, *310*, 804-815.

[14] Granit, N. F.; Korin, E.; Bettelheim, A.; *Chem. Eng. Technol.* **2003**, *26*, 341-346.

[15] Guillemet, B.; Faatz, M.; Gröhn, F.; Wegner, G.; Gnanou, Y.; *Langmuir* **2006**, *22*, 1875-1879.

[16] Park, J.; Oh, S.; *Mater. Res. Bull.* **2009**, *44*, 110-118.

[17] Rieger, J.; Thieme, J.; Schmidt, C.; *Langmuir* **2000**, *16*, 8300-8305.

[18] Levi-Kalisman, Y.; Raz, S.; Weiner, S.; Addadi, L.; Sagi, I.; *Adv. Funct. Mater.* **2002**, *12*, 43-48.

[19] Kim, Y. Y.; Douglas, E. P.; Gower, L. B.; *Langmuir* **2007**, *23*, 4862-4870.

[20] Liu, J.; Rieger, J.; Huber, K.; *Langmuir* **2008**, *24*, 8262-8271.

[21] Faatz, M.; Grohn, F.; Wegner, W.; *Adv. Mater.* **2004**, *16*, 996-1000.

[22] Wolf, S. E.; Leiterer, J.; Kappl, M.; Emmerling, F.; Tremel, W.; *JACS* **2008**, *130*, 12342-12347.

[23] Gebauer, D.; Völkel, A.; Cölfen, H.; *Science* **2008**, *322*, 1819-1822.

[24] Dickinson, S. R.; McGrath, K. M.; *Cryst. Growth Des.* **2004**, *4*, 1411-1418.

[25] Donners, J. J. J. M.; Meijer, E. W.; Nolte, R. J. M.; Roman, C.; Schenning, A. P. H. J.; Sommerdijk, N. A. J. M.; Heywood, B. R.; *Chem. Commun.* **2000**, 1937-1938.

[26] Garcia-Carmona, J.; Gomez-Morales, J.; Fraile-Sainz, J.; Rodriguez-Clemente, R.; *Powder Technol.* **2003**, *130*, 307-315.

[27] Kim, I. W.; Robertson, R.; Zand, Z.; *Cryst. Growth Des.* **2005**, *5*, 513-522.

[28] Martinod, A.; Neville, A.; Euvrad, M.; Sorbie, K.; *Chem. Eng. Sci.* **2009**, *64*, 2413-2421.

[29] Tang, Y.; Yang, W.; Yin, X.; Liu, Y.; Yin, P.; Wang, J.; *Desalination* **2008**, *228*, 55-60.

[30] Dobson, P. S.; Bindley, L. A.; Macpherson, J. V.; Unwin, P. R.; *Langmuir* **2005**, *21*, 1255-1260.

[31] Orme, C. A.; Noy, A.; Wierzbicki, A.; McBride, M. T.; Grantham, M.; Teng, H. H.; Dove, P. M.; DeYoreo, J. J.; *Nature* **2001**, *411*, 775-779.

[32] Tang, H.; Yu, J.; Zhao, X.; *Mater. Res. Bull.* **2009**, *44*, 831-835.

Chapter 9 CONCLUSIONS

As highlighted in the introduction (chapter 1), this thesis has explored methods for promoting, preventing and understanding the functionalisation of interfaces with a wide range of materials and progress has been made in each area.

For molecular-functionalisation, the complex [(biph-tpy)Ru(tpy-thioctic)]$(PF_6)_3$ proved suitable for the formation of self assembled monolayers, on a platinum substrate. The double sulphur group formed a strong bond with the substrate, allowing the formation of a packed SAM. The technique employed for the deposition, with a sweeping potential function, resulted in a great improvement in the SAM deposition, making the deposition process much faster. This formation of SAMs with a recognition site on a conductive is an important step for the development of non-covalent molecular wires.

Particular success has been achieved in the fabrication of novel nano-composite material. Ultrathin Nafion films, deposited by the Langmuir-Schaefer technique, proved to be suitable as templates for the chemical production and incorporation of palladium nanoparticles. The thickness of the films formed could be controlled with high precision and the nanoparticles formed had a low

size dispersion. The nano-material prepared following this procedure resulted in catalytic activity towards hydrogen oxidation and generation and this nano-material could be suitable for utilisation in sensor devices and fuel cells.

The protocol used for the deposition of cyclodextrin capped platinum nanoparticles on different substrates showed high degree control on the amount of catalyst deposited. This is useful for applications in which the amount of catalyst deposited is of paramount importance. Moreover, this technique allowed the deposition of highly monodispersed nanoparticles. The final functionalised substrate showed catalytic properties on oxygen and hydrogen redox reactions.

Turning to the understanding more complex deposition processes, a delivery system developed for studying crystal formation provided an optimum tool to investigate calcium carbonate deposition processes at high-supersaturation conditions. The presence of ACC in solution and on the substrate was shown to be a very important factor. Moreover, our experimental investigations and mathematical modelling showed that the deposition is likely to be controlled by ion pairs in solution.

An important outcome of the studies herein is that inhibitors such as CIT show complex behaviour on the scaling properties of calcium carbonate solutions. The stabilisation of ACC in solution and at the substrate shows a non-monotonic behaviour with respect the concentration of CIT on the amount of calcium carbonate deposited. This result is rather important, because so called inhibitors could actually increase the amount of calcium carbonate deposited within a particular range of additive concentration.

The experimental set up developed for studying crystal formation proved to be a powerful tool as a screening system to investigate in a quick and reliable fashion a series of scaling inhibitors. Polymeric additives showed a completely different mechanism of inhibition compared to the molecular additives. Polymeric inhibitors act as a nucleation site and the calcium carbonate grows embedded in the polymers, while the molecular additives participate to crystal growth, having an important effect on the final crystal structure.

A combined utilisation of both the additives types showed the best results on the scaling inhibition.

In summary, the work herein resulted in the field of surface functionalisation and several aspects have opened up prospects for significant further work.

Appendix A

Attached to the thesis there are a series of movies related to experiments describe in chapter 6 and 7.

Movie 1: 10 mM calcium ions, 5 mM carbonate ions, pH 10.5, the microscope was focused slightly beyond the glass surface and off from the centre of the nozzle.

Movie 2: Feed process, 22 min duration.

Movie 3: Feed process, 12 min duration.

Movie 4: 10 mM calcium ions, 5 mM carbonate ions, pH 10.5, 1000 s.

Movie 5: 10 mM calcium ions, 5 mM carbonate ions, 1.75 mM citrate ions, pH 10.5.